H. Niewodniczański Institute of Nuclear Physics
Polish Academy of Science

Analysis of Diffractive Processes in Electron-Proton and Proton-Proton Collisions

Agnieszka Łuszczak

Thesis presented for the degree of Doctor of Philosophy
written under the supervision of
Prof. dr hab. Krzysztof Golec-Biernat

Kraków
2009

Abstract

In this thesis, the analysis of diffractive processes in electron-proton and hadronic collision is presented. Diffractive parton distributions are determined from fits with a twist-4 contribution to the diffractive deep inelastic scattering data from HERA. A new prediction for the longitudinal diffractive structure function F_L^D is presented which differs significantly from that obtained in the pure twist-2 analysis.The newest diffractive data from HERA are analyzed using the dipole model. Good agreement between the predictions and the data on the diffractive structure functions is found. For the diffractive open charm production, a significant sensitivity to the form of the diffractive gluon distribution is found. Diffractive production at hadronic colliders is also analyzed. The determined diffractive parton distributions are used to assess the gap survival probability and to make predictions for the diffractive production of electroweak bosons at the LHC. It is noted that the W boson asymmetry in rapidity is a good observable to test of the concept of flavor symmetric parton distribution functions in the pomeron.

Streszczenie

Niniejsza praca prezentuje analizę procesów dyfrakcyjnych w zderzeniach elektron-proton i proton-proton. Wyznaczone zostały dyfrakcyjne rozkłady partonowe z fitu do danych z HERY, z uwzględnieniem wkładu typu wyższy twist. Wykonano nowe przewidywanie dla podłużnej dyfrakcyjnej funkcji struktury F_L^D. Pokazano, że po uwzględnieniu wyższego twistu, funkcja ta znacząco różni się od tej tylko z wiodącym twistem. Wykonano także porównania przewidywań dla tej funkcji z ostatnio zmierzonymi danymi. Zanalizowano najnowsze dane dyfrakcyjne z HERY przy pomocy modeli dipolowych. Znaleziono dobrą zgodność z danymi przewidywań dla dyfrakcyjnej funkcji struktury. Policzono dyfrakcyjną produkcję charmu podkreślając istotną rolę rozkładów gluonowych w pomeronie. Wyznaczone dyfrakcyjne rozkłady partonowe zostały użyte do oszacowania faktora przeżycia przerwy w rapidity i wykonania przewidywań dla dyfrakcyjnej produkcji elektrosłabych bozonów na LHC. Pokazano, że asymetria w rapidity produkcji naładowanych bozonów W jest dobrą obserwablą do zbadania rozkładów partonowych w pomeronie.

Contents

Preface

Diffractive processes constitute a substantial fraction of the total cross section for electron-hadron collisions. They are also observed at hadronic colliders, although at a lower rate. A typical signature of the diffractive processes is a rapidity gap between the final state particles, which form the diffractive system, and a loosely scattered hadron(s). We can classify these processes into two distinct classes: *soft diffractive processes* and *hard diffractive processes*. A classical example of soft reaction is diffractive dissociation, being a special case of inclusive production in a quasi two-body process, wherein all quantum numbers of two final state groups of particles (i.e. charge, isospin, strangeness etc.) are the same as of the initial hadrons. The study of hard diffractive processes is a relatively new research field, initiated by the observation of diffractive events in deep inelastic scattering (DIS) at HERA. The characteristic feature of hard diffraction is the presence of large scale (like the photon virtuality Q^2 in DIS) which allows to use perturbative QCD in the description of these processes. The example of such events in hadronic collisions is the high E_T dijet production with large rapidity gap, which was first observed by the UA8 Collaboration [1] and later by CDF and D0 Collaborations at the Tevatron (1995) [2, 3].

In the last years, it was possible to discover and investigate diffractive processes which have soft and hard properties at the same time. A typical process of this type is *diffractive deep inelastic scattering (DDIS)*. DDIS is simply a deep inelastic scattering reaction with a particular final state configuration, characterized by a large *rapidity gap* between the proton remnant and the products of the hadronization of the photon. It implies that there is no exchange of quantum numbers (except those of the vacuum) between the virtual photon and the proton. These processes have been first observed at HERA in the year 1993 by the ZEUS and the H1 Collaborations [4, 5]. They amount to about 15% of the total deep inelastic scattering events. In DDIS two different energy scales coexist: a soft one, $|t| < 1\ \mathrm{GeV}^2$, which is an energy scale characterizing the momentum transfer between the initial and final state proton, and a hard one, the photon virtuality $Q^2 \gg 1\ \mathrm{GeV}^2$. When the hard scale is present, it is allowed to apply perturbative QCD and understood such processes in terms of quarks and gluons. However, soft part of hard diffraction, responsible for the rapidity gap formation, stays outside perturbative QCD and is usually described using the Regge pole phenomenology. In this framework, the exchange of the so called *Regge trajectories* is given by the exchange of particles in the t-channel, which are summed coherently. Diffraction is characterized by the exchange of a specific trajectory, called a *pomeron*, which dominates at high energy and carries vacuum quantum numbers. The exchange of the pomeron is responsible for nonperturbative rapidity gap formation. Indeed, a very appealing interpretation of the rapidity gap relies upon a partonic interpretation of the structure of the pomeron. It is possible to nicely describe the diffractive cross-sections from HERA by a QCD DGLAP evolution of parton distributions in the pomeron, combined with a Regge parametrization of the flux factor describing the pomeron emission [6]. This interpretation is linked with the issue of diffractive parton distribution functions (DPDF) in diffractive deep inelastic scattering. The first part of this Thesis is devoted to the determination of the DPDF from fits to the HERA data.

Regge theory has also put forward a successful description of soft hadron-hadron scattering at high energies. The difference between diffraction at HERA and at the Tevatron is that diffraction at

the Tevatron can occur not only on either p or $\bar{p}$ side as at HERA, but also on both sides. The former case is called single diffraction, whereas the other one double pomeron exchange. It has been shown that the diffractive parton distributions from HERA can not be used directly to make predictions at the Tevatron. Indeed, factorization does not hold and a *gap survival probability* has to be considered. It corresponds to the probability that there are no additional soft interactions or in other words, that the event remains diffractive. The study of diffraction at the Tevatron and at the LHC is the subject of the second part of this Thesis.

The outline of the dissertation is the following.

Chapter 1 serves as an introduction in which we review basic facts concerning diffractive deep inelastic scattering and diffractive processes in hadron-hadron collisions. In this way, we establish the notation and present the standard approach to DIS in the framework of the collinear factorization. We also introduce the concept of the pomeron and the diffractive parton distribution functions.

In Chapter 2, we focus on the diffractive parton distribution functions. We determined these distributions from fits to the diffractive data from HERA. In our fits, in addition to the twist–2 contribution, the twist–4 contribution from longitudinally polarized virtual photons is considered, which is important in the region of small diffractive masses (large values of the parameter β). As a result, a new prediction for the longitudinal diffractive structure function, F_L^D, is made, which differs significantly from that obtained in the pure twist–2 analysis in the region of large β. Finally, we show a comparison for our predictions for F_L^D with the preliminary data from the H1 Collaboration at HERA.

In Chapter 3, we present a comprehensive analysis of the newest diffractive data using the dipole model approach. We consider two most popular parametrizations of the interaction between the diffractive system and the proton (the Golec-Biernat-Wüsthoff (GBW) and Color Glass Condensate (CGC) parametrizations) which are based on the idea of parton saturation. We present an updated and more consistent analysis which clearly shows the significance of the dipole models with parton saturation for the precise description of the diffractive HERA data .

In Chapter 4, we present the study of the heavy flavor production in diffractive deep inelastic scattering within the dipole models. We demonstrate that the present dipole models of DIS diffraction are able to describe the diffractive charm data from HERA provided we supplement them by a collinear factorization prescription for the generation of the diffractive state with a $c\bar{c}$ pair.

Chapter 5 is devoted to the diffractive dijet production. The diffractive parton distributions obtained from the QCD fits to the H1 [7] and ZEUS Collaboration data [8] allow us to make direct comparisons with measurements at the Tevatron. It is interesting to directly test the factorization breaking beetwen HERA and the Tevatron, using the measurements performed at both accelerators. We thus compare the extrapolations of the results of our and the H1 and ZEUS Collaboration fits to the recent CDF measurement of the single diffractive cross section for events with leading antiproton [7]. A special attention is paid to the role of the secondary reggeon contribution in the discussed results.

In Chapter 6, we study the electroweak boson production in hadron-hadron collisions. We show that the measurement of $W^{\pm}$ boson production asymmetry in rapidity in the diffractive pp collisions can serve as a test of the concept of the flavor symmetric parton distributions in the pomeron. In addition, this measurement may also be a valuable method to determine details of the parton distribution in the proton. The summary of the Thesis is given in Chapter 7.

The results discussed in this Thesis are based on the following publications:

- **"Diffractive parton distributions from the analysis with higher twist"**
  K. J. Golec-Biernat and A. Luszczak, Phys. Rev. D **76**, 114014 (2007)

- **"Dipole model analysis of the newest diffractive deep inelastic scattering data"**
  K. J. Golec-Biernat and A. Luszczak, Phys. Rev. D **79**, 114010 (2009)

- **"Diffractive hadroproduction of electroweak vector bosons at the LHC"**
  K. J. Golec-Biernat and A. Luszczak, Phys. Rev. D **81**, 014009 (2010)

The results of this Thesis were also presented by me at the following international conferences:

1. Results with diffractive parton distributions for the HERA, Tevatron and the LHC.
   Proceedings of Hadron Collider Physics Symposium, Evian, France, 16-20 November, 2009.

2. Diffractive asymmetry of electroweak vector bosons at the LHC.
   Proceedings of European Physical Society Europhysics Conference on High Energy Physics, EPS-HEP 2009, 16 - 22 July, 2009, Krakow,e-Print: arXiv:0911.0809 [hep-ph].

3. Diffractive open charm production from the dipole model analysis.
   Proceedings of European Physical Society Europhysics Conference on High Energy Physics, EPS-HEP 2009, 16 - 22 July, 2009, Krakow, e-Print: arXiv:0909.4077 [hep-ph].

4. Precise dipole model analysis of diffractive DIS.
   Proceedings of 17th International Workshop on Deep Inelastic Scattering and Related Subjects (DIS 2009), Madrid, Spain, 26-30 April 2009, e-Print: arXiv:0909.3956 [hep-ph].

5. Diffractive processes in electron-proton and proton-proton collisions.
   Proceedings of the XIII Mexican School of Particles and Fields, San Carlos, Sonora, Mexico, 2-11 October 2008, AIP Conf.Proc.1116:434-436, 2009.

6. Diffractive processes in electron-proton collisions at HERA.
   Proceedings of International Summer School and Conference on High Energy Physics: Standard Model and Beyond 15-22 September 2007, Akyaka, Turkey.

7. Diffractive parton distributions in electron-proton collisions at HERA.
   Prepared for International Workshop on Hadronic Final State and Parton Density Function, Hamburg, 24-26 October, 2006.

8. Diffractive structure function F_L from the analysis with higher twist.
   The Cracow Epiphany Conference, 4-6 January 2007, Acta. Phys. Polon. B **38**, 2331-2338 (2007).

Chapter 1

Introduction

1.1 Diffractive phenomena

In the 1950s, the term *diffraction* was introduced in high-energy nuclear physics. Among those by whom it was first used were Landau and Pomeranchuk [9–12]. The term is applied in strict analogy with the familiar optical phenomenon that is observed when a beam of light meets an obstacle and travels through a hole whose dimensions are comparable to its wavelength (if the wavelength is much smaller than these dimensions, geometrical shadowing is found to be taking place). It is shown schematically in Fig. 1.1. To the extent the propagation and the interaction of extended objects like the hadrons are insignificant but the absorption of their wave function caused by the many inelastic channels open at high energy the use of the optical terminology seems by all means appropriate [13]. Below, proper optical conditions for diffraction are presented.

Diffraction relies on a number of approximations. First of all, if a plane wave of wavelength λ hits a screen with a hole of dimensions R and the wave number $k = 2\pi/\lambda$ is sufficiently large, the *short wavelength condition*

$$kR \gg 1 \tag{1.1}$$

is satisfied. If the hole on the screen is described as Σ_0, then, according to the Huygens-Fresnel principle, each point becomes the center of a spherical wave, from whose envelope, the wave will be deflected. Let Σ is the plane at a distance D in which the image is collected (*i.e.* the detector plane). Due to the fact that distances to the point and angles with respect to the original direction of the beam vary, the amplitudes and phases of the waves collected at each point will also be different. Therefore, cancellations and reinforcements may occur at different points, giving rise to the phenomenon of diffraction. This propagation maps the value of this energy distribution T_0 on Σ_0 into its value T at the point $P(x, y, z)$ on the detector's plane. The Fresnel-Kirchhoff formula explains the mathematical aspect of this phenomenon [14]

$$T(x, y, z) = \frac{-i}{2\lambda} \frac{\mathrm{e}^{ik_0 r_0}}{r_0} \int_\Sigma dS\, T_0 \left\{1 + \cos\theta\right\} \frac{\exp i\vec{k} \cdot \vec{b}}{s} \tag{1.2}$$

where $\vec{s}$ is the distance of the point P from Σ_0 and $\cos\theta$ is the inclination of this vector with respect to the normal to Σ_0.

The problem is greatly simplified when the detector is so distant that all rays from Σ_0 to the point $P(x, y, z)$ on Σ can be considered to be parallel. Whether the term *Fraunhofer diffraction* or *Fresnel diffraction* is applied, depends on a distance to a source, more precisely, whether it can be considered infinitely large. The large distance approximation will always be valid for the case at hand. If the distance D satisfies the large distance condition

$$R/D \ll 1 \tag{1.3}$$

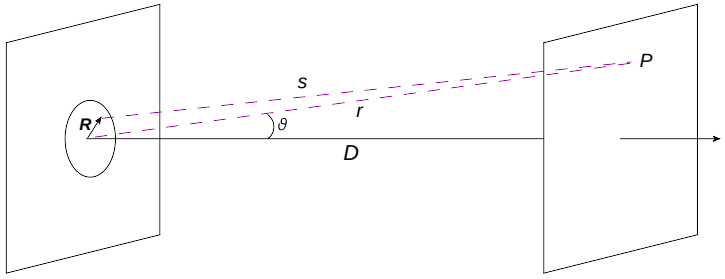

Figure 1.1: Diffraction of a plane wave by a hole in a screen

the exponential e^{iks}/s in power series of ks may be expanded. The following various cases can occur:

- Fraunhofer diffraction when $kR^2/D \ll 1$
- Fresnel diffraction when $kR^2/D \approx 1$
- geometrical optics when $kR^2/D \gg 1$

What follows, is that the optical regime is determined by the parameter kR^2/D. It needs to be pointed out that Fraunhofer diffraction is the focus of attention in terms of the application of optical concepts to hadronic phenomena.

Let us show the diffraction more precisely. On Fig. 1.2, by the light of wavelength λ impinging on a black disk of radius R_0, a diffraction pattern is produced on a distant screen. This pattern is characterized by a large forward peak for scattering angle $\theta = 0$ (the *diffraction peak*) and a series of symmetric minima and maxima, with the first minimum at $\theta_{\min} \simeq \pm\lambda/(2R_0)$ (Fig. 1.2). The intensity I as a function of the scattering angle θ is given by

$$\frac{I(\theta)}{I(\theta=0)} = \frac{[2J_1(x)]^2}{x^2} \simeq 1 - \frac{R_0^2}{4}(k\theta)^2, \tag{1.4}$$

in which J_1 is the Bessel function of the first order and $x = kR_0 \sin\theta \simeq kR_0\,\theta$ with $k = 2\pi/\lambda$. The diffraction pattern is, thus, related to the size of the target and the wavelength of the light beam.

The differential cross section $d\sigma/dt$ for elastic proton-proton scattering ($pp \to pp$) is remarkably similar to the diffraction pattern and is described in [15]. At low values of $|t|$, one has

$$\frac{\frac{d\sigma}{dt}(t)}{\frac{d\sigma}{dt}(t=0)} \simeq \mathrm{e}^{-b|t|} \simeq 1 - b\,(P\theta)^2, \tag{1.5}$$

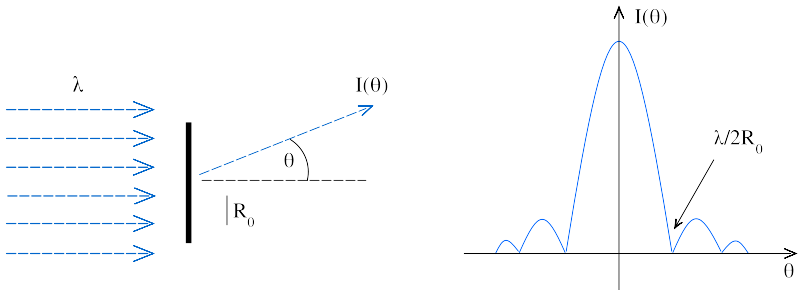

Figure 1.2: Distribution of the intensity I in the diffraction of light of wavelength λ from a circular target of size R_0.

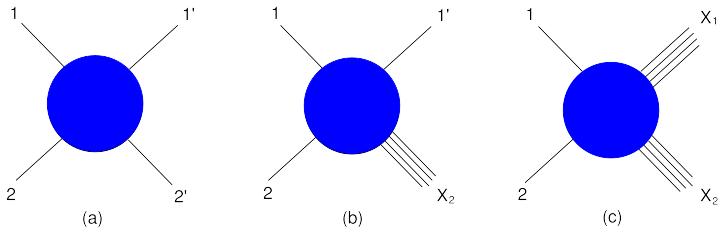

Figure 1.3: (a) Elastic scattering. (b) Single diffraction. (c) Double diffraction.

in which $|t| \simeq (P\theta)^2$ is the absolute value of the squared four-momentum transfer, P is the incident proton momentum and θ is the scattering angle. The t-slope b can be defined as $b = R^2/4$, in which once again R is related to the target size (or, more precisely, to the transverse distance between the projectile and target). A dip followed by a secondary maximum has also been observed. The dip appears to be decreasing with increasing proton momentum at the value of $|t|$. It is, hence, not surprising that the term diffraction is used for elastic pp scattering. Similar t distributions have been discovered for the other diffractive reactions mentioned above, leading to the use of the term diffraction for all such processes.

1.2 Definition of diffractive processes in particle physics

The next task will be to *define* diffraction in terms related to pure particle physics. The first authors to give a definition of relevant modern terms were Good and Walker [4]. For the sake of definiteness, it will be said that

- every reaction in which no quantum numbers are exchanged between high energy colliding particles is dominated asymptotically by diffraction.

Looking at the issue from a different point of view, one may imply that diffraction dominates as the energy increases anytime the diffused particles, or their ensembles, have the quantum numbers equal to those of the incident particles.

The request alone of no exchange of quantum numbers is a necessary condition for the process to be diffractive, but not a sufficient one. It is essentially impossible to define diffraction without any ambiguities whatsoever. A contamination of non-diffractive origin, such as the exchange of scalar particles, is always possible. However, it weakens asymptotically as the center-of-mass energy increases, and this is why in the definition above, it is explicitly demanded the process to be a high energy one.

Another advantage of this definition is that all cases of diffractive processes, shown in Fig. 1.3 and discussed later in the introduction, are covered by it, namely, elastic scattering, single diffraction and double diffraction.

One usually refers to a diffractive processes in particle physics, as a kind of processes which are dominated by the exchange of a *pomeron*. Here, *pomeron exchange* is synonymous with the exchange of no-quantum numbers. As it was mentioned above, our definition of diffraction is a little too simple. What is actually made possible by it, is differentiating between the true diffraction and the exchange of scalar systems which *a priori* are non-diffractive. However, the exchange of scalars gradually loses its importance while the energy increases.

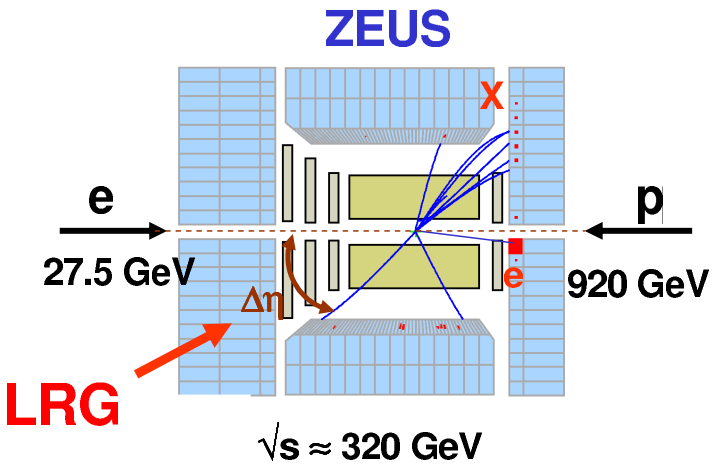

Figure 1.4: A DIS event with a large rapidity gap observed with the ZEUS detector at HERA. The scattered proton escapes into the beam pipe. The symbol $\Delta\eta$ denotes the difference in pseudorapidity between the scattered proton and the most forward particle of the observed hadronic system X.

1.2.1 Diffraction at HERA

HERA, a Collider in which 27.5 GeV electrons or positrons strike 820 or 920 GeV protons, was originally conceived as the machine by which the field of DIS would have been entirely cleared. As it turned out, it did not fail to deliver what had been promised and HERA was also the number one device to investigate diffraction in particle physics, triggering renewed interest in theoretical approaches to diffraction.

However, diffractive DIS has the advantage of being simpler since only one initial state hadron is involved. A typical diffractive event in DIS is shown in Fig. 1.4. In the theoretical interpretation of such events a virtual photon is radiated by an electron (or a Z or W boson), which then interacts with the proton. Looking at the scattering in a frame in which the virtual photon moves very fast (e.g. in the proton rest frame, in which the γ^* has a momentum of maximum 50 TeV at HERA), the virtual photon can fluctuate into a quark-antiquark pair. Because of its large Lorentz's boost, the lifetime of this virtual pair is much longer than that of a typical strong interaction time. In other words, the photon fluctuates into a pair long before the collision, and it is the pair that interacts with the proton. Diffractive events are possible because the interaction between the pair and the proton is mediated by the strong interaction with a net colorless exchange (vacuum quantum number exchange).

An advantage of studying diffraction in ep collisions is that, for sufficiently large photon virtuality Q^2, the typical transverse dimensions of the quark pair (colour dipole) are small if compared to the size of a hadron. Then, the interaction between the quark and the antiquark (as well as that of the pair and the proton) can be treated perturbatively. As Q^2 is decreasing, the colour dipole becomes larger, and at very low Q^2, these interactions strengthen so much that it is no longer possible to describe the process in terms of quarks and gluons. Instead, one may then regard the photon as fluctuating into a vector meson [16] (this is the basis of the well-known vector meson dominance model). It can, therefore, lead to the expectation that diffractive reactions are very similar to those in hadron-hadron scattering.

A different physical picture is obtained in a frame in which the incident proton is very fast. The diffractive reaction can be seen as the deep inelastic scattering (DIS) of a virtual photon on the proton target here, and in the final state of it the proton is very fast. Thus, it is likely that partons will be probed in the proton in a very specific way. There are actually different types of QCD-factorization theorems for such processes, by which certain expectations are confirmed. The collision of the virtual photon and the proton results in a hadronic final state X with the photon quantum numbers and invariant mass

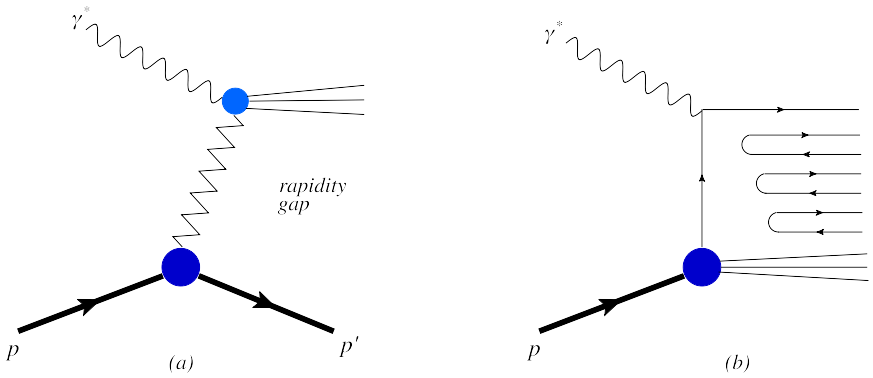

Figure 1.5: Diffractive (a) vs. inclusive (b) $\gamma^* p$ scattering.

M_X. A large gap in rapidity (or pseudorapidity) between X and the final-state proton is observed.

1.3 Diffractive deep inelastic scattering

In certain fraction of deep inelastic scattering events (about 10-15%) the target proton remains nearly intact. We speak, in these case, of diffractive deep inelastic scattering (DDIS). The process depicted in Fig. 1.5(a) is a semi-inclusive diffractive reaction, characterized by a particular final state configuration, wherein the presence of a rapidity gap between the scattered proton and the hadronic final state X signals that no quantum numbers are exchanged between the virtual photon and the incoming proton. In other words the main difference between these two processes is that, diffractive scattering is mediated by a pomeron, which carries vacuum quantum numbers and produces a rapidity gap. In inclusive case the rapidity space is completely filled, see Fig. 1.5(b).

Following diffractive processes, $ep \rightarrow e'Xp'$, in which X is a diffractive system, depicted in Fig. 1.6, are considered. There are several dimensional scales in diffractive DIS scattering. In addition to the photon virtuality Q^2 and total energy of the $\gamma^* p$ system W, which define the Bjorken variable

$$x = \frac{Q^2}{Q^2 + W^2}\,, \tag{1.6}$$

there are two additional invariant variables related to the diffractive nature of the process: the invariant mass of the diffractive system M^2 and the squared momentum transfer t. For the events, showed in this picture, the final state proton is well separated in rapidity from the rest of the system. The two new variables $x_{I\!P}$ and β, which are built out of above variables, are introduced. The variable

$$x_{I\!P} \;=\; \frac{Q^2 + M^2 - t}{Q^2 + W^2} \tag{1.7}$$

is a fraction of the incident proton momentum transferred into the diffractive system, and

$$\beta \;=\; \frac{Q^2}{Q^2 + M^2 - t}\,, \tag{1.8}$$

is an analogue of the Bjorken variable x for the diffractive system. Experimentally $|t| \ll Q^2, M^2$, thus t can be neglected in the above formulas.

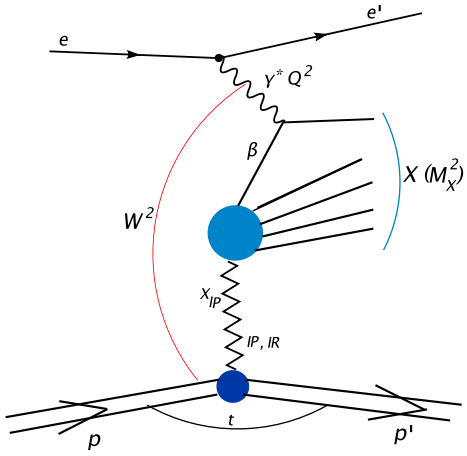

Figure 1.6: Kinematics of diffractive DIS in pomeron model.

The quoted interpretation of these variables can be derived from the two conditions resulting from the momentum conservation at the vertex with the diffractive system, see Fig. 1.6.

$$(x_{I\!P}p+q)^2 = M^2 \qquad => \qquad x_{I\!P} = \frac{M^2+Q^2}{2pq} = \frac{M^2+Q^2}{W^2+Q^2} \tag{1.9}$$

$$(q+\beta\,(x_{I\!P}p))^2 = 0 \qquad => \qquad \beta = \frac{Q^2}{M^2+Q^2} = \frac{x}{x_{I\!P}} \tag{1.10}$$

Notice that when $\beta \to 0$ then $M^2 \gg Q^2$ (diffractive mass is large), and when $\beta \to 1$ then $M^2 \ll Q^2$ (diffractive mass is small).

1.3.1 Diffractive structure functions

Diffractive structure function analogous to the inclusive case is defined. This is determined by the four invariant variables $(x, Q^2, x_{I\!P}, t)$ and defined with the use of the diffractive DIS cross section [17]

$$\frac{d^4\sigma^D}{dxdQ^2dx_{I\!P}dt} = \frac{2\pi\alpha_{em}^2}{xQ^4}\left\{[1+(1-y)^2]\frac{d^2F_2^D}{dx_{I\!P}dt} - y^2\frac{d^2F_L^D}{dx_{I\!P}dt}\right\}, \tag{1.11}$$

we introduce the following notation

$$F_2^{D(4)}(x,Q^2,x_{I\!P},t) \;=\; \frac{d^2F_2^D}{dx_{I\!P}dt}(x,Q^2,x_{I\!P},t), \tag{1.12}$$

$$F_L^{D(4)}(x,Q^2,x_{I\!P},t) \;=\; \frac{d^2F_L^D}{dx_{I\!P}dt}(x,Q^2,x_{I\!P},t), \tag{1.13}$$

in which it is explicitly indicated that the diffractive structure functions are dependent on four variables. In addition

$$F_2^{D(4)} = F_T^{D(4)} + F_L^{D(4)}, \tag{1.14}$$

It should be noticed that the introduced diffractive structure functions have dimension GeV^{-2} because of the differential dt in the definition of the cross section.

The structure functions integrated over t are also defined since they are measured when the final state proton momentum is not detected. In this case

$$F_{T,L}^{D(3)}(x, Q^2, x_{I\!P}) = \int_{-\infty}^{0} dt\, F_{T,L}^{D(4)}(x, Q^2, x_{I\!P}, t), \tag{1.15}$$

are dimensionless. The diffractive structure functions are related to the diffractive photon-proton cross sections in the following way

$$F_{T,L}^{D(4)}(x, Q^2, x_{I\!P}) = \frac{Q^2}{4\pi^2\alpha_{em}} \frac{d^2\sigma_{T,L}(\gamma^* p \to p' X)}{dx_{I\!P} dt}. \tag{1.16}$$

1.4 Regge approach to diffraction

1.4.1 Soft pomeron

The basic idea of Regge theory is that sequences of hadrons of mass m_i and spin j_i lie on Regge trajectories $\alpha(t)$ such that $\alpha(m_i^2) = j_i$. Prior to QCD, strong interactions were thought to be due to the exchange of complete trajectories of particles. In Regge model, all kinds of "soft" high energy hadronic scattering data: differential, elastic and total cross section measurements can be described successfully. The high energy behavior of a hadron scattering amplitude at small angles has the form

$$A(s,t) \;\sim\; \sum_R \beta(t)\, (s/s_0)^{\alpha_R(t)}, \tag{1.17}$$

where $s_0 = 1\ \mathrm{GeV}^2$ For the sake of simplicity, the signature factor is omitted. The variable s is the square of the centre-of-mass energy, whilst $-t$ is the square of the four-momentum transfer. The observed hadrons were found to be located on trajectories $\alpha_R(t)$, which are approximately linear in t and parallel to each other [18]. These hadrons have increasing spin and mass, but they do not differ as far as the other quantum numbers are concerned. They are found on a single trajectory $\alpha_R(t)$. The leading trajectories of this kind are the ρ, a_2, ω and f trajectories, all of them are approximately degenerate with the trajectory

$$\alpha_R(t) \;\simeq\; 0.5 \;+\; 0.9\,\mathrm{GeV}^{-2} \cdot t\,. \tag{1.18}$$

The Regge trajectories are shown in Fig. 1.7. For example, only the ρ trajectory has the appropriate quantum numbers to be exchanged in the process $\pi^- p \to \pi^0 n$. From the s dependence of the differential cross section $d\sigma/dt$, the trajectory $\alpha_\rho(t)$ can be determined for $t < 0$, see (1.17). For small $|t|$ the trajectory $\alpha_\rho(t)$ is found to be linear in t and, when extrapolated to positive t, it passes through the $\rho(1^-)$ and $\rho(3^-)\ldots$ states, i.e. $\alpha_\rho(m_\rho^2) = 1, 3, \ldots$ at the appropriate mass values. From the optical theorem, the total cross section (say, for $AB \to X$ scattering) is expressed in terms of the imaginary part of the forward elastic scattering amplitude. Total cross sections are observed to be slowly increase with s at high energies. In connection with that a higher lying trajectory with $\alpha_R \geq 1$ is required.

$$\sigma^{tot}(AB \to X) \;=\; \frac{1}{s}\mathrm{Im}A(s,0) \;=\; \frac{1}{s_0}\sum_R \beta_R\, (s/s_0)^{\alpha_R(0)-1}. \tag{1.19}$$

Vacuum quantum number exchange (pomeron) was introduced to account for the asymptotic energy dependence of the total cross sections [19]. Originally, the total cross sections were thought to asymptote to a constant at high energies and so a pomeron with the intercept $\alpha_{I\!P}(0) = 1$ was invoked. The slow rise at the total cross sections, however, needs $\alpha_{I\!P}(0) \simeq 1.08$. Due to introduction of a pomeron,

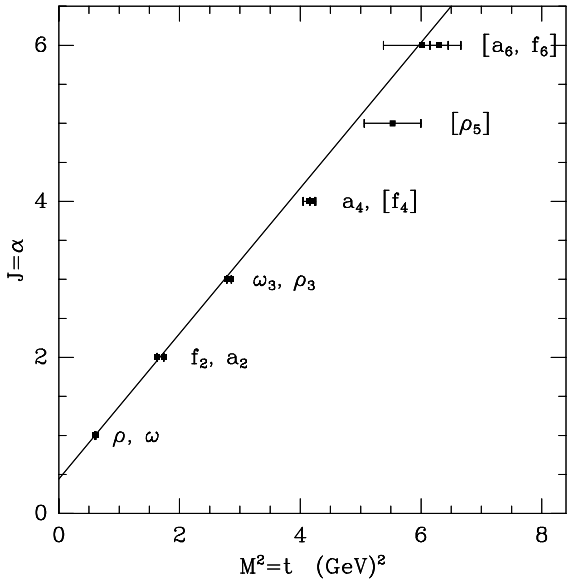

Figure 1.7: Regge trajectories.

the total, elastic and differential hadronic cross section data are found to be well described (for small $|t|$) by taking a universal pole form for the pomeron,

$$\alpha_{I\!P}(t) \;\simeq\; 1.08 \;+\; 0.25\,\mathrm{GeV}^{-2}\cdot t, \tag{1.20}$$

shown in Fig. 1.8 from [20]. The pomeron should be seen as an effective description only, since the $s^{0.08}$ power behavior of the total cross sections will ultimately violate the Froissart bound

$$\sigma^{tot}(AB \to X) \leq \frac{\pi}{m_\pi^2}\,\ln^2(s/s_0)\,. \tag{1.21}$$

where m_π is pion mass. The link between this successful Regge description of *soft* processes and the underlying fundamental theory of QCD is not yet known in detail. It is most likely that pomeron exchange is mainly originated from the exchange of a two-gluon bound state, whilst the meson trajectories (ρ, a_2, ω, f) correspond to $q\bar{q}$ bound states. The Regge theory pomeron discussed above is now frequently called the *soft pomeron*.

1.4.2 Triple Regge limit

Let us consider the single inclusive reaction, $1 + 2 \to 3 + X$, in the limit $s \gg M^2 \gg |t|$ in which M^2 is the invariant mass of the hadronic system X, see Fig. 1.9. The particle 3 is produced in the fragmentation region of particle 1. If 3 has the same quantum number as 1, such a process is called diffractive dissociation. In the limit $s \to \infty$, the scattering amplitude of the process is given by [13]

$$A(12 \to 3X) = \sum_i g_{13}^i(t)\, g_{2X}^i(t)\, \eta_i(t) \left(\frac{s}{M^2}\right)^{\alpha_i(t)}, \tag{1.22}$$

where the sum is done over the contributing reggeons, $\eta_i(t)$ is the corresponding signature factor and $g_{13}^i(t)$ and $g_{2X}^i(t)$ factors describe the coupling of the reggeons to the external particles. According to

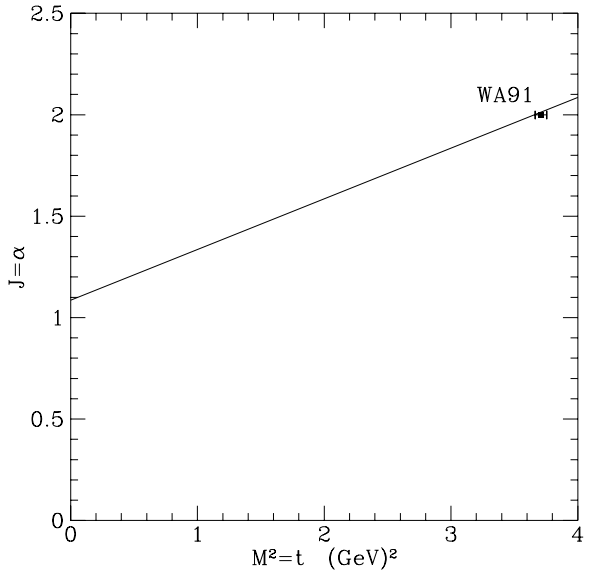

Figure 1.8: Pomeron trajectory.

Mueller generalized optical theorem, the DIS cross section is related to the corresponding scattering amplitude in the following way

$$\begin{aligned} 16\pi^2 s \frac{d^2\sigma^{SD}}{dM^2 dt} &= \frac{1}{s} \mathrm{Disc}_{M^2} A(12\overline{3} \to 12\overline{3}) \\ &= \frac{1}{s} \sum_{ij} g^i_{13}(t)\, g^{j*}_{13}(t)\, \eta_i(t)\, \eta^*_j(t) \left(\frac{s}{M^2}\right)^{\alpha_i(t)+\alpha_j(t)} \mathrm{Disc}_{M^2} A(i2 \to j2)\,, \end{aligned} \tag{1.23}$$

where $A(i2 \to j2)$ is the reggeon-particle scattering amplitude. Its discontinuity, in the limit $M^2 \to \infty$, is predicted by the Regge theory to be

$$\mathrm{Disc}_{M^2} A(i2 \to j2) = \sum_k g^k_{22}(0)\, g_{ijk}(t) \left(\frac{M^2}{s_0}\right)^{\alpha_k(0)} . \tag{1.24}$$

Note that reggeons i and j carry the momentum squared t, whereas k carries no momentum. In Eq. (1.24) g_{ijk} is the triple-reggeon coupling and s_0 is an arbitrary reference scale. Inserting Eq. (1.24) into Eq. (1.23) gives in the triple Regge limit $s \gg M^2 \gg |t|$ and $s, M^2 \to \infty$:

$$\begin{aligned} 16\pi^2 s \frac{d^2\sigma^{SD}}{dM^2 dt} &= \frac{1}{s} \sum_{ijk} g^i_{13}(t)\, g^{j*}_{13}(t)\, \eta_i(t)\, \eta^*_j(t) \left(\frac{s}{M^2}\right)^{\alpha_i(t)+\alpha_j(t)} \\ &\times \; g^k_{22}(0)\, g_{ijk}(t) \left(\frac{M^2}{s_0}\right)^{\alpha_k(0)} \\ &= \sum_{ijk} G_{ijk}(t) \left(\frac{s}{M^2}\right)^{\alpha_i(t)+\alpha_j(t)-1} \left(\frac{M^2}{s_0}\right)^{\alpha_k(0)-1}, \end{aligned} \tag{1.25}$$

where in the last line all the couplings and signatures were incorporated into the functions $G_{ijk}(t)$.

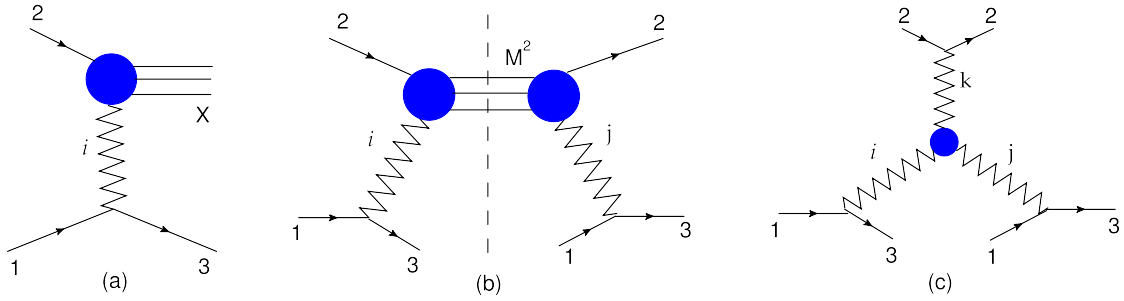

Figure 1.9: (a) Single-inclusive reaction $1 + 2 \to 3 + X$ mediated by the exchange of a reggeon i. (b) The discontinuity across M^2 of the scattering amplitude. (c) The triple reggeon diagram.

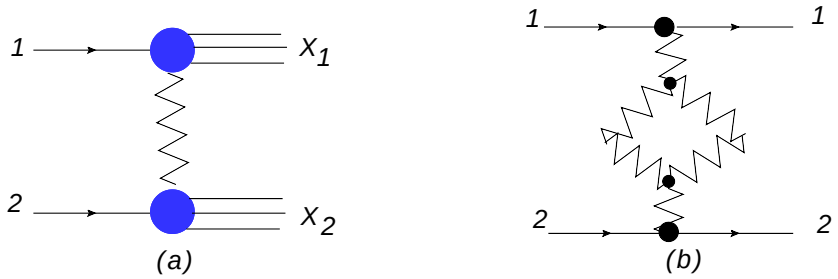

Figure 1.10: (a) Double diffractive dissociation. (b) The pomeron loop (a discontinuity is to be taken across the loop).

Let us focus now on a specific single-inclusive reaction, $12 \to 1'X_2$ in the limit of high energy $s \to \infty$. This process is called diffractive if the outgoing particle is equal to one of the incoming particles and carries most of its momentum, and the hadronic state X_2 has the same quantum numbers as the other incoming particle. In this case the two trajectories that we previously called i and j (i.e.,those exchanged between particles 1 and 2) are the pomeron trajectory: $\alpha_i(t) = \alpha_j(t) = \alpha_{I\!P}(t)$. The trajectory k can be either a pomeron or another reggeon $I\!R$ with the trajectory $\alpha_{I\!R}(t)$ (the former dominates when M^2 is very large). Therefore, we have

$$\begin{aligned} 16\pi^2 s \frac{d^2\sigma^{SD}}{dM^2 dt} &= G_{I\!P I\!P I\!P}(t) \left(\frac{s}{M^2}\right)^{2\alpha_{I\!P}(t)-1} \left(\frac{M^2}{s_0}\right)^{\alpha_{I\!P}(0)-1} \\ &+ G_{I\!P I\!P I\!R}(t) \left(\frac{s}{M^2}\right)^{2\alpha_{I\!P}(t)-1} \left(\frac{M^2}{s_0}\right)^{\alpha_{I\!R}(0)-1} . \end{aligned} \tag{1.26}$$

Another inclusive process, shown on Fig. 1.10, is double diffractive dissociation (DD): $12 \to X_1 X_2$, where X_1 and X_2 carry the same quantum numbers of particles 1 and 2, respectively (from the experimental point of view, the reaction is characterized by a large rapidity gap between X_1 and X_2). If the masses M_1^2 and M_2^2 of the produced states are large, we can proceed as for single diffraction, and we find that the process is dominated by a pomeron loop, which arises from gluing together two triple pomeron diagrams. Regge factorization relates the cross section of double diffraction dissociation to the cross section single diffractive dissociation and elastic scattering in the following way

$$\frac{d\sigma^{DD}(12\to X_1X_2)}{dM_1^2dM_2^2dt}=\frac{d\sigma^{SD}(12\to X_12)}{dM_1^2dt}\,\frac{d\sigma^{SD}(12\to 1X_1)}{dM_2^2dt}\,/\,\frac{d\sigma_{el}(12\to 12)}{dt}\,. \tag{1.27}$$

We shall make use of the Regge theory predictions for diffractive dissociation presented above, when discussing diffractive deep inelastic scattering (DDIS).

1.4.3 DDIS from Regge theory

It will now be proved that the results on single inclusive process, discussed above, lead to Regge theory predictions for diffractive DIS. The correspondence between the general reaction $1+2\to 3+X$ and DDIS is shown in Fig. 1.11. Particles 1 and 3 are now the incoming p and outgoing proton p', respectively while particle 2 is the virtual photon γ^*. in Eq. (1.25), the center-of-mass energy squared of γ^*p scattering is denoted by W^2 and the replacement $M^2\to(M^2+Q^2)$ must be made in order to take photon virtuality into account. In addition, Q^2 is also chosen for the reference scale s_0.

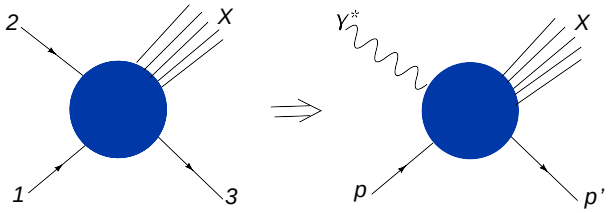

Figure 1.11: From hadronic diffractive dissociation to diffractive DIS.

For $W^2\gg M^2,Q^2\gg|t|$, DDIS is described by the triple Regge diagrams, see Fig. 1.12. There are two dominant contributions, shown in Fig. 1.13, which are described by the triple-pomeron, $I\!P I\!P I\!P$, and the pomeron-pomeron-reggeon, $I\!P I\!P I\!R$, diagrams. The diffractive deep inelastic cross section then reads

$$\begin{aligned} W^2\,\frac{d^2\sigma^{SD}}{dM^2dt}, \;&=\; A_{I\!P}(t)\left(\frac{W^2}{M^2+Q^2}\right)^{2\alpha_{I\!P}(t)-1}\left(\frac{M^2+Q^2}{Q^2}\right)^{\alpha_{I\!P}(0)-1}\\ &+\; A_{I\!R}(t)\left(\frac{W^2}{M^2+Q^2}\right)^{2\alpha_{I\!P}(t)-1}\left(\frac{M^2+Q^2}{Q^2}\right)^{\alpha_{I\!R}(0)-1}, \end{aligned} \tag{1.28}$$

in which all couplings are incorporated into the functions $A_{I\!P,I\!R}$. In particular, considering only the triple pomeron case we have

$$W^2\,\frac{d^2\sigma^{SD}}{dM^2dt}=\frac{1}{16\pi^2}|g_{I\!P}(t)|^2\left(\frac{W^2}{M^2+Q^2}\right)^{2\alpha_{I\!P}(t)-1}g_{I\!P}(0)\,g_{3I\!P}(t)\left(\frac{M^2+Q^2}{Q^2}\right)^{\alpha_{I\!P}(0)-1}, \tag{1.29}$$

where $g_{3I\!P}$ is the triple-pomeron coupling. For the sake of simplicity, it is assumed that the pomeron couples in the same way to the proton and to the virtual photon. The triple-pomeron mass spectrum in the large mass limit is given by

$$\frac{d^2\sigma^{SD}}{dM^2\,dt}\sim\frac{1}{(M^2+Q^2)^{\alpha_{I\!P}(0)}}\sim\frac{1}{(M^2)^{\alpha_{I\!P}(0)}}\sim\frac{1}{(M^2)^{1+\epsilon}}, \tag{1.30}$$

for the pomeron with the trajectory $\alpha_{I\!P}(0)=1+\epsilon$.

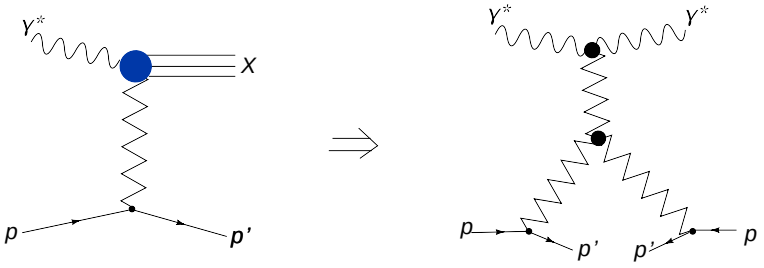

Figure 1.12: Diffractive $\gamma^* p$ scattering and the triple Regge diagram that describes it in the limit$W^2 \gg M^2, Q^2 \gg t$.

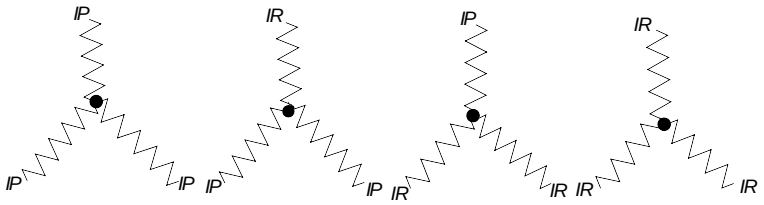

Figure 1.13: Triple Regge diagrams contributing to diffraction dissociation.

Since t is limited and the triple-pomeron coupling does not depend much on it, the approximation $g_{3I\!P}(t) \backsimeq g_{3P}(0)$ can be made. Inserting the variable $x_{I\!P} \backsimeq M^2/W^2$, Eq. (1.29) can be rewritten as

$$\frac{d^2\sigma^{SD}}{dx_{I\!P}dt} = f_{I\!P}(x_{I\!P}, t)\, \sigma_{\gamma^* I\!P}(M^2, Q^2), \tag{1.31}$$

in which

$$f_{I\!P}(x_{I\!P}, t) = \frac{1}{16\pi^2} |\, g_{I\!P}(t)|^2\, x_{I\!P}^{1-2\alpha_{I\!P}(t)}, \tag{1.32}$$

is the pomeron flux factor and

$$\sigma_{\gamma* I\!P}(M^2, Q^2) \;=\; g_{3I\!P}(0)\, g_{I\!P}(0) \left(\frac{M^2+Q^2}{Q^2}\right)^{\alpha_{I\!P}(0)-1}, \tag{1.33}$$

is the γ^*-pomeron scattering cross section. If the variable $\beta \simeq Q^2/M^2$ is used, Eq. (1.31) becomes

$$\frac{d\sigma^{D}}{dx_{I\!P}dt} = f_{I\!P}(x_{I\!P}, t)\, \sigma_{\gamma^* I\!P}(\beta, Q^2), \tag{1.34}$$

in which

$$\sigma_{\gamma* I\!P}(\beta, Q^2) = A_{I\!P}(Q^2)\, \beta^{1-\alpha_{I\!P}(0)}. \tag{1.35}$$

It needs to be noted that the Q^2 dependence which is embodied in $A_{I\!P}(Q^2)$ is actually irrelevant in the context of the Regge theory, in which the virtuality of the photon is a fixed parameter (a mass) and one cannot predict the dependence of the cross section on Q^2. What is actually predicted in the Regge theory, is the β dependence of $\sigma_{\gamma^* I\!P}$ at fixed Q^2. The interesting feature of Eq. (1.34) is the factorization of the $x_{I\!P}$ dependence from the β dependence, called *Regge factorization*. This is an important and highly non-trivial prediction based on the Regge theory that the dependence on $x_{I\!P}$, i.e.

in W^2, is completely determined by the flux factor. With $\alpha_{I\!P} = 1 + \epsilon$, the diffractive cross section behaves as

$$\frac{d\sigma^D}{dx_{I\!P}dt} \sim \frac{1}{(x_{I\!P})^{1+2\epsilon}}, \tag{1.36}$$

In terms of the diffractive structure function $F_2^{D(4)}$ Eq. (1.34) can be rewritten as

$$F_2^{D(4)}(x_{I\!P}, t, \beta, Q^2) = f_{I\!P}(x_{I\!P}, t)\, F_2^{I\!P}(\beta, Q^2), \tag{1.37}$$

in which $F_2^{I\!P}$ is the so called *pomeron structure function*. The triple Regge limit expectation for the β dependence of $F_2^{I\!P}$ in the limit $\beta \to 0$ is given by

$$F_2^{I\!P}(\beta, Q^2) \sim \beta^{1-\alpha_{I\!P}(0)} \sim \beta^{-\epsilon}, \tag{1.38}$$

Integrating Eq. (1.37) over t, $F_2^{D(3)}$ can be put in the factorized form

$$F_2^{D(3)}(x_{I\!P}, \beta, Q^2) = \overline{f}_{I\!P}(x_{I\!P})\, F_2^{I\!P}(\beta, Q^2), \tag{1.39}$$

where the t-integrated pomeron flux is given by

$$\overline{f}_{I\!P}(x_{I\!P}) = \int_{-\infty}^{0} dt\, f_{I\!P}(x_{I\!P}, t). \tag{1.40}$$

In practical measurements, the t-integration has a limited range due to experimental conditions.

1.5 Partonic structure of the pomeron

It is tempting to interpret the quasi-elastic high-energy scattering of photon fluctuation and proton in terms of pomeron exchange, thus introducing a soft energy dependence. Essentially, one assumes that the pomeron (just like a real hadron) can be characterized by a parton distribution (Ingelman and Schlein model [21]). This distribution is assumed to factorize from the pomeron trajectory and the pomeron-proton-proton vertex, which are both obtained from the analysis of purely soft hadronic reactions. At leading order, the pomeron structure function is given as a superposition of quark and antiquark distributions in the pomeron

$$F_2^{I\!P}(\beta, Q^2) = \sum_{i=1}^{N_f} e_i^2\, \beta \left[q_{i/I\!P}(\beta, Q^2) + \overline{q}_{i/I\!P}(\beta, Q^2) \right], \tag{1.41}$$

where the sum is performed over quark flavors. The variable $\beta = x/x_{I\!P}$ is interpreted as the fraction of the pomeron momentum carried by its partonic constituents and $q_{i/I\!P}(\beta, Q^2)$ is the probability to find, inside the pomeron, a quark of flavor i with the momentum fraction β. Clearly, this interpretation makes sense only insofar as the probability of finding a pomeron in the proton can be specified clearly and with certainty (i.e., the pomeron flux). It also needs to be viable that the pomeron is a real particle. Since it is not so, the whole picture must be regarded as a purely phenomenological one combining Regge factorization and QCD-factorization.

The Q^2 dependence of the quark and the gluon density in the pomeron is governed by the Dokshitzer-Gribov-Lipatov-Altarelli-Parisi (DGLAP) evolution equations [22,23], which can be written in following way:

$$Q^2 \frac{\partial}{\partial Q^2} \begin{pmatrix} \Sigma^{I\!P}(\beta, Q^2) \\ g^{I\!P}(\beta, Q^2) \end{pmatrix} = \frac{\alpha_s(Q^2)}{2\pi} \int_\beta^1 \frac{dz}{z} \begin{pmatrix} P_{qq} & 2n_f P_{qg} \\ P_{gq} & P_{gg} \end{pmatrix} (\beta/z, \alpha_s(Q^2)) \begin{pmatrix} \Sigma^{I\!P}(z, Q^2) \\ g^{I\!P}(z, Q^2) \end{pmatrix}, \tag{1.42}$$

where by $\Sigma^{I\!P}(\beta, Q^2)$ we mean the sum of quarks and anti-quarks of all flavors, *i.e.* the so called *singlet quark distribution*

$$\Sigma^{I\!P}(\beta, Q^2) = \sum_{i=1}^{N_f} \left[q_{i/I\!P}(\beta, Q^2) + \overline{q}_{i/I\!P}(\beta, Q^2) \right]. \tag{1.43}$$

We symbolically denoted the dependence of the splitting functions P_{ij} under the integral on the parton momentum fractions β/z and the scale Q^2. The above equation is an analogue of the renormalization group equation for evolution of the running coupling $\alpha_s(Q^2)$. Similarly to the renormalization group equation, it allows to calculate the change of the parton distribution functions with a scale, but the absolute value at a given scale cannot be determined without specifying initial conditions for the evolution, which are not provided by the theory itself.

The problem in the analysis of both DIS and DDIS data is that only perturbative QCD (pQCD) at small distances (that means, at large Q^2) can be used. Within pQCD, one can study the evolution of parton distributions, but the initial distributions at some relatively low scale $Q_0 \gg \Lambda_{QCD}$ are of non-perturbative origin and, at present, have to be determined by fitting to the data. A factorization theorem underlies the analysis. It enables the amplitude to be factored into two parts, one purely in the pQCD domain, and the other parametrized by a phenomenological ansatz. In terms of Feynman diagrams, the factorization is based on the resummation of the series of the most important higher-order corrections where the small coupling α_S is enhanced by a large logartithm $\ln(Q^2/Q_0^2)$. That is, it is possible to divide such diagrams, at a "logarithmic loop or cell", into a part depending only on large scales from a part containing the low scale.

1.5.1 From partonic pomeron to diffractive parton distributions

Having introduced the pomeron parton distributions, the diffractive structure functions can also be written in the terms of the diffractive parton distributions in the proton, for the quarks

$$\mathcal{F}^D_{i/p}(x_{I\!P}, t, \beta, Q^2) = \frac{1}{16\pi^2} |g_{I\!P}(t)|^2 \, x_{I\!P}^{-2\alpha_{I\!P}(t)} \, q_{i/I\!P}(\beta, Q^2), \tag{1.44}$$

and for the gluons

$$\mathcal{F}^D_{g/p}(x_{I\!P}, t, \beta, Q^2) = \frac{1}{16\pi^2} |g_{I\!P}(t)|^2 \, x_{I\!P}^{-2\alpha_{I\!P}(t)} \, g^{I\!P}(\beta, Q^2), \tag{1.45}$$

Now, in the leading logarithmic (in Q^2) approximation the diffractive structure function is given by

$$F_2^{D(4)}(x_{I\!P}, t, \beta, Q^2) = \sum_{i=1}^{N_f} e_i^2 \, \beta \, x_{I\!P} \left[\mathcal{F}^D_{i/p}(x_{I\!P}, t, \beta, Q^2) + \overline{\mathcal{F}}^D_{i/p}(x_{I\!P}, t, \beta, Q^2) \right]. \tag{1.46}$$

At the next-to-leading order the above formula acquires a term containing diffractive gluon distribution $\mathcal{F}^D_{g/p}$. The particular form of the diffractive parton distributions, *i.e.* that the $(x_{I\!P}, t)$ dependence is factorized from the (β, Q^2) dependence, *e.g.*

$$x_{I\!P} \, \mathcal{F}^D_{i/p}(x_{I\!P}, t, \beta, Q^2) = f_{I\!P}(x_{I\!P}, t) \, q_{i/I\!P}(\beta, Q^2), \tag{1.47}$$

is only an assumption reflecting Regge factorization. This factorization allows to introduce the model of DDIS with the pomeron as a quasi-real particle with partonic structure.

In general, the diffractive parton distributions are objects which are firmly rooted in perturbative QCD. They are conditional probabilities describing diffractive process with a hard scale. For example, the diffractive parton distribution $\mathcal{F}^D_{i/p}(x_{I\!P}, t, \beta, Q^2)$ is the probability of finding, in a fast moving

proton, a parton with flavor i and the momentum fraction $x = x_{I\!P} \cdot \beta$, under the additional requirement that the proton remains intact while being scattered with invariant momentum transfer t and losing a small fraction $x_{I\!P}$ of its longitudinal momentum. A precise and consistent determination of the diffractive PDFs and their uncertainties is very important for making predictions of cross sections of hard diffractive processes at the LHC.

It should be mentioned, however, that there is a strong theoretical obstacle to apply straightforwardly the diffractive parton distributions to hadronic processes. Soft gluonic interactions between the colliding partons in the incoming hadrons lead to contributions which spoil a simple description with partonic distributions by adding additional nonpartonic terms. An effective way to describe such soft processes is to consider a gap survival factor which diminishes cross sections computed with the diffractive parton distributions.

1.5.2 Soft vs hard pomeron

The soft pomeron is the vacuum quantum number exchange described in the Regge theory by the rightmost pole of the elastic scattering amplitude $A(s,t)$ in the complex momentum plane j, *i.e.* after performing the Mellin transform with respect to s, the amplitude behaves in the following way close to the pomeron pole at $j = \alpha_{I\!P}(t)$,

$$A(j,t) \sim \frac{1}{j - \alpha_{I\!P}(t)}\,, \tag{1.48}$$

where $\alpha_{I\!P}(t)$ is given by Eq. (1.20). From the optical theorem, the asymptotic behavior of the total cross section for $s \to \infty$ is determined by the pomeron intercept $\alpha_{I\!P}(0) = 1.08$:

$$\sigma^{tot} \sim s^{\alpha_{I\!P}(0)-1} = s^{0.08}\,. \tag{1.49}$$

Such a power-like behavior, however, ultimately violates the Froissart bound (1.21), which takes into account unitarity of the scattering amplitude. Thus, the soft pomeron behavior contradicts unitarity for asymptotically large energies, and the agreement of presently measured total cross sections with the soft pomeron behavior is only a reflection of a preasymptotic region of s in the experiments preformed up till now. The diffractive data from the Tevatron, however, are more sensitive to unitarity corrections (which take into account cuts in addition to a simple pomeron pole) than the data on σ^{tot}. This is why the diffractive data are so important. More details on this aspect will be given in the forthcoming section on diffraction in hadron-hadron collisions.

The observation of diffractive processes with hard scale at HERA (with large Q^2 or heavy vector meson mass M_V) or at the Tevatron (diffractively produced jets with large transverse momentum k_T) invoke QCD to describe these processes in terms of the QCD pomeron. The simplest picture of the vacuum quantum number exchange which dominates in the high energy limit is provided by two exchanged gluons in the color singlet state. Virtual corrections lead to the BFKL pomeron in the form of an infinite gluon ladder with non-local vertices and rungs being reggeized gluons. Formally, the BFKL pomeron emerges as a solution to the BFKL equation. The scattering amplitude of two colorless objects with the BFKL pomeron exchanged gives a powerlike behavior on s, stronger than for the soft pomeron. In the leading logarithmic in s approximation $\alpha_{I\!P}(0) = 1 + 4N_c\alpha_s \ln 2/\pi$, and

$$\sigma^{tot} \sim s^{\alpha_{I\!P}(0)-1} \simeq s^{0.5}, \tag{1.50}$$

for $N_c\alpha_s/\pi = 0.2$ and $N_c = 3$ quark colors. The next-to-leading order corrections to the BFKL equation reduce the power to $0.2 - 0.3$, nevertheless, strong unitarity corrections are necessary to be in agreement with the Froissart bound. Such corrections go beyond the gluon ladder picture and need multiple gluon exchanges in t-channel.

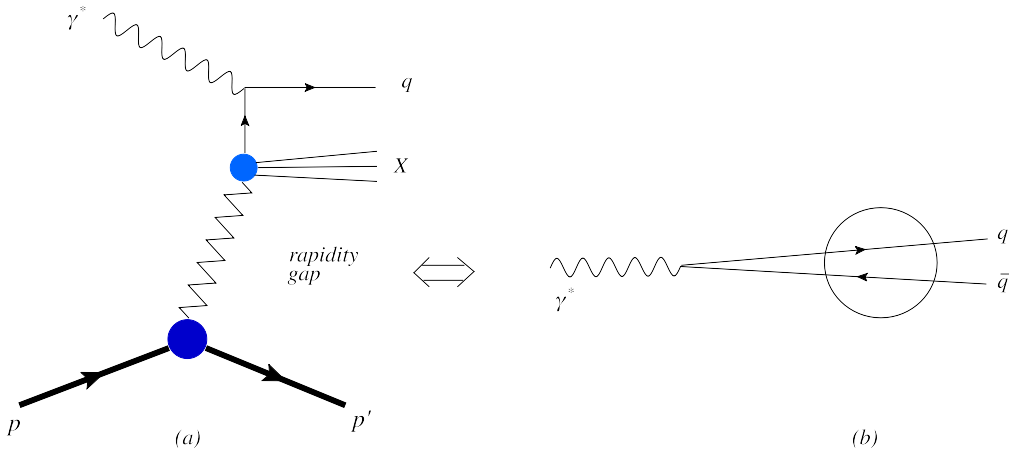

Figure 1.14: Partonic structure of the pomeron vs. color dipole fluctuations of the photon.

Thus, crucial difference between *soft*, phenomenological pomeron and the *hard*, BFKL pomeron is the intercept, much bigger in the latter case . One can ask here, whether the soft pomeron is intrinsically distinct from the hard pomeron. That, however, would not actually be a well posed questions. The answer to that, in fact, depends on the definition of the pomeron. On the one hand, in perturbative QCD, pomeron is synonymous with a *ladder of interacting reggeized gluons*. On the other hand, in phenomenological approaches, such as those from which the soft intercept comes out, the pomeron is not associated to a physical object, but is generically understood as something that must lie behind a successful, and amazingly simple, parametrization of a vast series of data. Quite obviously, comparing these two concepts of pomeron and understanding their mutual relationships, is just impossible. The missing information is relevant to the physical picture underlying the soft pomeron. This is clearly determined by the non-perturbative structure of the pomeron about which very little is known.

DDIS is particularly sensitive to the pomeron energy behavior since the diffractive scattering amplitudes are squared in the diffractive cross sections. Thus, unitarization effects play more important role than for the total cross section which is proportional to the imaginary part of the scattering amplitudes. This observation was a basis of successful description of the first diffractive data from HERA in which the diffractive system was formed by the quark-antiquark ($q\overline{q}$) and quark-antiquark-gluon ($q\overline{q}g$) systems which could be viewed as dipoles in the space of Fourier transformed transverse momenta [24]. The pomeron was modelled by the two-gluon exchange which was subsequently substituted (unitarized) by the effective dipole–proton cross section [25].

1.5.3 Is pomeron a particle?

One may find it tempting to interpret diffractive $\gamma^* p$ processes as the scattering a virtual photon on a pomeron which has been radiated off the initial proton. Diffractive DIS would then probe the distribution of partons in a *pomeron target*. This is what Ingelman and Schlein proposed in their model [21]. Nevertheless, this idea is contrary to an analysis in QCD (see e.g. [26]). As it was discussed in the previous section, the high-energy scattering in QCD is dominated by the exchange of two gluons, whose interaction is described by ladder diagrams. By analyzing these diagrams in terms of time-ordered perturbation theory, the dominant space-time ordering in the high-energy limit may be obtained. The result is determined by the reference frame. In the Breit frame (natural for a parton-model interpretation), the photon does *not* scatter off a parton in a pre-existing two-gluon system. Actually, some of the interactions which build up in the gluon ladder in pomeron exchange take place long after the

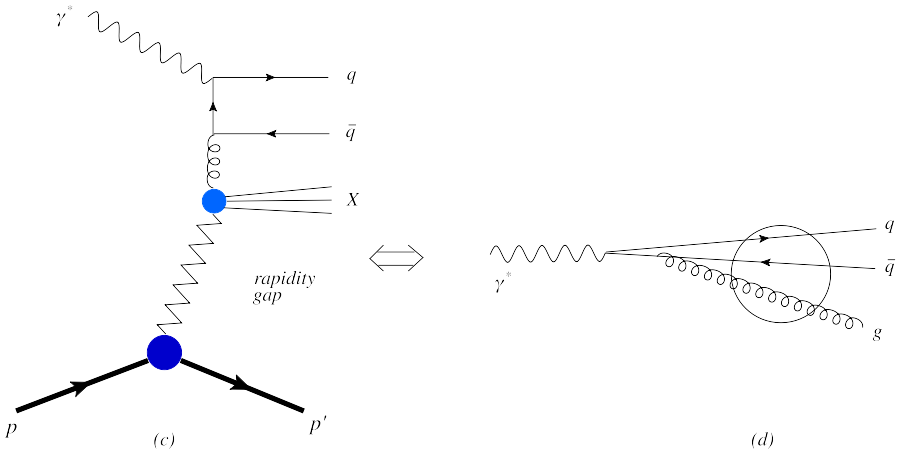

Figure 1.15: Partonic structure of the pomeron vs. color dipole fluctuations of the photon.

absorption of the virtual photon. The picture in the Breit frame is, however, compatible with the interpretation of diffractive parton distributions, namely the probability to find a parton under the condition that subsequent interactions, will produce a fast proton in the final state.

Since the pomeron is not a particle, its parton distributions do not satisfy energy-momentum conservation. Moreover, the pomeron flux is ambiguously defined (up to the normalization) and so are the parton distributions of the pomeron. What can be adopted, is a point of view mentioned in the previous section, the color dipole approach. From this perspective, probing the quark and antiquark distributions of the pomeron corresponds to considering the $q\overline{q}$ excitations of the virtual photon and their interaction with the proton via two-gluon (or the BFKL ladder) exchange. The gluonic contribution to the pomeron structure function is reinterpreted in terms of $q\overline{q}g$ fluctuations of the photon. The correspondence between the infinite-momentum frame picture of diffractive DIS (wherein the internal structure of the pomeron is resolved) and the proton rest frame description (wherein the hadronic fluctuations of the photon are involved) is sketched in Fig. 1.14 and Fig. 1.15. One ought to note, nevertheless, that the QCD formulas which define the diffractive parton distributions fail to take into account higher-twist contributions. These instead emerge in the colour dipole approach and turn out to be non-negligible for large values of β.

1.6 Dipole approach

The colour dipole formalism has been developed as an alternative to the Feynman diagram approach to small x physics. It is formulated in impact parameter space and has been shown to reproduce Feynman diagram results for inclusive processes in the Regge limit, as embodied in the BFKL equation. With regard to gluon radiation in diffraction it can be applied in the triple Regge limit, *i.e.* for large diffractive masses only, $M^2 \gg Q^2$.

In QCD the pomeron in its simplest form is represented by two gluons since the minimum number of gluons to form a colourless state is two. It is not excluded that more than two gluons are exchanged and it is important that whenever we talk about two-gluon exchange to remember, there is the possibility to extend the formalism to multigluon exchange. One might object that the whole process is soft and perturbation theory not applicable. Saturation effects for high parton densities, however, screen soft contributions, so that a fairly large fraction of the cross section is hard and therefore eligible for a perturbative treatment.

The intuitive picture behind the dipole picture of DDIS is the following. In the target (proton) rest

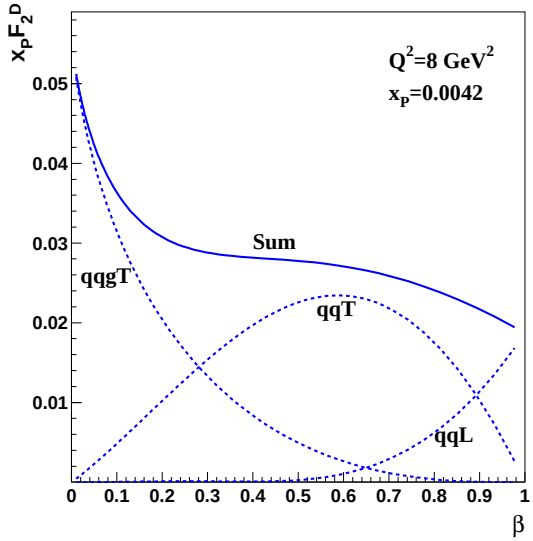

Figure 1.16: The three components of the diffractive structure function as a function of β.

frame the virtual photon dissociates into a $q\bar{q}$-pair far upstream the proton target. The $q\bar{q}$-pair may radiate a gluon, forming a $q\bar{q}g$ state, and the whole parton configuration scatters quasi-elastically off the proton via a colorless gluon exchange (two gluons in the simplest case). The timescale on which the fluctuation occurs is proportional to $1/(xm_p)$ where m_p is the proton mass. At very small x, the fluctuation is long lived whereas the scattering is a sudden short impact of the $q\bar{q}$-pair or the $q\bar{q}g$-final state, which eventually form a diffractive state, on the target. The impact changes the virtual into a real state but it does not change the position in impact parameter space which can be viewed as being frozen during the scattering. The significance of the $q\overline{q}$ and $q\overline{q}g$ diffractive states produced from transverse or longitudinaly polarized virtual photons in DIS is shown in Fig. 1.16. Hence

$$F_2^D = F_T^{q\overline{q}} + F_L^{q\overline{q}} + F_T^{q\overline{q}g}\,, \tag{1.51}$$

and each component has its own dominance region for the diffractive structure function F_2^D:

- the $q\overline{q}$ component from transverse photons, $F_T^{q\overline{q}}$, dominates for $\beta \sim 1/2$ when $M^2 \sim Q^2$
- the $q\overline{q}$ component from logintudinal photons, $F_L^{q\overline{q}}$, dominates for $\beta \to 1$ when $M^2 \ll Q^2$
- the $q\overline{q}g$ component from transverse photons, $F_T^{q\overline{q}g}$ dominates for $\beta \to 0$ when $M^2 \gg Q^2$.

It should be noticed that the $F_L^{q\overline{q}}$ component is especially important for large β since it goes to a constant value as $\beta \to 1$ [27]. Formally, it is a twist-four contribution to the longitudinal structure function F_L^D which, however, appears to be important numerically. This twist-four contribution goes beyond the leading twist-two approximation with the diffractive parton distributions, however, due to its numerical importance it cannot be neglected in any analysis of DDIS. In Section 2 we will present such an analysis with higher twist.

1.7 Diffractive dissociation in hadron-hadron collisions

In hadron-hadron scattering, a substantial fraction of the total cross section is due to diffractive reactions. Diffractive dissociation is a special case of inclusive production in a quasi two-body process,

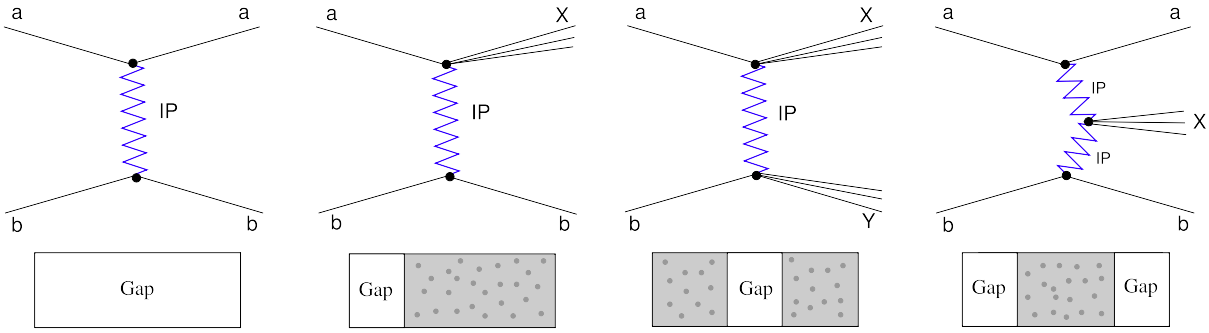

Figure 1.17: Elastic scattering, single and double diffractive dissociation, and double pomeron exchange in the collision of two hadrons a and b. The two groups of final state hadrons are separated by a large rapidity gap (LRG). The zigzag lines denote the exchange of a pomeron ($I\!P$) in the t-channel.

wherein all quantum numbers (charge, isospin, strangeness etc.) of the final states are the same as for initial hadrons. Spin and parity can, of course, be different since orbital angular momentum can be transferred in the collision.

In Fig. 1.17, the different types of diffractive processes in the collision of two hadrons are shown. In *elastic scattering*, both projectiles emerge intact in the final state, whereas *single* (SD) or *double diffractive dissociation* (DD) corresponds to one or both of them being scattered into a low-mass state. The latter has the same quantum numbers as the initial hadron and may be a resonance or continuum state [16]. In all cases, the energy of the outgoing hadrons a, b or the states X, Y is approximately equal to that of the incoming beam particles, to within a few percent. The two (groups of) final-state particles are well separated in phase space and, in particular, have a large gap in rapidity between them. The scheme of inclusive *double pomeron exchange* (DPE) is also shown in Fig. 1.17.

Diffractive dissociation, therefore, is closely connected with elastic scattering, as it may be visualized by the quasi two-body reaction: for *single diffraction* $a + b \to b' + X$. Double diffraction occurs when both incoming particles a and b are excited to systems with the same initial quantum numbers: $a + b \to X + Y$. Whenever the basic conditions for single or double diffraction are satisfied, the differential cross sections exhibit a sharp forward peak.

Fig. 1.18 taken from [29], collects the existing measurements of the single diffractive cross section, σ_{SD}, which does not continue to increase with energy following triple-Regge behavior (which would eventually violate unitarity). The observed flattening of the integrated single-diffraction cross section has been attributed by Goulianos [29] to the saturation of the pomeron flux factor $f_{I\!P}(x_{I\!P}, t)$. In other terms, it is suggested that $f_{I\!P}(x_{I\!P}, t)$ integrated over $x_{I\!P}$ and t should not exceed unity. Therefore, above some energy value ($\sqrt{s} = 22$ GeV), $f_{I\!P}(x_{I\!P}, t)$ is renormalized, and this gives the solid curve in Fig. 1.18. If one reinterprets the pomeron flux as rapidity probability (recall that the rapidity gap $\Delta y = \ln(1/x_{I\!P})$), renormalizing the pomeron flux is equivalent to demanding that the integrated gap probability be always smaller than 1. The integrated double diffractive cross section σ_{DD} seems to scale with $\sqrt{s}$ in a similar way [30].

1.8 Hard diffraction at the Tevatron

The first suggestion of hard diffractive events in hadron-hadron collisions appeared in a paper by Ingelman and Schlein [21] in 1985. They presented a model of high-p_T jet production via pomeron exchange, responsible for diffraction. In this way, a model of pomeron with partonic structure which gives rise to two jets was proposed.

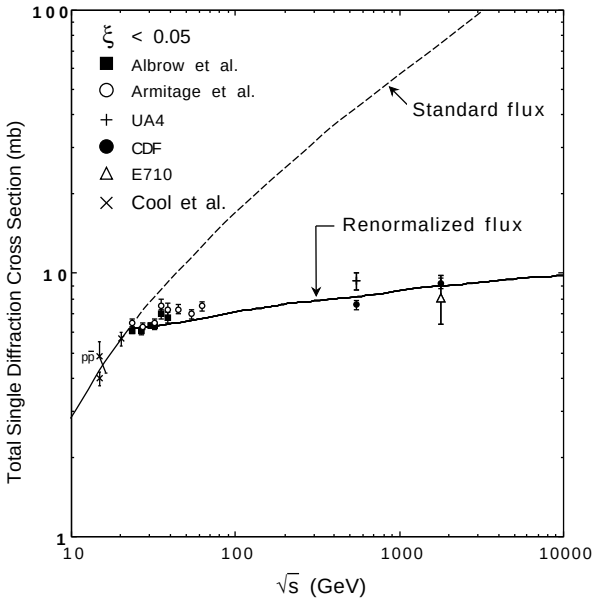

Figure 1.18: The total single diffractive cross sections versus $\sqrt{s}$ compared with the predictions of the renormalized pomeron flux model of Goulianos [28].

Hard diffraction program in hadron-hadron scattering has been pursued by the UA8 Collaboration at the CERN SPS Collider [31], and by the CDF and D0 Collaborations at the Tevatron [2, 32]. The general situation is illustrated in Fig. 1.17. Dijets can be observed in single and double diffraction or being centrally produced via double pomeron exchange.

1.8.1 Single diffraction

The signature of hard single diffraction(SD) at the Tevatron is two jets produced on the same side and either a forward rapidity gap along the direction of one of the initial particles. From a phenomenological point of view, the single dissociation process $\overline{p}p \to \overline{p}X$ is described by assuming that a pomeron is emitted by the incident antiproton and undergoes a hard scattering with the proton. This is an ideal reaction to study the partonic content of the pomeron, that is the β dependence of the diffractive structure functions [13]

$$F_{jj}^{D} = \frac{1}{x_{I\!P max} - x_{I\!P min}} \int_{x_{I\!P min}}^{x_{I\!P max}} dx_{I\!P}\, f_{I\!P}(x_{I\!P})\, \beta \Big\{ g^{I\!P}(\beta) + \frac{4}{9} \sum_{f} \Big[q_{f/I\!P}(\beta) + \overline{q}_{f/I\!P}(\beta) \Big] \Big\}. \quad (1.52)$$

As we will see in Chapter 5, the substitution of the pomeron parton distributions, determined from the diffractive HERA data, overshoots the experimental results by a factor of 10. This questions universality of the diffractive parton distributions, resulting form the QCD collinear factorization, and calls for a modification which takes into account the gap survival factor.

1.8.2 Double diffraction

Rapidity gaps between jets were proposed by Dokshitzer, Khoze and Troyan [33] and Bjorken [34] as a signature of color-singlet exchange. Events of this type are predominantly of diffractive nature, since

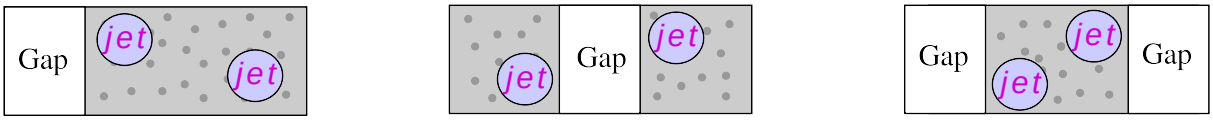

Figure 1.19: Diffractively produced dijets in single, double diffraction and in double pomeron exchange.

the contribution from electroweak processes, which would give a similar configuration is small.

The CDF and D0 experiments have collected dijet data with central rapidity gaps [2,32] and found the diffractive to non diffractive production ratio to be about 1% at energy $s = 1.8$ GeV, that is 10 times smaller than the diffractive rate measured at HERA.The decrease of the double diffractive contribution with increasing energy can be explained by introducting the concept of the gap survival factor.

1.8.3 Double pomeron exchange (DPE)

The first observation of dijet production via double pomeron exchange (DPE) in $p\overline{p}$ collisions was reported by the CDF Collaboration [35]. The events are characterized by a leading antiproton, two jets in the central pseudorapidity region with transverse energy $E_T > 7$ GeV and a large rapidity gap on the outgoing proton side. The ratio of the DPE to SD rates R_{SD}^{DPD} was determined as a function of the proton Bjorken variable x_B. In leading order QCD, R_{SD}^{DPD} is equal to the ratio of the diffractive to non-diffractive color weighted structure functions of the proton. Thus assuming collinear factorization one should have:

$$R_{SD}^{DPD} = R_{ND}^{SD}. \tag{1.53}$$

However, from CDF data this equality is not fulfilled since:

$$R_{ND}^{SD}/R_{SD}^{DPD} \approx 0.2\,. \tag{1.54}$$

1.9 Gap survival factor

The survival probability of a rapidity gap in hard diffraction, S^2, is defined as the fraction of events for which the soft interactions between the quark spectators in the colliding hadrons do not fill the gap.

The survival probability is easily defined in the eikonal model in the impact parameter space. Let as assume that $f(s,t)$ denote the elastic $2 \to 2$ scattering amplitude, and s and t be standard Mandelstam variables. Its normalization is defined such that the elastic and total cross sections are defined as

$$\frac{d\sigma_{el}}{dt} = \pi |f(s,t)|^2 \tag{1.55}$$

$$\sigma_{tot} = 4\pi \mathrm{Im}\, f(s,0), \tag{1.56}$$

The scattering amplitude Fourier transformed into the impact parameter space is given by

$$a(s,\mathbf{b}) = \frac{1}{2\pi}\int d^2\mathbf{q}\, \mathrm{e}^{-i\mathbf{q}.\mathbf{b}} f(s,t), \tag{1.57}$$

where $\mathbf{q}$ is the transverse momentum of the scattered particles and $t \simeq -\mathbf{q}^2$. It is easy to derive that in the $b-$space:

$$\sigma_{el} = \int d^2\mathbf{b}\, |a(s,b)|^2, \tag{1.58}$$

and

$$\sigma_{tot} = 2 \int d^2\mathbf{b}\, \mathrm{Im}\, a(s,b)\,. \tag{1.59}$$

The condition of $s-$channel unitarity implies the following relation

$$2\mathrm{Im}\, a(s,b) = |a(s,b)|^2 + G_{in}(s,b), \tag{1.60}$$

where $G_{in}(s,b)$ is related to inelastic processes since from Eqs. (1.58) and (1.59) we obtain for the inelastic cross section, $\sigma_{in} = \sigma_{tot} - \sigma_{el}$,

$$\sigma_{in} = \int d^2\mathbf{b}\, G_{in}(s,b)\,. \tag{1.61}$$

The $s-$channel unitarity relation (1.60) also implies that

$$0 \leq G_{in}(s,b) \leq 1\,. \tag{1.62}$$

s-channel unitarity is most easily enforced in the eikonal approach. Assuming that $a(s,b)$ is purely imaginary, we can write

$$a(s,b) = i(1 - \mathrm{e}^{-\Omega(s,b)}), \tag{1.63}$$

where the eikonal $\Omega(s,b)$, called opacity, is a real function. From Eq. (1.60) we can compute

$$G_{in}(s,b) = 1 - \mathrm{e}^{-2\,\Omega(s,b)}\,, \tag{1.64}$$

thus the quantity

$$P(s,b) = \mathrm{e}^{-2\,\Omega(s,b)}, \tag{1.65}$$

may be interpreted as the probability that no inelastic interaction takes place at impact parameter b.

We follow Bjorken [34] and define the gap survival probability as

$$S^2 = \frac{\int d^2\mathbf{b}\, |a_H(s,b)|^2\, P(s,b)}{\int d^2\mathbf{b}\, |a_H(s,b)|^2}, \tag{1.66}$$

where $a_H(s,b)$ denotes the amplitude associated with hard collisions and $P(s,b)$ is the probability that no other interaction takes place in the rapidity interval of interest. Some preliminary calculations of S^2 have been presented by Bjorken in Ref. [34]

$$S^2 \approx 0.05 - 0.10 \qquad \mathrm{at} \qquad \sqrt{s} = 1.8\ \mathrm{TeV}\,. \tag{1.67}$$

Similar values are found by Gotsman, Levin and Maor [36] who used various phenomenological models. It is reasonable to expect that S^2 varies with energy , in particular that it decreases with increasing $\sqrt{s}$, since the interactions between the particle remnants become stronger and tend to destroy the gap. The comprehensive analysis of the gap survival energy dependence can be found in [37].

Chapter 2

Diffractive parton distributions from the analysis with higher twist

As it was mentioned in Chapter 1, a very interesting example of the interplay between hard and soft aspects of QCD-interactions is provided by the diffractive deep inelastic scattering at HERA. On the one hand, the virtuality of the photon probe Q^2 is hard (much bigger than Λ^2_{QCD}), whilst on the other hand, the scattered proton remains intact, and only a small fraction of the initial longitudinal momentum is lost. Its transverse momentum with respect to the photon-proton collision axis is small. The ratio of the diffractive and inclusive DIS cross sections is, to a good approximation, a constant as a function of energy of the gamma-proton system or as a function of the photon virtuality. The latter fact reflects the logarithmic dependence of the DDIS structure functions on Q^2 in the Bjorken limit.

The diffractive interactions can be viewed as a colourless, vacuum quantum number exchange between the diffractive system and the proton, in the t-channel picture. In the old days of Regge phenomenology, such a *mechanism* of interactions, which dominates in the high energy limit, was termed a *pomeron*, see Section 1.4. With the advent of QCD, a new way of understanding the pomeron by modelling it with the help of gluon exchanges, projected onto the colour singlet state, became possible. In the lowest approximation, the pomeron is a two-gluon exchange, independent of energy. If radiative corrections of this process in the high energy limit (typical of diffraction) are studied, it is necessary to take into account an infinite set of diagrams. This leads to the famous BFKL pomeron [38–41], introduced in Section 1.5.2. One of its features is a strong dependence on energy. This dependence ultimately violates unitarity, which means that exchanges with more gluons need to be considered. A systematic program which sums up exchanges with gluon number changing vertices was formulated in [42, 43] and developed in [44–47]. Another and more intuitive formulation (Colour Glass Condensate [48, 49], see also [50, 51] for a review) is based on the idea of parton saturation [52] in which DDIS is observed on a dense gluonic system in the proton. In every one of the approaches discussed here, unitarization is supposed to change the asymptotic energy behavior of the cross sections involving the pomeron from power-like to logarithmic. DDIS displays an especially strong sensitivity to the pomeron energy behavior due to the fact that the diffractive scattering amplitudes are squared in the diffractive cross sections.

Therefore, unitarization effects are more important here than in case of the total cross section which is proportional to the imaginary part of the scattering amplitudes. As a consequence of this observation, the basis of successful description of the first diffractive data from HERA was formed: in this way, the diffractive system was formed by first Fock components of the light-cone wave function of the virtual photon, namely quark-antiquark ($q\overline{q}$) and quark-antiquark-gluon ($q\overline{q}g$) systems which can be viewed as dipoles in the space of Fourier transformed transverse momenta [24]. The pomeron was modelled by the two-gluon exchange, which was subsequently substituted (unitarized) by the effective

dipole-proton cross section [25].

According to the alternative approach to DDIS, the diffractive structure functions are expressed in terms of the diffractive parton distributions (DPD), evolving in Q^2 with the DGLAP evolution equations [22,23,53]. Here, the diffractive structure functions depend logarithmically on Q^2 in the Bjorken limit, and that means that they provide the twist-2 description of DDIS. The theoretical justification of this approach can be found in the collinear factorization theorem, valid for hard diffractive scattering in ep collisions [54–58]. Nevertheless, collinear factorization is ineffective in hadron-hadron scattering due to non-factorizable soft interactions between the initial hadrons [18, 59]. Thus, unlike inclusive parton distributions, DPD are not universal objects. They can only be safely used for the description of diffractive processes in the ep DIS. The relation between the dipole approach with the $q\overline{q}$ and $q\overline{q}g$ diffractive components and the DGLAP-based description was studied in detail in [60]. In short, after extracting the twist-2 part, the dipole approach provides Q^2-independent quark and gluon DPD. Moreover, the $q\overline{q}g$ component, which was computed, assuming strong ordering between transverse momenta of the gluon and the $q\overline{q}$ pair, gives the first step in the Q^2-evolution of the gluon distribution.

In this sense, the two component dipole picture is extended by the twist-2 approach based on the DGLAP-equations, taking into account more complicated diffractive final state. In the DGLAP-based analysis, performed so far, the diffractive parton distributions were determined through fits to the diffractive HERA data [7]. This approach will now be followed by an important modification. We included into our analysis twist-4 contribution, which is not taken into account in previous descriptions of diffractive parton distributions.

The seemingly subleading twist-4 contribution, given by the $q\overline{q}$ pair from longitudinally polarized virtual photons $(Lq\overline{q})$, is revealed. Formally, it is suppressed by a power of $1/Q^2$ with respect to the leading twist-2 transverse contribution. Nevertheless, the perturbative QCD calculation shows that for a small diffractive mass M^2, when $\beta = Q^2/(M^2+Q^2) \to 1$, the longitudinal component dominates over the twist-2 one which vanishes in this limit. The effect of the $Lq\overline{q}$ component is particularly important for the longitudinal diffractive structure function F_L^D, which has been already determined from the high luminosity run data at HERA. That is why, we claim that it is absolutely necessary to consider the twist-4 contribution in the determination of the diffractive parton distributions through the DGLAP fits.

The relevance of this issue for predicting F_L^D is confirmed by the analysis presented here, which makes it significantly different from the predictions based on the pure DGLAP analysis. This is the main goal of the study presented in this chapter.

We start from introducing the diffractive parton distributions in Section 2.1. Subsequently, we explain the main features of Ingelman-Schlein model and Reggeon contribution, respectively, in Sections 2.2 and 2.3. In Sections 2.4 we describe the tree contributions: twist–2, twist–2 charm, twist–4 and the Reggeon contribution which we included in the description of the diffractive structure functions. In Section 2.5 and 2.6 we provide details of the preformed fits to HERA data and show the results of the diffractive parton distributions and diffractive structure functions from fits with and without the twist-4 contribution. Predictions for the longitudinal diffractive structure function are presented in Section 2.8. Finally, the conclusions are given in Section 2.9.

The results presented in Sections 2.5- 2.8 are based on the original publication [61].

2.1 Diffractive parton distribution formalism

Let us now come back to the diffractive parton distributions $\mathcal{F}_{a/p}^D$ from Section 1.5.1, which are now introduced according to the collinear factorization formula [62],

$$F_2^{D(4)}(x,Q^2,x_{I\!P},t) \;=\; \sum_a \int_0^{x_{I\!P}} d\xi\; \mathcal{F}_{a/p}^D(\xi,\mu^2,x_{I\!P},t)\; \mathcal{C}_a(x/\xi,Q^2/\mu^2)\,, \tag{2.1}$$

with $a = q, \bar{q}, g$ denoting a quark, antiquark (of different flavors) or gluon distributions in the proton, respectively. In the infinite momentum frame, the diffractive parton distributions describe the probability to find a parton with the fraction ξ of the proton momentum, provided the proton stays intact and loses only a small fraction $x_{I\!P}$ of its original momentum. $\mathcal{C}_a$ are the coefficient functions describing hard scattering of the virtual photon on a parton a. They are identical to the coefficient functions known from inclusive DIS,

$$\mathcal{C}_a(x/\xi, Q^2/\mu^2) \,=\, e_a^2\,\delta(1-x/\xi) \,+\, \mathcal{O}(\alpha_s)\,. \tag{2.2}$$

Formula (2.1) is an analogue of the inclusive leading twist description for inclusive DIS. The inclusive structure function F_2 is factorized in a similar way into computed in pQCD coefficient functions and nonperturbative parton distributions. The scale μ^2 is the factorization/renormalization scale. In the next step we find the renormalization group equations (evolution equations) for the diffractive parton distribution [60]

$$\mu^2\,\frac{d}{d\mu^2}\,\mathcal{F}^D_{a/p}(\xi,\mu^2,x_{I\!P},t) \,=\, \sum_b \int_\xi^{x_{I\!P}} \frac{dz}{z}\,P_{ab}(\xi/z,\alpha_s(\mu^2))\,\mathcal{F}^D_{b/p}(z,\mu^2,x_{I\!P},t)\,, \tag{2.3}$$

where P_{ab} are the standard Altarelli-Parisi splitting functions in leading or next-to-leading logarithmic approximation. Since the scale μ is arbitrary, we can choose $\mu = Q \gg \Lambda_{QCD}$. With this scale the evolution equations are usually presented.

The integration in (2.1) and (2.3) is only done up to the fraction $x_{I\!P}$ of the proton momentum, since the active parton cannot carry more than this fraction of momentum. The proton remnants carry the remaining fraction $(1 - x_{I\!P})$. If we refer the longitudinal momenta of the partons to $x_{I\!P}p$ instead of the proton total momentum p, the structure functions and parton distributions become functions of $\beta = x/x_{I\!P}$ or $\beta' = \xi/x_{I\!P}$. With this notation, we rewrite (2.1) and (2.3) in the following form:

$$F_2^{D(4)}(\beta,Q^2,x_{I\!P},t) \,=\, \sum_a \int_0^1 d\beta'\; x_{I\!P}\mathcal{F}^D_{a/p}(\beta',\mu^2,x_{I\!P},t)\;\mathcal{C}_a(\beta/\beta',Q^2/\mu^2) \tag{2.4}$$

and

$$\mu^2\,\frac{d}{d\mu^2}\,\mathcal{F}^D_{a/p}(\beta,\mu^2,x_{I\!P},t) \,=\, \sum_b \int_\beta^1 \frac{dz}{z}\,P_{ab}(\beta/z,\alpha_s(\mu^2))\,\mathcal{F}^D_{b/p}(z,\mu^2,x_{I\!P},t)\,. \tag{2.5}$$

Thus, we obtain a description similar to inclusive DIS but modified by the additional variables $x_{I\!P}$ and t. Moreover, the Bjorken variable x is replaced by its diffractive analogue β, Eq. (1.8). Notice that $x_{I\!P}$ and t play the role of parameters of the evolution equations and does not affect the evolution. According to the factorization theorem the evolution equations (2.5) are applicable to all orders in perturbation theory.

In the lowest order approximation for the coefficient functions (2.2), we find for the diffractive structure function

$$F_2^{D(4)}(x,Q^2,x_{I\!P},t) \,=\, \sum_{a=q,\overline{q}} e_a^2\;\beta\;x_{I\!P}\mathcal{F}^D_{a/p}(\beta,Q^2,x_{I\!P},t)\,, \tag{2.6}$$

where the sum over the quark/antiquark flavors is performed.

The collinear factorization formula (2.4) holds to all orders in α_s for diffractive DIS [55]. However, this is no longer true in hadron–hadron hard diffractive scattering [18, 59], where collinear factorization fails due to final state soft interactions. Thus, unlike inclusive scattering, the diffractive parton distributions are no universal quantities. The can safely be used, however, to describe hard diffractive processes involving leptons. can only be used in the description of diffractive DIS. A systematic approach to diffractive parton distributions, based on quark and gluon operators, is given in [54,56,63].

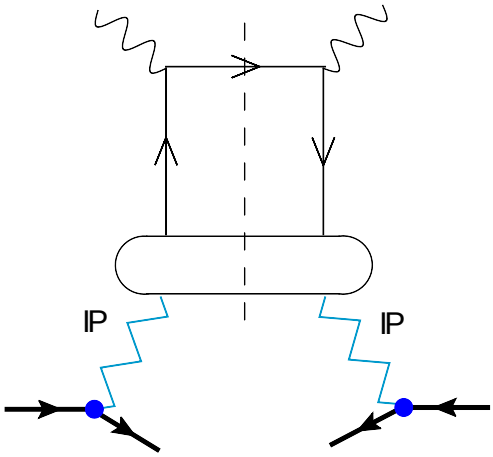

Figure 2.1: Diffractive structure function in the Ingelman-Schlein model. The spring-like lines represent the pomeron.

2.2 The Ingelman-Schlein model

Until now, we have not referred to the pomeron. In the Ingelman-Schlein (IS) model [21], diffraction is described with the help of the concept of the soft pomeron exchange. In addition, it is assumed that the pomeron has a hard structure. In DIS diffraction, this structure is resolved by the virtual photon, as in the standard DIS processes. Following the results of Regge theory, the IS model is based on the assumption of *Regge factorization*. In the context of the diffractive parton distributions it means that the following factorization holds [54, 62, 63]

$$x_{I\!P}\mathcal{F}^D_{a/p}(\beta, Q^2, x_{I\!P}, t) \;=\; f_{I\!P}(x_{I\!P}, t)\, q_{a/I\!P}(\beta, Q^2)\,, \tag{2.7}$$

The structure function (2.7 is schematically shown in Fig. 2.1. The "pomeron flux" (1.32) is now parametrized as

$$f_{I\!P}(x_{I\!P}, t) \;=\; \frac{B^2_{I\!P}(t)}{8\pi^2}\, x_{I\!P}^{1-2\alpha_{I\!P}(t)}\,. \tag{2.8}$$

Thus, the variables $(x_{I\!P}, t)$, related to the loosely scattered proton, are factorized from the variables characterizing the diffractive system (β, Q^2). $B_{I\!P}(t)$ is the Dirac electromagnetic form factor [20], describing the pomeron coupling to the proton,

$$B^2_{I\!P}(t) \;=\; B^2_{I\!P}(0)\, \mathrm{e}^{-B_D|t|}\,. \tag{2.9}$$

where $B^2_{I\!P}(0) \;=\; 54.4\ GeV^{-2}$ [64] and $B_D \;=\; 5.5\ GeV^{-2}$ [7]. In the IS model the soft pomeron trajectory (1.20) is used [65].

The function $q_{a/I\!P}(\beta, Q^2)$ describes the hard structure in DIS diffraction and is interpreted as the pomeron quark distribution. The pomeron parton distributions are determined as the parton distributions of real hadrons. Therefore, some functional form with several parameters is assumed at an initial scale and then the parameters are found from a fit to data [7,66] using the DGLAP evolution equations.

In summary, the diffractive structure function (2.6) in the IS model becomes

$$F_2^{D(4)}(x, Q^2, x_{I\!P}, t) \;=\; f_{I\!P}(x_{I\!P}, t) \sum_a e_a^2\, \beta\, q_{a/I\!P}(\beta, Q^2)\,, \tag{2.10}$$

where the summation over quark/antiquark flavors is performed. The Q^2 evolution of $q_{a/I\!P}(\beta, Q^2)$ is given by the DGLAP equations (2.5) while the t-dependence in the pomeron quark distributions is neglected.

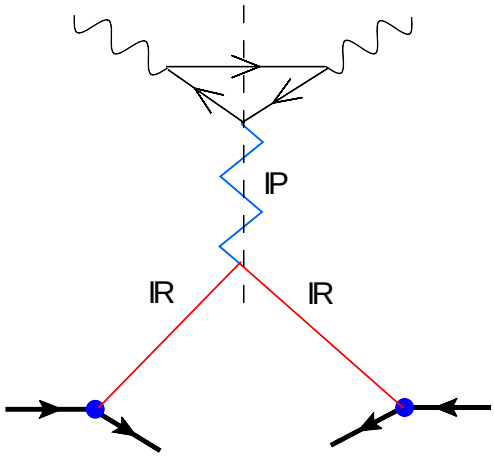

Figure 2.2: The reggeon-reggeon-pomeron contribution to diffractive structure function.

2.3 Reggeon contributions

The exchange of subleading reggeons can account for the Regge factorization breaking of diffractive structure function for large values of $x_{I\!P} > 0.01$. Strictly speaking, we cannot call such processes diffractive since diffraction is usually associated with the leading pomeron exchange. However, for simplicity we use the same terminology for the non-pomeron exchanges, including the isospin changing process with neutron instead of the proton in the final state. The reggeon contribution is shown in Fig. 2, which illustrates the following extension of the Ingelman-Schlein model [67]

$$F_2^{D(4)}(x, Q^2, x_{I\!P}, t) \;=\; f_{I\!P}(x_{I\!P}, t) \sum_{a=i} e_a^2\, \beta\, f_{a/I\!P}(\beta, Q^2) \;+\; \sum_R f_R(x_{I\!P}, t)\, F_2^R(\beta, Q^2) \qquad (2.11)$$

where the non-pomeron terms describe reggeon exchanges, isoscalar (f_2, ω) and isovector (a_2, ρ), with the trajectory

$$\alpha_R(t) = 0.5475 + 1\ \text{GeV}^{-2} \cdot t \qquad (2.12)$$

in the reggeon flux

$$f_R(x_{I\!P}, t) \;=\; \frac{B_R^2(t)}{8\,\pi^2} |\eta_R(t)|^2\, x_{I\!P}^{1-2\,\alpha_R(t)}\,, \qquad (2.13)$$

where $\eta_R(t)$ is a signature factor:

$$|\eta_R(t)|^2 \;=\; \begin{cases} 4\,\cos^2[\pi\alpha_R(t)/2] & \text{for even signature reggeons } (f_2, a_2) \\ \\ 4\,\sin^2[\pi\alpha_R(t)/2] & \text{for odd signature reggeons } (\rho, \omega)\,. \end{cases} \qquad (2.14)$$

The function $B_R(t)$ describes the coupling of the reggeon to the proton. We assume that

$$B_R(t) = B_R(0)\ \exp(t/2\Lambda_R^2) \qquad (2.15)$$

with $\Lambda_R = 0.65\,\text{GeV}$, as known from the reggeon phenomenology of hadronic reactions. Moreover, the following relations between the reggeon-proton couplings are found

$$B_{f_2}^2(0) > B_\omega^2(0) \gg B_{a_2}^2(0) \sim B_\rho^2(0)\,. \qquad (2.16)$$

This result shows that the isovector reggeons (a_2, ρ) can safely be neglected in the presented analysis. The function $F_2^R(\beta, Q^2)$ is a reggeon structure function and is given by [68]

$$F_R(\beta) \;=\; A_R\, \beta^{-0.08}\, (1-\beta)^2\,, \tag{2.17}$$

where A_R is determined by the triple Regge vertex $I\!R I\!R I\!P$ (see Fig. 2.2). With the diffractive structure function (2.11), the Regge factorization is obviously broken for large values of the variable $x_{I\!P}$.

2.4 DGLAP based analysis of DPD

In the QCD approach based on collinear factorization, the diffractive structure functions ind DIS, Eqs. (1.12) and (1.13), are decomposed into the leading and higher twist contributions

$$F_{2,L}^D(x, Q^2, x_{I\!P}, t) \;=\; F_{2,L}^{D(tw2)} \;+\; F_{2,L}^{D(tw4)} \;+\; \ldots\,. \tag{2.18}$$

2.4.1 Twist–2 contribution

The twist–2 part is given in terms of the diffractive parton distributions through the standard collinear factorization formula [54, 62, 64, 69]. In the next-to-leading logarithmic approximation

$$F_2^{D(tw2)}(x, Q^2, x_{I\!P}, t) \;=\; S_D + \frac{\alpha_s}{2\pi}\left\{C_2^S \otimes S^D + C_2^G \otimes G^D\right\} \tag{2.19}$$

$$F_L^{D(tw2)}(x, Q^2, x_{I\!P}, t) \;=\; \frac{\alpha_s}{2\pi}\left\{C_L^S \otimes S^D + C_L^G \otimes G^D\right\} \tag{2.20}$$

where α_s is the strong coupling constant and $C_{2,L}^{S,G}$ are coefficients functions known from inclusive DIS [70, 71]. The integral convolution is performed for the longitudinal momentum fraction, *e.g.*

$$(C \otimes F)(\beta) = \int_\beta^1 dz\, C\,(\beta/z)\, F(z)\,. \tag{2.21}$$

Notice that in the leading order, when terms proportional to α_s are neglected, the longitudinal structure function $F_L^{D(tw2)} = 0$.

After introducing a new notation, which we will be using from now on,

$$q_f^D \equiv \mathcal{F}_{q/p}^D \quad \overline{q}_f^D \equiv \mathcal{F}_{q/p}^D \quad g_f^D \equiv \mathcal{F}_{q/p}^D \tag{2.22}$$

for the quark, antiquark and gluon diffractive parton distributions, respectively, the functions S_D and G_D are given by

$$S^D(\beta, Q^2, x_{I\!P}, t) \;=\; \sum_{f=1}^{N_f} e_f^2\, \beta\left\{q_f^D(\beta, Q^2, x_{I\!P}, t) + \overline{q}_f^D(\beta, Q^2, x_{I\!P}, t)\right\} \tag{2.23}$$

$$G^D(\beta, Q^2, x_{I\!P}, t) \;=\; \beta g^D(\beta, Q^2, x_{I\!P}, t) \tag{2.24}$$

Note that $\beta = x/x_{I\!P}$ plays the role of the Bjorken variable in DDIS. In the infinite momentum frame, the DPD have an interpretation of conditional probabilities to find a parton in the proton with the momentum fraction $x = \beta x_{I\!P}$ under the condition that the incoming proton stays intact losing a small fraction $x_{I\!P}$ of its momentum. A formal definition of the diffractive parton distributions based on the quark and gluon twist-2 operators is given in [54, 56].

The DPD are evolved in $\log(Q^2)$ by the DGLAP evolution equations [72] for which the variables $(x_{I\!P}, t)$ are external parameters. In this analysis we assume *Regge factorization* for these variables:

$$\begin{aligned} q_f^D(\beta, Q^2, x_{I\!P}, t) &= f_{I\!P}(x_{I\!P}, t)\; q_{f/I\!P}(\beta, Q^2) \\ g^D(\beta, Q^2, x_{I\!P}, t) &= f_{I\!P}(x_{I\!P}, t)\; g^{I\!P}(\beta, Q^2)\,. \end{aligned} \tag{2.25}$$

where $q_{f/I\!P}$ and $g^{I\!P}$ are already introduced pomeron parton distributions. The function $f_{I\!P}(x_{I\!P}, t)$ is the pomeron flux (2.8) with the pomeron trajectory

$$\alpha_{I\!P}(t) = \alpha_{I\!P}(0) + \alpha'_{I\!P} \cdot t\,. \tag{2.26}$$

in which $\alpha'_{I\!P} = 0.06\ \mathrm{G}eV^{-2}$ and the pomeron intercept $\alpha_{I\!P}(0)$ is fitted to the data. The pomeron quark distributions are flavor independent and are given by a singlet quark distribution $\Sigma^{I\!P}(\beta, Q^2)$:

$$q_{f/I\!P}(\beta, Q^2) \;=\; \overline{q}_{f/I\!P}(\beta, Q^2) \;\equiv\; \frac{1}{2N_f}\,\Sigma^{I\!P}(\beta, Q^2) \tag{2.27}$$

where N_f is a number of active flavors.

The problem of Regge factorization is an issue which should be tested experimentally. The pomeron in this context is a model of diffractive interactions which provides energy dependence through the $x_{I\!P}$ dependence of the pomeron flux. Its normalization is only a useful convention because the normalization of the pomeron distributions $q_{f/I\!P}$ and $g^{I\!P}$ in Eqs. (2.25) (at some scale Q_0^2) is fitted to data.

2.4.2 Twist-2 charm contribution

We describe the charm quark diffractive production using twist-2 formula for the $c\overline{c}$ pair generation from a gluon. These are formula analogous to the inclusive case [73] in which the diffractive gluon distribution g^D is substituted:

$$F_{2,L}^{D(c\overline{c})}(x, Q^2, x_{I\!P}, t) \;=\; 2\beta\, e_c^2\, \frac{\alpha_s(\mu_c^2)}{2\pi} \int_{a\beta}^1 \frac{dz}{z}\, C_{2,L}\big(\beta/z, m_c^2\, Q^2\big)\, g^D(z, \mu_c^2, x_{I\!P}, t) \tag{2.28}$$

where $a = 1 + 4m_c^2/Q^2$, the factorization scale $\mu_c^2 = 4m_c^2$ and the charm mass $m_c = 1.4\ \mathrm{G}eV$. The coefficient functions read

$$\begin{aligned} C_2(z, r) \;=\; & \tfrac{1}{2}\left\{z^2 + (1-z)^2 + 4z(1-3z)r - 8z^2r^2\right\} \ln\tfrac{1+\alpha}{1-\alpha} \\ & + \tfrac{1}{2}\alpha\left\{-1 + 8z(1-z) - 4z(1-z)r\right\} \end{aligned} \tag{2.29}$$

$$C_L(z, r) \;=\; -4z^2 r \ln\frac{1+\alpha}{1-\alpha} + 2\alpha z(1-z) \tag{2.30}$$

with $\alpha = \sqrt{1 - 4rz/(1-z)}$. The $c\overline{c}$ pair can be produced if invariant mass of the diffractive system fulfills the condition

$$M^2 = Q^2\left(\frac{1}{\beta} - 1\right) > \; 4m_c^2\,. \tag{2.31}$$

2.4.3 Twist–4 contribution

In the presented description, the leading twist structure function vanishes when $\beta \to 1$, *i.e.* for small diffractive masses, $M^2 \ll Q^2$. However, as it has already been mentioned in Section 1, it was found in the dipole approach that for $\beta \to 1$ the twist–4 contribution dominates over the vanishing twist–2

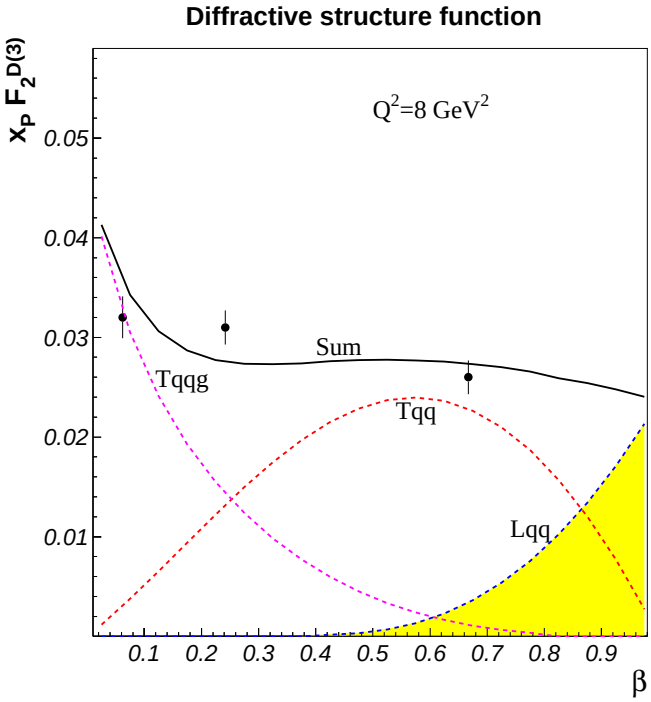

Figure 2.3: Three contributions to F_2^D from: $q\overline{q}$ and $q\overline{q}g$ from transverse (T) and longitudinal (L) photons [24] for $x_{I\!P} = 0.003$. The twist–4 contribution $Lq\bar{q}$ is indicated by the yellow band. Old ZEUS data points are shown.

one [24, 27, 74]. Thus it has to be considered in any analysis with the diffractive parton distributions. The explicit form of the twist–4 contribution is given by

$$F_L^{q\bar{q}} = \frac{3}{16\pi^4 x_{I\!P}} \mathrm{e}^{-B_D|t|} \sum_f e_f^2 \frac{\beta^3}{(1-\beta)^4} \int_0^{\frac{Q^2(1-\beta)}{4\beta}} dk^2 \frac{k^2/Q^2}{\sqrt{1-\frac{4\beta}{1-\beta}\frac{k^2}{Q^2}}} \phi_0^2(k, x_{I\!P}) \qquad (2.32)$$

where

$$\phi_0(k, x_{I\!P}) \;=\; k^2 \int_0^\infty dr\, r\, K_0\left(\sqrt{\frac{\beta}{1-\beta}} kr\right) J_0(kr)\, \hat{\sigma}(x_{I\!P}, r) \qquad (2.33)$$

and K_0 and J_0 are Bessel functions [60]. Strictly speaking, Eq. (2.32) contains all inverse powers of Q^2 but the part proportional to $1/Q^2$ (called twist–4) dominates. The function $\hat{\sigma}(x_{I\!P}, r)$ in Eq. (2.33) is called the dipole-proton cross section and describes the interaction of the $q\overline{q}$ and $q\overline{q}g$ dipoles with the proton. Following [25] we choose

$$\hat{\sigma}(x_{I\!P}, r) \;=\; \sigma_0 \left\{1 - \exp\left(-r^2 Q_s^2(x_{I\!P})/4\right)\right\} \qquad (2.34)$$

where $Q_s^2(x_{I\!P}) = (x_{I\!P}/x_0)^{-\lambda}$ GeV^2 is a saturation scale which provides the energy dependence of the twist–4 contribution. The parameters $\sigma_0 = 29$ mb, $x_0 = 4 \cdot 10^{-5}$ and $\lambda = 0.28$ are taken from [25] (Fit 2 with charm). This form of the dipole cross section provides successful description of the first HERA data on both inclusive and diffractive structure functions [24, 25]. We checked that

a very similar description of $F_L^{q\bar{q}}$ was found in a recent analysis [75] based on the recent color glass condensate parametrization of the dipole scattering amplitude [76].

From more theoretical point of view the saturated form of the dipole cross section unitarizes the BFKL pomeron, and gives a prediction for the $x_{I\!P}$ (energy) dependence of the DDIS. This aspect of the presented description is subjected to the modelling, however, the β (diffractive mass) dependence is a genuine prediction of perturbative QCD calculations. It appears that the leading in Q^2 components, $q\overline{q}$ and $q\overline{q}g$ from transverse photons, vanish at $\beta = 1$. This is not the case for the $q\overline{q}$ production from longitudinal photons which is formally suppressed by $1/Q^2$. Thus, the particular β-dependence makes the $F_L^{q\bar{q}}$ contribution dominant for $\beta \to 1$ see Fig. 2.3. More details on the dipole approach to DDIS will be presented in Section 3. It is also important to realize that the expected $x_{I\!P}$-dependence for of the twist–4 contribution is given by

$$F_L^{q\bar{q}} \sim \frac{Q_s^4(x_{I\!P})}{x_{I\!P}} \sim x_{I\!P}^{-1-2\lambda}, \tag{2.35}$$

which clearly violates the universality of the effective pomeron intercept, assumed in the Ingelman-Schlein model.

2.4.4 Reggeon contribution

The diffractive data from H1 Collaboration for higher values of $x_{I\!P}$ hints towards a contribution which decreases with energy. This effect can be described by reggeon exchanges in addition to the rising with energy pomeron exchange. Following [67, 68], we consider the dominant isoscalar (f_2, ω) reggeon exchanges which lead to the following contribution to F_2^D:

$$F_2^{D(R)}(x, Q^2, x_{I\!P}, t) = \sum_R f_R(x_{I\!P}, t)\, F_R(\beta, Q^2)\,. \tag{2.36}$$

This contribution breaks Regge factorization of the diffractive structure function, however, its presence is necessary for $x_{I\!P} > 0.01$ [7,8,77,78]. The reggeon flux f_R is given formula (2.13) with the reggeon trajectory (2.12. From the Regge phenomenology of hadronic reactions the couplings of the reggeon to the proton are given by [68]:

$$B_{f_2}^2(0) = 194\,\mathrm{GeV}^{-2}, \qquad B_\omega^2(0) = 52\,\mathrm{GeV}^{-2}. \tag{2.37}$$

The reggeon structure function $F_R(\beta, Q^2)$ is given by [68]

$$F_R(\beta) = A_R\, \beta^{-0.08}\, (1-\beta)^2\,, \tag{2.38}$$

where the normalization A_R is a fitted parameter. Thus, in the first approximation, we neglect the Q^2 dependence of the reggeon contribution.

2.5 Fit details

2.5.1 Data sets

In our analysis we use diffractive data from the H1 [7,77] and ZEUS [8,78] Collaborations. In Table 2.1 we show their kinematic limits in which they have been measured. The minimal value value of $|t|$ is given by

$$|t_{min}| \simeq \frac{x_{I\!P}^2}{1 - x_{I\!P}}\, m_p^2\,, \tag{2.39}$$

Collab.	No. points	Data	$\|t\|$-range	Q^2-range	β-range
H1 [77]	72	LP	$[0.08,\ 0.5]$	$[2\,,50]$	$[0.02\,,0.7]$
ZEUS [78]	80	LP	$[0.075\,,0.35]$	$[2\,,100]$	$[0.007\,,0.48]$
H1 [7]	461	$M_Y < 1.6$	$[\|t_{min}\|\,,1]$	$[3.5\,,1600]$	$[0.01\,,0.9]$
ZEUS [8]	198	$M_Y < 2.3$	$[\|t_{min}\|\,,\infty]$	$[2.2\,,80]$	$[0.003\,,0.975]$

Table 2.1: Kinematic regions of diffractive data from HERA. LP means leading proton data and M_Y is invariant mass of a dissociated proton. Dimensionfull quantities are in units of 1 GeV.

where m_p is the proton mass. The leading proton data from H1, measured in the range given in Table 2.1, were corrected by the H1 Collaboration to the range $|t_{min}| < |t| < 1$ GeV^2.

The ZEUS data are given for the diffractive structure function F_2^D, thus we use

$$F_2^D \;=\; F_2^{D(tw2)} + F_2^{D(R)} + F_{Lq\bar{q}}^D \tag{2.40}$$

$$F_L^D \;=\; F_L^{D(tw2)} + F_{Lq\bar{q}}^D\,. \tag{2.41}$$

The longitudinal twist-4 contribution is present on the r.h.s. of Eq. (2.40) since F_2^D is the sum of the contributions from the transverse and longitudinal polarized virtual photon. The H1 data are presented for the reduced cross section

$$\sigma_r^D \;=\; F_2^D - \frac{y^2}{1+(1-y)^2} F_L^D\,. \tag{2.42}$$

Thus we substitute relations (2.40) and (2.41) in there and use

$$\sigma_r^D \;=\; \left\{ F_2^{D(tw2)} + F_2^{D(R)} - \frac{y^2}{1+(1-y)^2} F_L^{D(tw2)} \right\} \;+\; \frac{2(1-y)}{1+(1-y)^2}\, F_{Lq\bar{q}}^D\,. \tag{2.43}$$

The expression in the curly brackets is the twist–2 contribution while the last term is the twist–4 one. Notice that the difference between F_2^D and σ_r^D is most important for $y \to 1$.

2.5.2 Fit parameters

We fit the diffractive parton distributions at the initial scale $Q_0^2 = 1.5$ GeV^2 assuming the Regge factorized form (2.25) with the following pomeron parton distributions [7]:

$$\beta\,\Sigma^{I\!P}(\beta) \;=\; A_q\,\beta^{B_q}\,(1-\beta)^{C_q} \tag{2.44}$$

$$\beta\,g^{I\!P}(\beta) \;=\; A_g\,\beta^{B_g}\,(1-\beta)^{C_g}\,. \tag{2.45}$$

where the six indicated parameters are fitted to data. We additionally multiplied both distributions by a factor $\exp\{-a/(1-\beta)\}$ with $a = 0.01$ to secure that their vanishing for $\beta = 1$. This factor is only important in the case when C_q or C_g becomes negative in the performed fits. We use the next-to-leading order DGLAP evolution equations with $\Lambda_{QCD} = 407$ MeV for $N_f = 3$ flavors [79].

The pomeron flux in Eq. (2.25) is integrated over t in the limits given in Table 2.1, which leads to the form

$$f_{I\!P}(x_{I\!P}) \;=\; \frac{B_{I\!P}^2(0)}{8\pi^2 B} \left\{ \mathrm{e}^{-B|t_{min}|} - \mathrm{e}^{-B|t_{max}|} \right\} x_{I\!P}^{\,1-2\alpha_{I\!P}(0)}\,. \tag{2.46}$$

The shrinkage parameter in the above is given by

$$B = B_D + 2\alpha'_{I\!P} \ln(1/x_{I\!P}) \tag{2.47}$$

No	Data	Fit	$\alpha_{I\!P}(0)$	A_R	A_q	B_q	C_q	A_g	B_g	C_g	χ^2/N
1	H1 (LP)	tw-2	1.098	0.29	1.75	1.49	0.5^*	2.09	0.67	0.80	0.48
2	ZEUS (LP)	tw-2	1.145	1.05	2.13	1.51	0.5^*	10.0*	1.03	2.26	0.40
3	H1	tw-2	1.117	0.49	1.33	1.63	0.34	0.17	-0.16	-1.10	1.04
4		tw-(2+4)	1.119	0.48	1.62	1.98	0.59	0.04	-0.56	-1.68	1.17
5	ZEUS	tw-2	1.093	0.0^*	1.68	1.01	0.5^*	0.49	-0.03	-0.40	1.35
6		tw-(2+4)	1.092	0.0^*	1.20	0.85	0.57	0.07	-0.52	-1.48	1.82

Table 2.2: Fit parameters from fits to H1 and ZEUS data with and without twist–4 contribution, marked by tw-(2+4) and tw-2, respectively. Parameters with an asterisk are kept constant in a fit and $N = N_{exp} - N_{param}$.

with $B_D = 5.5\,\mathrm{GeV}^{-2}$ and $\alpha'_{I\!P} = 0.06\,\mathrm{GeV}^{-2}$ [77].

In summary, we have eight fit parameters altogether: the pomeron intercept $\alpha_{I\!P}(0)$ in the Regge trajectory (2.26), the reggeon normalization A_R in Eq. (2.38) and the six parameters in Eqs. (2.44) and (2.45)

2.6 Fit results

The data sets from Table 2.1 were obtained in different kinematical regions, using different methods of their analysis. Thus we decided to perform fits to each data set separately. The fit parameter values are shown in Table 2.2. The difference between them can be attributed to the scale of uncertainty of our analysis. In each case we preformed two fits: with and without the twist–4 formula added to the twist–2 contribution. The common normalization of the pomeron flux enables us to compare the diffractive parton distributions obtained from fits to different data sets.

2.6.1 Leading proton data (LP)

We started from fits to the leading proton data. The fit parameters in this case are shown in the first two rows of Table 2.2. We only show the twist–2 fit results since they do not change in fits with the twist–4 term. This is because the leading proton data comes from the region of β values, $\beta \leq 0.7$ (H1) and $\beta < 0.5$ (ZEUS), where the twist–4 contribution is small, see Fig. 2.3. In Fig. 2.4 we show good fit quality of the fits for ZEUS (LP) data from the second rows of Table 2.2. The main difference between the parameters from the fits to the LP data and the fits to data with a dissociated proton (DP) (presented in the next four rows of Table 2.2) lies in the value of the parameter C_g which controls the gluon distribution at large β. For the LP data $C_g > 0$ and the gluon distribution is suppressed near $\beta \approx 1$, while for the DP data $C_g < 0$ and the gluon distribution is strongly enhanced there. This shows that the region of $\beta > 0.7$ is crucial and without it we lose important part of information about diffractive interactions. Thus, from now on we concentrate on the DP data analysis.

2.6.2 H1 data

The parameters from fits to the H1 data with dissociate proton (DP) are given in the third and fourth rows (fits No. 3 and 4 in Table 2.2). The fit quality is practically the same for these fits, independent of the twist–4 contribution. The presence of the reggeon term improves fit quality by 30 units of χ^2 for 461 experimental points. A good quality of the fits is illustrated in Fig. 2.5 and in Fig. 2.6, which also

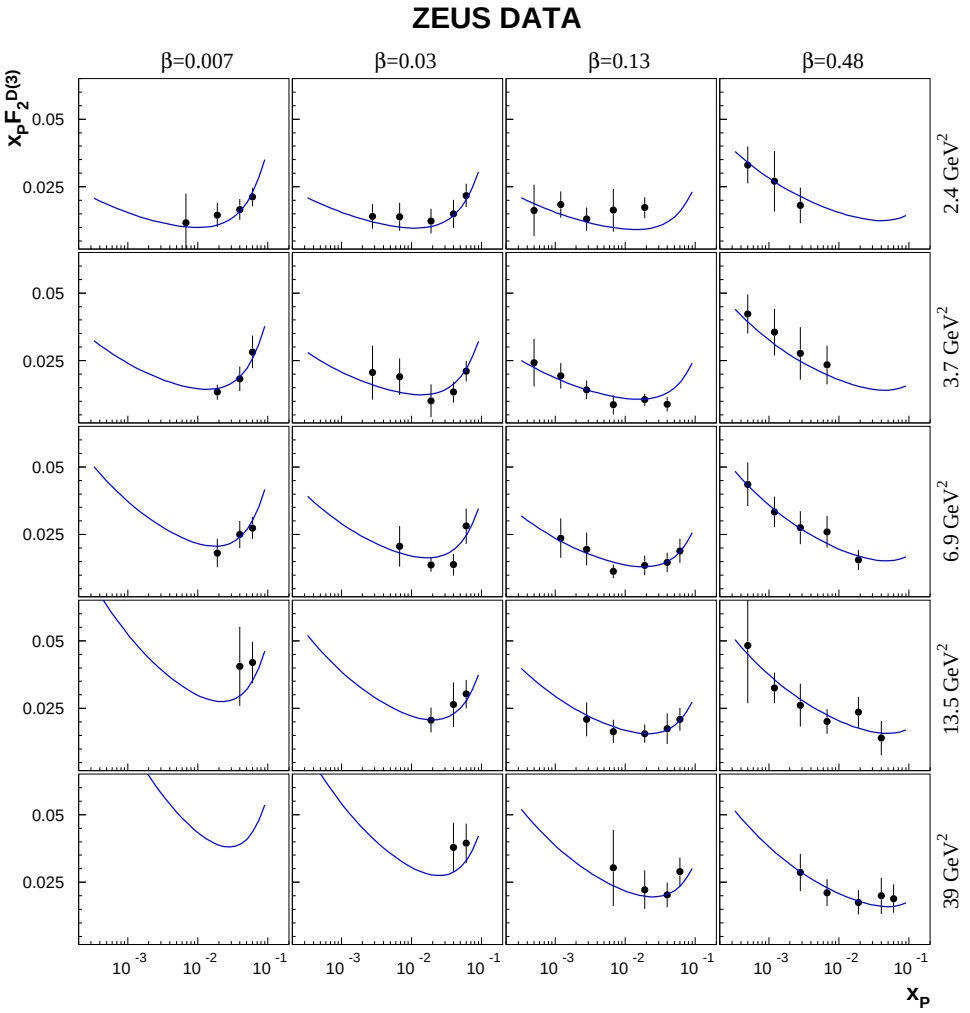

Figure 2.4: Diffractive structure function F_2^D for ZEUS data (leading proton) as a function of $x_{I\!P}$. Solid lines: twist–2 fit.

shows that the reduced cross sections (2.43) from the twist–2 (solid lines) and twist–(2+4) fits (dashed lines) are very close to each other.

In Fig. 2.7 we show our results for the largest measured value of $\beta = 0.9$. The twist–4 contribution, shown as the dotted lines, is already very important in this region. We see that taking into account experimental errors, both twist–2 (solid) and twist–(2+4) (dashed) fit curves describe data reasonable well. The twist-(2+4) curves, however, have a steeper dependence on $x_{I\!P}$ (energy) than in the pure twist–2 analysis. This observation is by far more pronounced in the analysis of the ZEUS data performed for the F_2^D structure function.

The diffractive parton distributions from our fits are shown in Fig. 2.8 in terms of the pomeron parton distributions $\beta\Sigma_{I\!P}(\beta, Q^2)$ and $\beta g_{I\!P}(\beta, Q^2)$. Being independent of the pomeron flux, such a presentation allows for a direct comparison of the results from fits to different data sets. We see that the singlet quark distributions are quite similar while the gluon distributions are different. In the twist–(2+4) fit the gluon distribution is peaked stronger near $\beta \approx 1$. This somewhat surprising result can be understood by looking at the logarithmic slope of F_2^D for fixed values of β. From the LO DGLAP

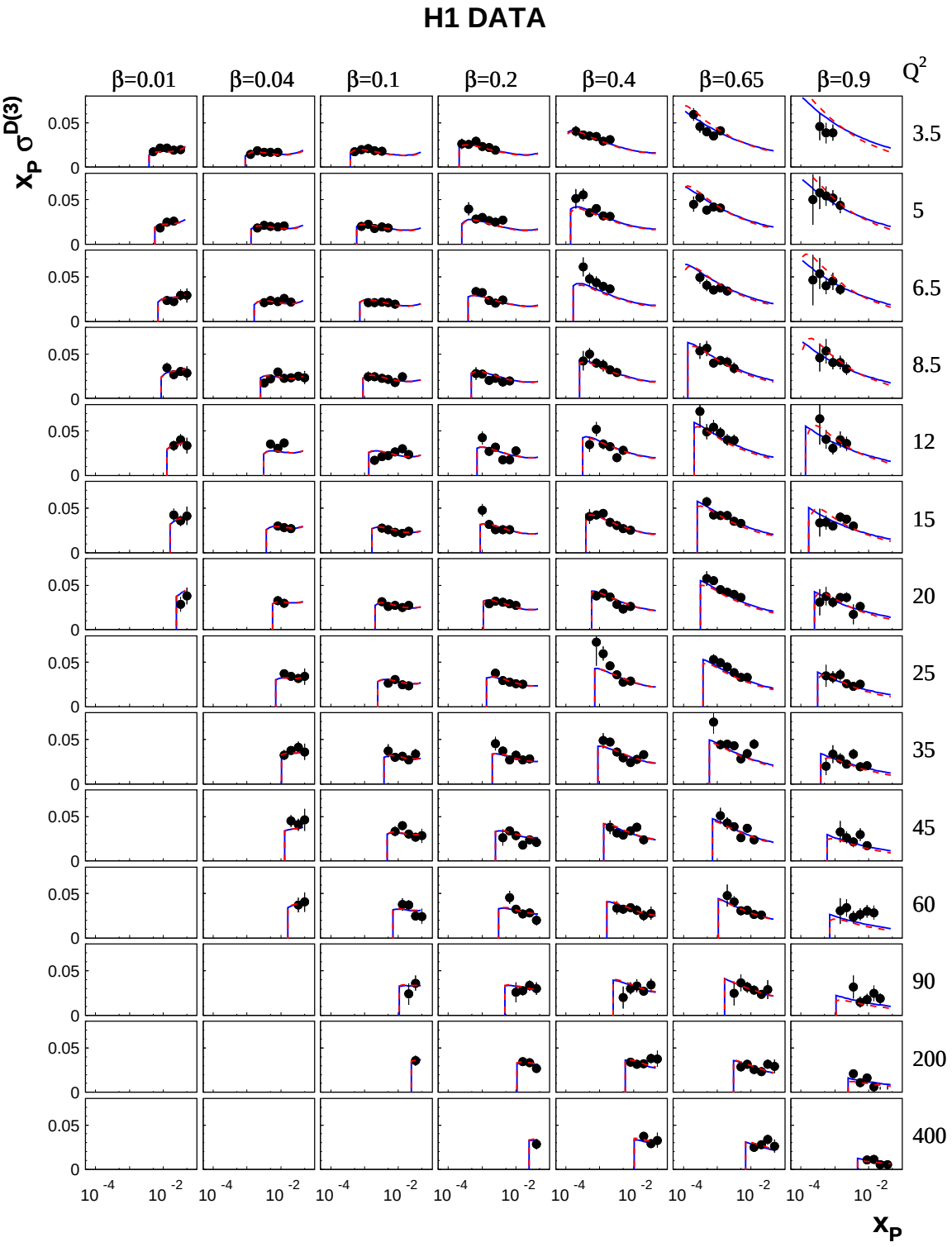

Figure 2.5: Reduced cross section $\sigma_r^{D(3)}$ for H1 data as a function of $x_{I\!P}$. Solid lines: twist–2 fit, dashed lines: twist–(2+4) fit.

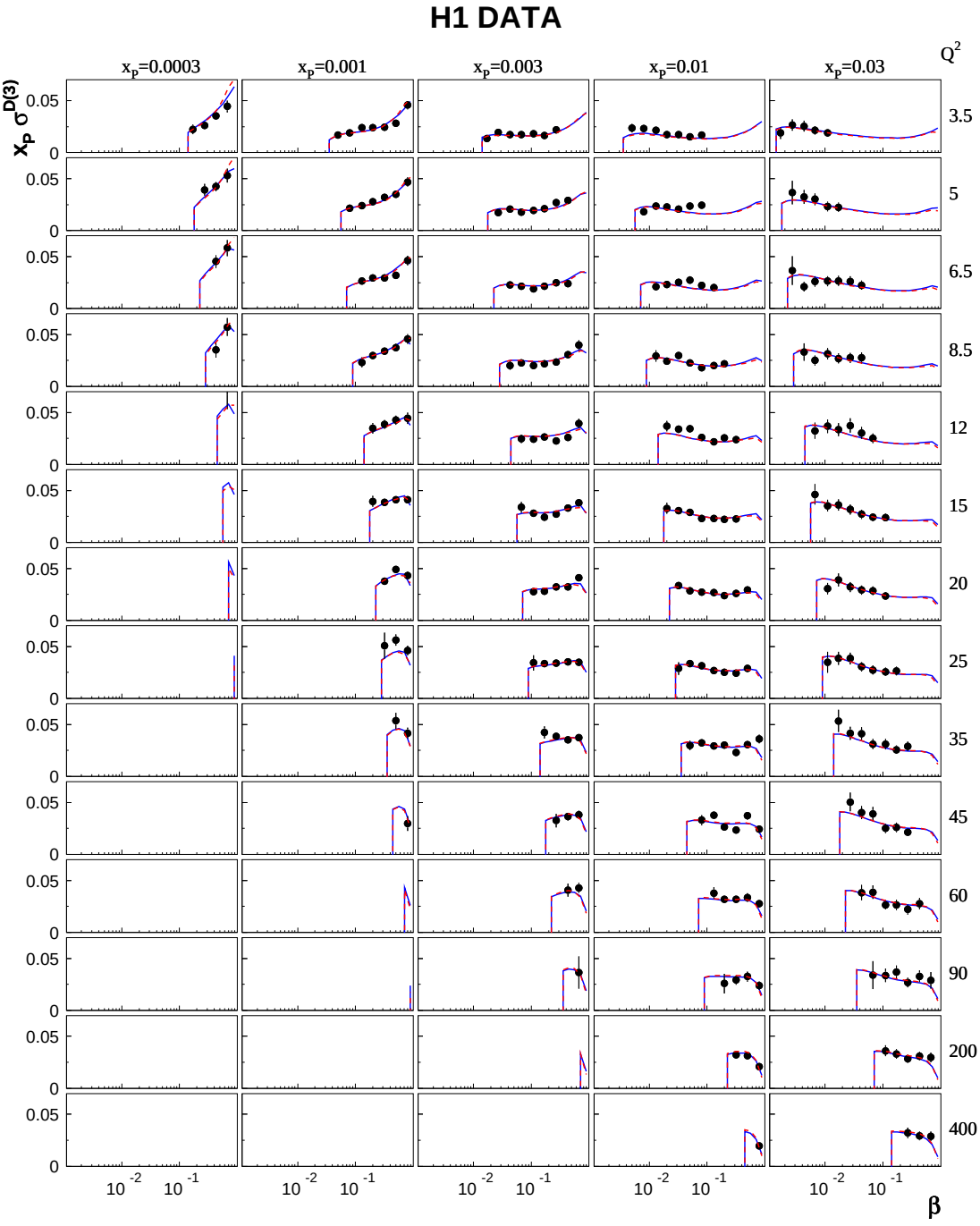

Figure 2.6: Reduced cross section $\sigma_r^{D(3)}$ for H1 data as a function of β. Solid lines: twist–2 fit, dashed lines: twist–(2+4) fit.

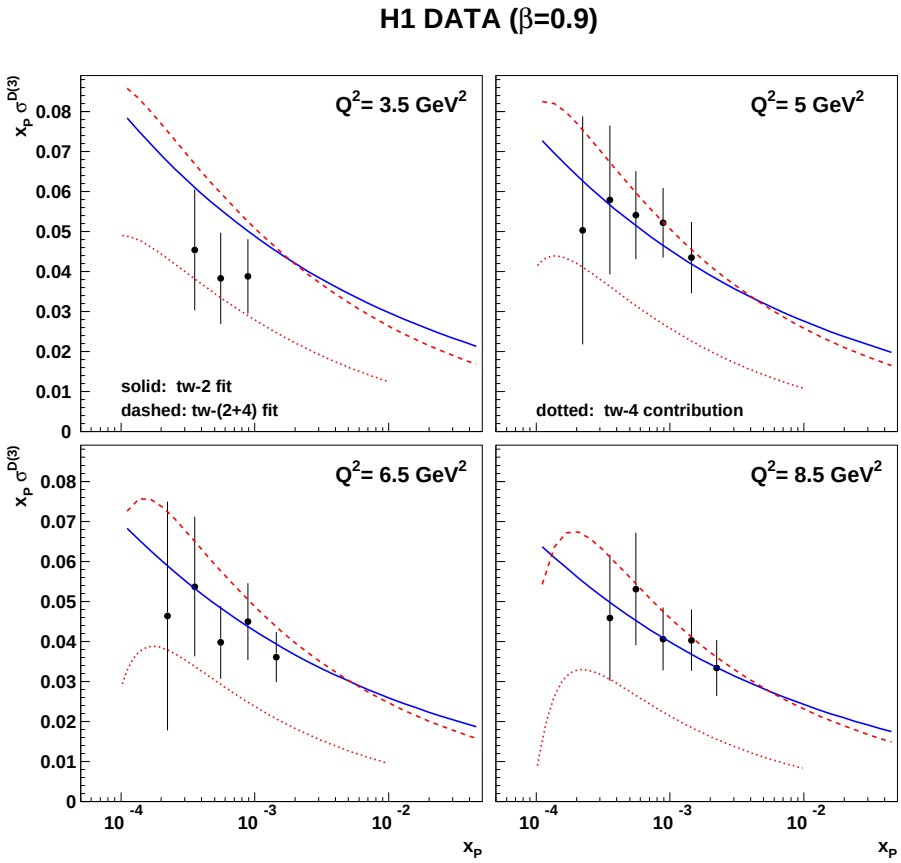

Figure 2.7: Reduced cross section $\sigma_r^{D(3)}$ for H1 data at $\beta = 0.9$ for four values of Q^2 against fit curves.

equations we have:

$$\frac{\partial F_2^D}{\partial \ln Q^2} \sim \frac{\partial \Sigma_{I\!P}}{\partial \ln Q^2} = P_{qq} \otimes \Sigma_{I\!P} + P_{qG} \otimes G_{I\!P} - \Sigma_{I\!P} \int P_{qq} \tag{2.48}$$

where the negative term sums virtual corrections. For large β, the measured slope is negative which means that the virtual emission term must dominate over the real emission ones. The addition of the twist–4 contribution to F_2^D, proportional to $1/Q^2$, contributes a negative value to the slope which has to be compensated by a larger gluon distribution in the region $\beta \approx 1$ in order to describe the same data.

In Fig. 2.9 we present our most important result from the presented analysis. On the left panel the F_2^D structure functions are shown from the twist–2 and twist–(2+4) fits without significant difference between. The twist–4 contribution is marked by the dotted lines. However, the longitudinal structure functions F_L^D from the two fits (right panel) are very different due to the $q\overline{q}$ production from longitudinal photons. Let us emphasize that both sets of curves were found in the fits which well describe the existing data, including the large β region. Thus, an independent *measurement* of F_L^D in this region would be an important test of the QCD mechanism of diffraction.

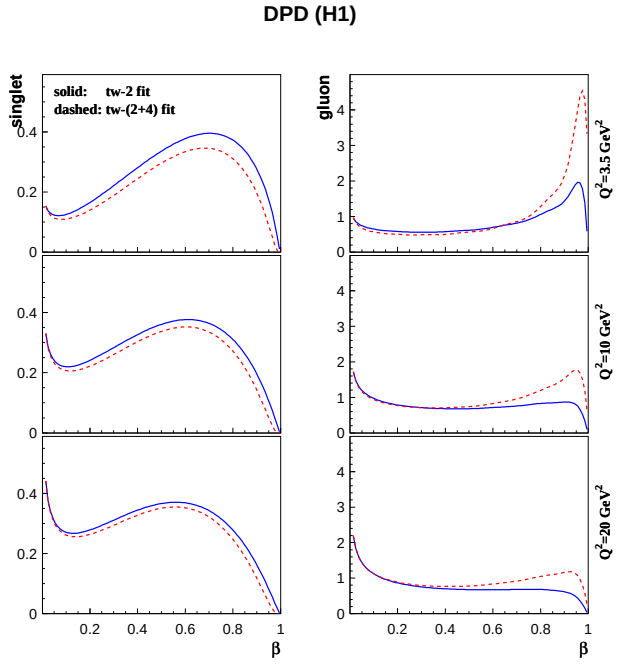

Figure 2.8: Pomeron parton distributions: singlet $\beta\Sigma_{I\!P}(\beta, Q^2)$ (left) and gluon $\beta g_{I\!P}(\beta, Q^2)$ (right) from H1 data.

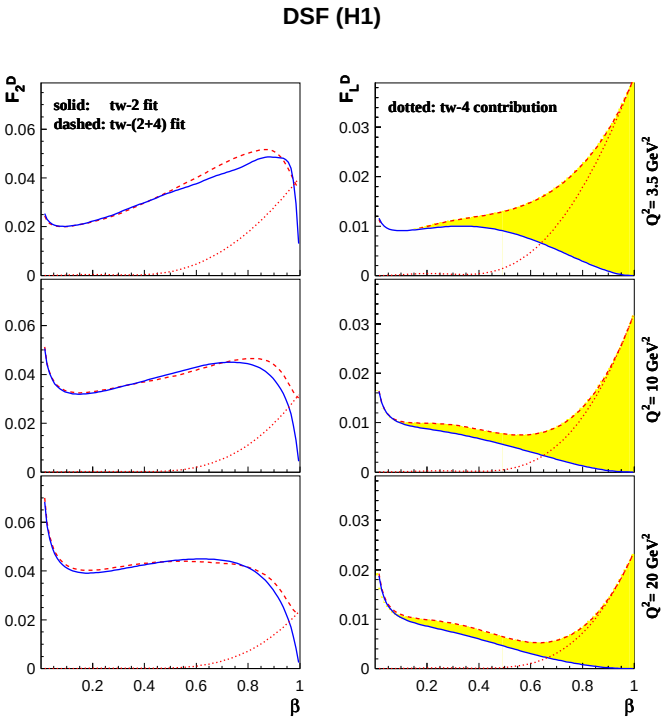

Figure 2.9: Diffractive structure functions $F_2^{D(3)}$ (left) and $F_L^{D(3)}$ (right) from fits to H1 data for $x_{I\!P} = 10^{-3}$. The band shows the effect of twist–4 on the predictions for $F_L^{D(3)}$.

2.7 Comparison with H1 DPD

We finish this section by showing the comparison of our diffractive parton distributions with those obtained by the H1 Collaboration [7], see Fig. 2.10. The latter analysis used data points with $Q^2 > 8.5\ \mathrm{GeV}^2$, and this is why they stop showing values of DPDF for $\beta > 0.8$. We have not imposed such a restriction in our analysis, analyzing the high β region. In general, we see good overall agreement between the shown sets of DPDF in the common region of β with additional details provided by our analysis. In the Figure below variable z is equal β.

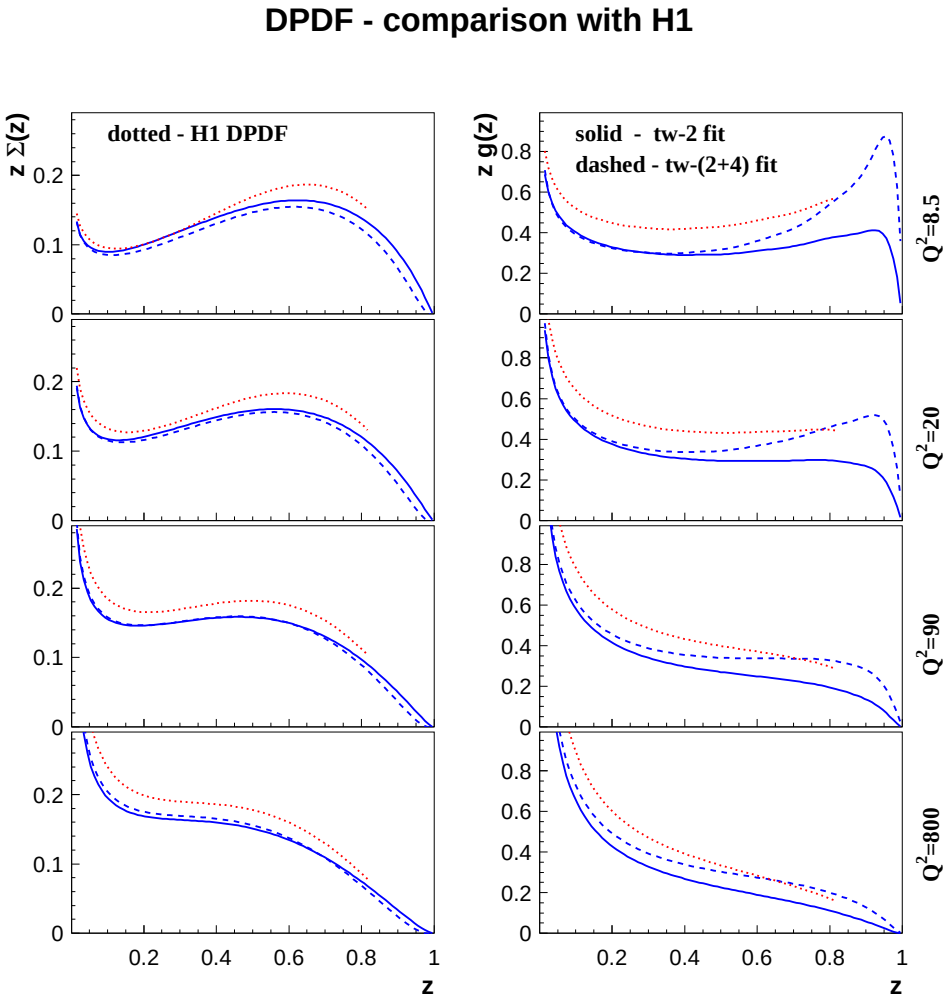

Figure 2.10: Diffractive parton distributions at $x_{I\!P} = 0.003$ for singlet (left) and gluon (right) DPD from twist-2 and twist-(2+4) fits together with the DPDF from H1 fits (FIT A). Q^2 is in units GeV^2.

2.7.1 ZEUS data

The same fits were performed for the ZEUS data (fits No. 5 and 6 in Table 2.2). This time the Regge term (2.17) is not necessary since the fits give the reggeon normalization $A_R \approx 0$. In general, the fit quality is worse than for the H1 data for both types of fits.

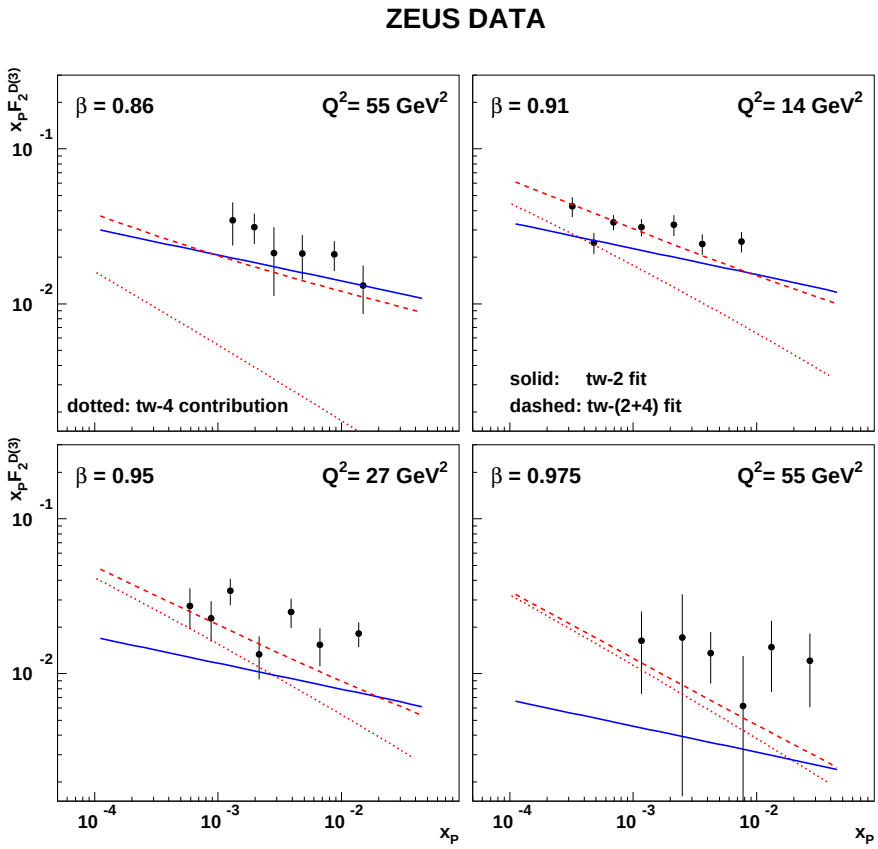

Figure 2.11: Diffractive structure function $F_2^{D(3)}$ as a function $x_{I\!P}$ for ZEUS data at large values of β against fit curves.

As shown in Figs. 2.12, 2.13 and 2.14 the biggest difference between the twist–2 and twist–(2+4) results occurs at large β values. This is shown in detail in Fig. 2.11. We see that the presence of the twist–4 term in the fit (dashed lines) improves the agreement with the data in this region. In particular, a steep dependence of F_2^D on $x_{I\!P}$ is better reproduced by the twist–(2+4) fit then by the twist–2 one (solid lines). This dependence is to large extend driven by the twist–4 contribution (dotted lines).

The behavior of the diffractive parton distributions and structure functions, shown in Figs. 2.15 and 2.16 respectively, is very similar to that found for the H1 data. The gluon distribution from the twist–(2+4) fit is strongly peaked near $\beta \approx 1$ and the longitudinal structure functions is dominated by the twist–4 contribution in the large β region.

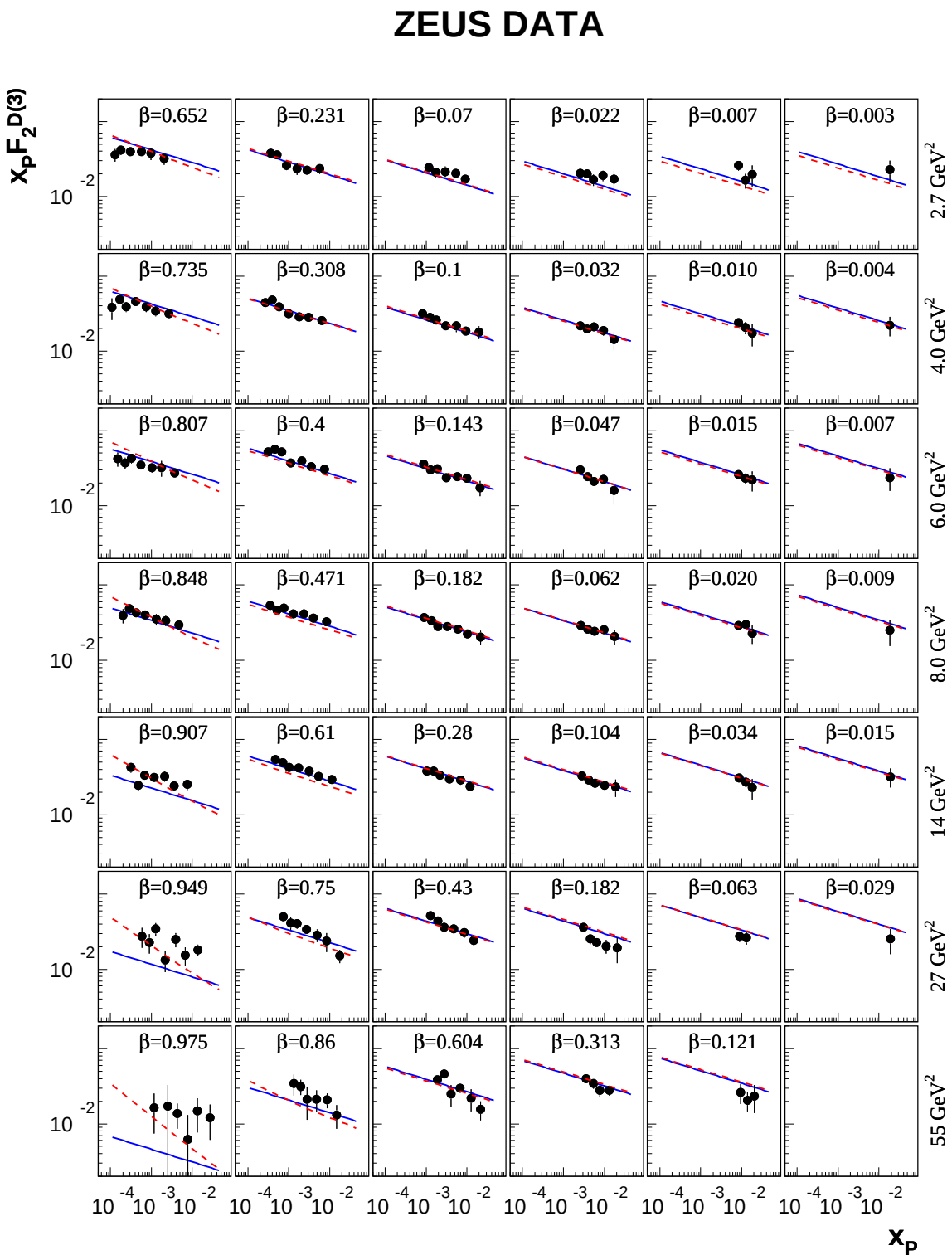

Figure 2.12: Diffractive structure function $F_2^{D(3)}$ as a function $x_{I\!P}$ for ZEUS data. Solid lines: twist–2 fit, dashed lines: twist–(2+4) fit.

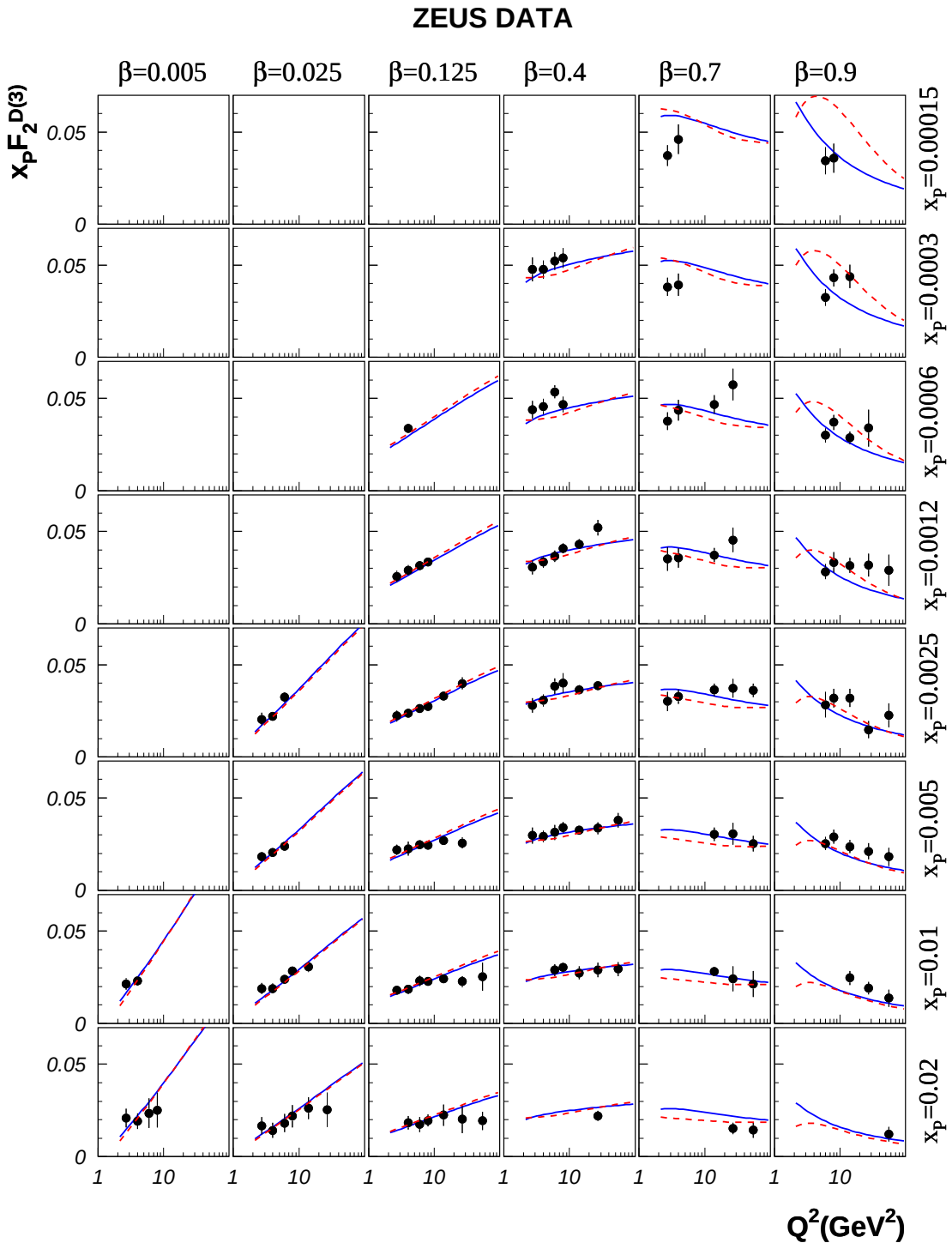

Figure 2.13: Diffractive structure function $F_2^{D(3)}$ as a function Q^2 for ZEUS data. Solid lines: twist–2 fit, dashed lines: twist–(2+4) fit.

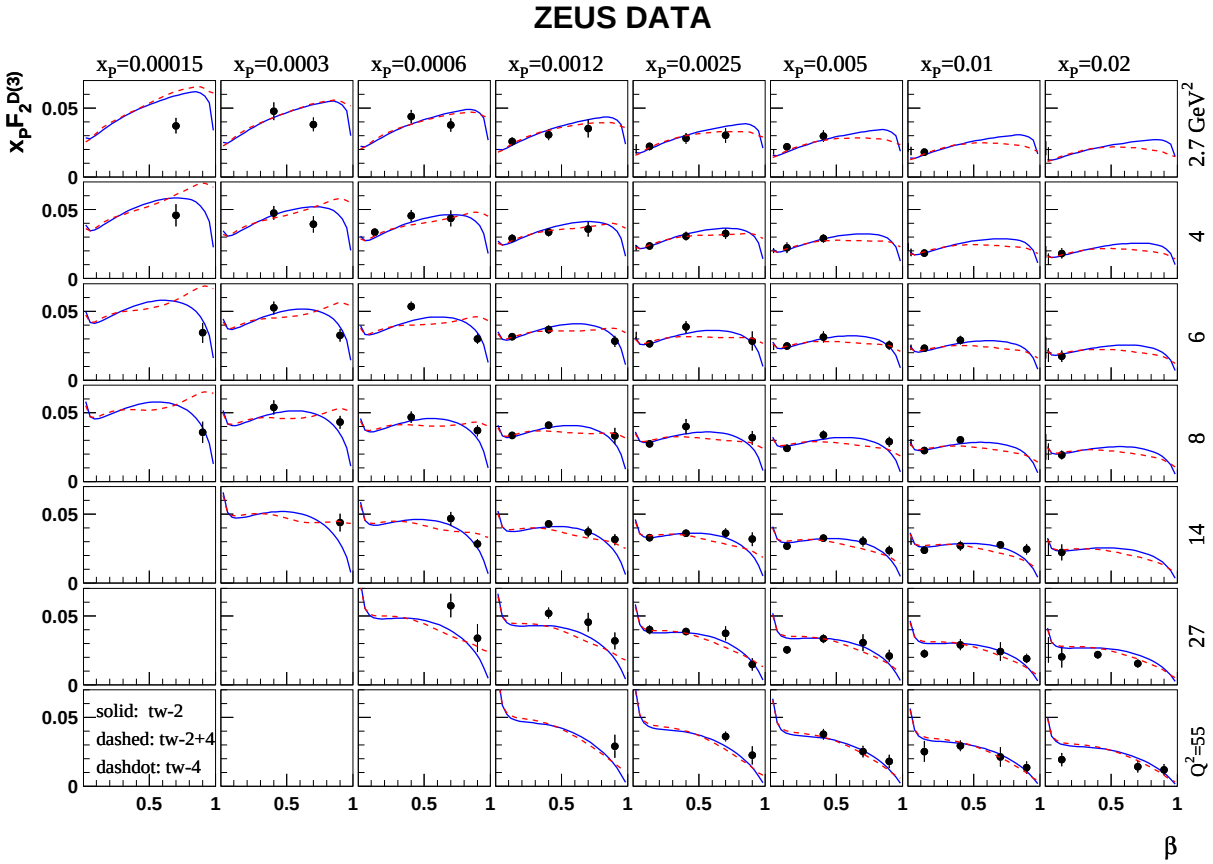

Figure 2.14: Diffractive structure function $F_2^{D(3)}$ as a function β for ZEUS data. Solid lines: twist–2 fit, dashed lines: twist–(2+4) fit.

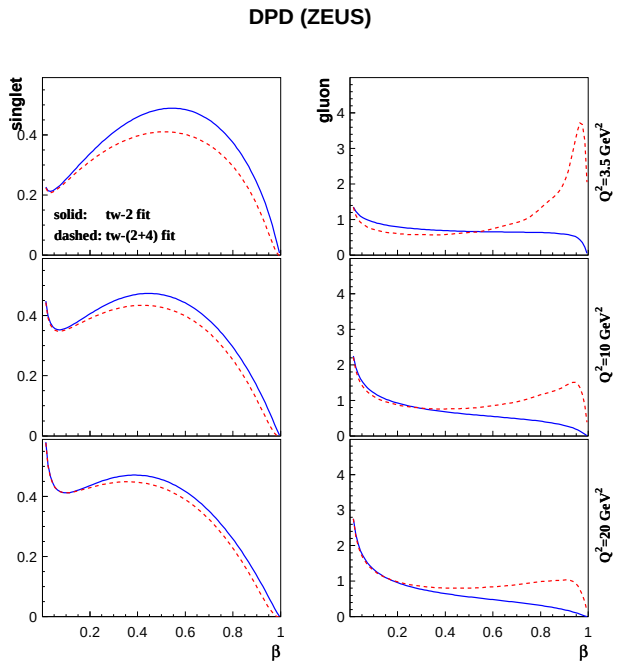

Figure 2.15: Pomeron parton distributions $\beta\Sigma_{I\!P}(\beta, Q^2)$ (left) and $\beta g_{I\!P}(\beta, Q^2)$ (right) from fits to ZEUS data.

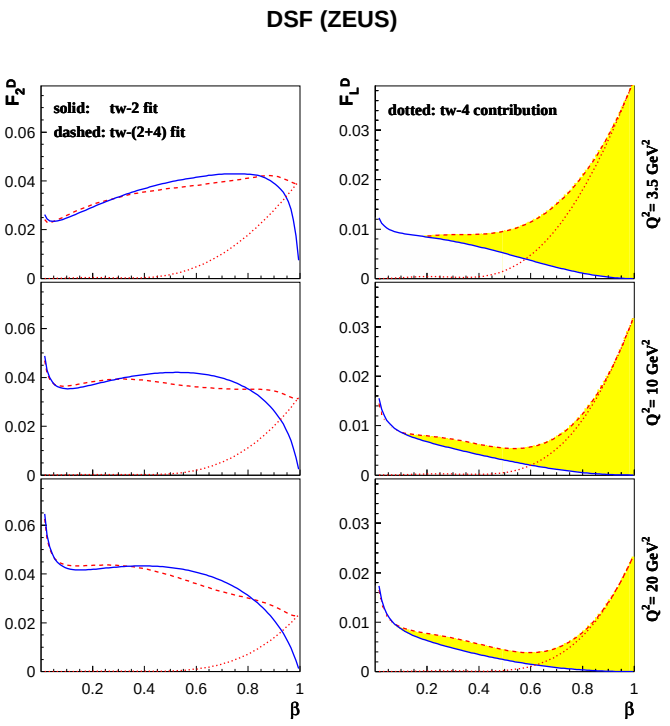

Figure 2.16: Diffractive structure functions $F_2^{D(3)}$ (left) and $F_L^{D(3)}$ (right) from fits to ZEUS data for $x_{I\!P} = 10^{-3}$. The band shows the effect of twist–4 on the predictions for $F_L^{D(3)}$.

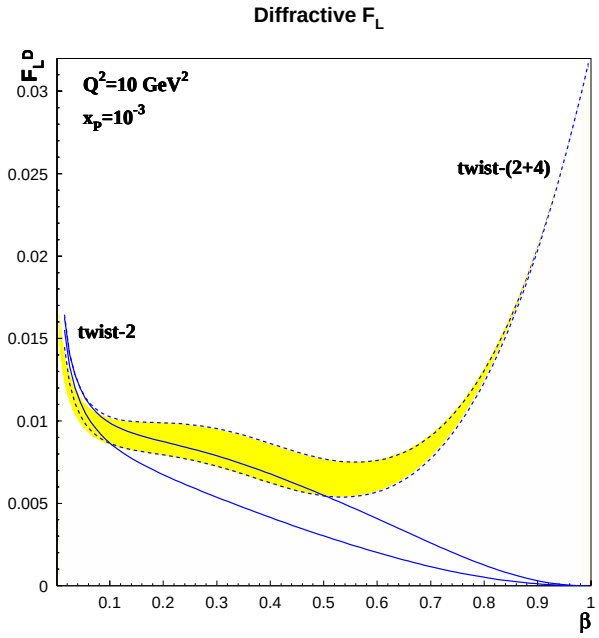

Figure 2.17: Predictions for $F_L^{D(3)}$ for $x_{I\!P} = 10^{-3}$ and $Q^2 = 10$ GeV^2 from the twist–(2+4) fits to the H1 (upper dashed line) and ZEUS (lower dashed line) data. The solid lines show predictions from pure twist–2 fits to the H1 (upper) and ZEUS (lower) data.

2.8 Prediction for the diffractive longitudinal structure function F_L^D

We summarize the effect of the twist–4 contribution in Fig. 2.17 showing the predictions for the diffractive longitudinal structure function which is supposed to be determined from HERA data. Ignoring this contribution, we find the two solid curves coming from the pure twist–2 analysis of the H1 (upper) and ZEUS (lower) data. With twist–4, the dashed curves are found, the upper curve from the H1 data and the lower one from the ZEUS data analysis. There is a significant difference between these predictions in the region of large β. Our effect is confirmed by the Preliminary H1 data analysis [80]. It is shown in Fig. 2.18.

2.9 Concluding remarks

In this chapter, diffractive parton distributions, obtained from fits to new diffractive data from the H1 and ZEUS Collaborations at HERA, are studied. In addition to the standard twist-2 formula, the twist-4 contribution, suppressed by an additional power of $1/Q^2$, but dominating in the region of large β, is considered. This contribution stems from the $q\overline{q}$ diffractive production from longitudinally polarized virtual photons. The effect of the twist-4 contribution on the distributions of diffractive parton and the diffractive structure functions was carefully examined. The twist-4 contribution leads to the diffractive gluon distribution, which is stronger peaked at $\beta \approx 1$ than the gluon distribution from the pure twist-2 fits. Regge contribution is also important in the analysis presented above. This contributions improves fit quality through better $x_{I\!P}$ shape. That's why the fit quality is better for H1 data, where Regge contributions is present, than for ZEUS data, where fits give Reggeon normalization $A_R \approx 0$

The main result of the analysis discussed here is a new prediction relevant to the diffractive longi-

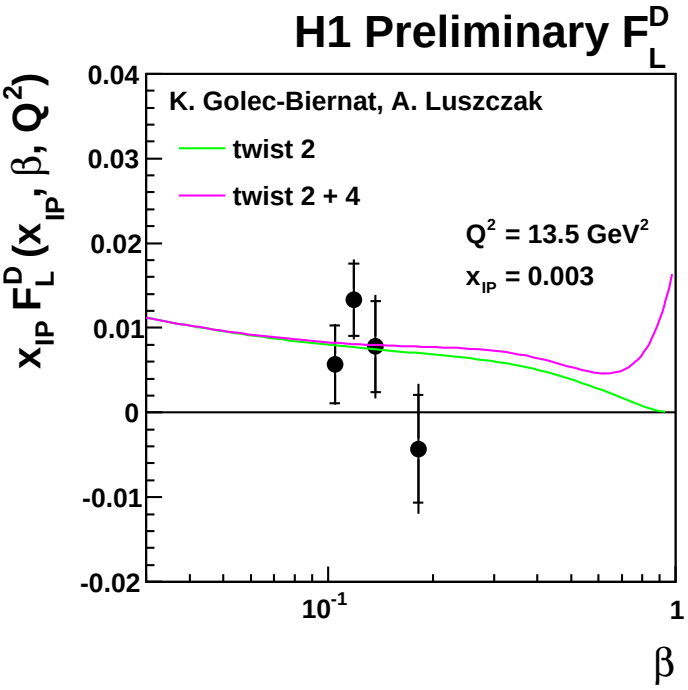

Figure 2.18: Comparison predictions for $F_L^{D(3)}$ with the Preliminary H1 data from [80].

tudinal structure function F_L^D. The twist-4 term in F_L^D makes this prediction significantly different in the region of large β from that one which is found in the pure DGLAP analysis. The last measurement of F_L^D at HERA in this region of β confirms the presented expectations, which are based on the perturbative QCD calculations. The obtained diffractive parton distributions can also be used in the analysis of diffractive processes at the LHC, particularly in the estimation of the background of the diffractive Higgs production. See [81] for a recent discussion.

Chapter 3

Dipole model description of DDIS

The most promising QCD-based approach to DIS diffraction is formulated in terms of dipole models. In these models, the diffractive (color singlet) state is systematically built from parton components of the light cone wave function of the virtual photon, see the following [18, 82] references. The lowest order state is formed by a quark-antiquark $(q\overline{q})$ pair while higher orders start from a $q\overline{q}g$ system in which a gluon is radiated by a quark or antiquark in the $q\overline{q}$ pair. We will focus on the first two components since they can be viewed in the configuration space as quark or gluon color dipoles. Their interaction with the proton is described by the quark or gluon dipole scattering amplitude $N(x, r, b)$. Here r and b are two-dimensional vectors of transverse separation and impact parameter, respectively, and x is the Bjorken variable, which brings the energy dependence. The dipole scattering amplitude is extracted from the DIS data on fully inclusive structure functions, assuming some physically motivated form with a few parameters [25, 83–85]. Then, it can be used in the description of diffractive processes [24, 75, 86–89]. The most interesting form of N is motivated by main features of parton saturation in dense partonic systems, such as the existence of a saturation scale $Q_s(x)$ [25]. From a formal point of view, such an amplitude fulfills local unitarity condition in the impact parameter space. The QCD-based evolution equation for N is derived in [90–93].

The main goal in this chapter is to confront the dipole model with two most popular parametrizations of the dipole scattering amplitude GBW (Golec-Biernat-Wüsthoffand) [25] and CGC (Color Glass Condensate) [76] with the newest data from HERA on the diffractive structure functions, obtained by the H1 [7] and ZEUS [66, 94] Collaborations.

The comparison we performed prompts us to discuss some subtle points of the dipole models, mostly related to the $q\bar{q}g$ component, and to connect them to the approach based on the diffractive parton distributions evolved with the Dokshitzer-Gribov-Lipatov-Altarelli-Parisi (DGLAP) equations.

In Section 3.1 we discuss various facts concerning the dipole approach to DIS diffraction. Next, in Section 3.2 we introduce the framework of the diffraction in dipole model and derive formula for diffractive structure function and its $q\bar{q}$ and $q\bar{q}g$ components. In Section 3.5 we perform a comparison of the dipole model results on the total diffractive structure functions with the HERA data [7, 94].

The results presented in this chapter are based on the original publication [95].

3.1 Dipole approach to DIS diffraction

The leading twist diffractive parton distributions functions (DPDF) allows for a good description of data. Nevertheless, the basic experimental fact that $\sigma^{diff}/\sigma^{tot} \simeq const$ as a function of energy W is not understood in this approach. The understanding is provided in a different theoretical framework of DIS diffraction, in which the virtual photon splits into a quark-antiquark pair that subsequently scatters off the target proton through a further quantum fluctuation. This picture is valid in the frame in which

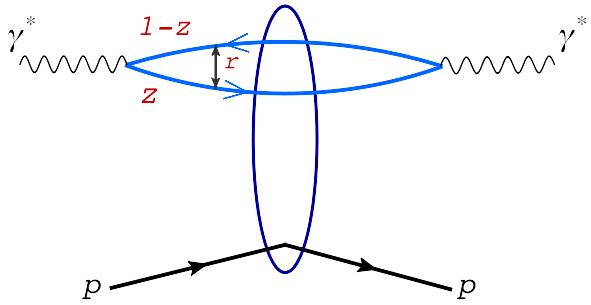

Figure 3.1: The photon-proton interaction in the dipole formalism at small x.

the $q\bar{q}$ pair (dipole) carries most of the available rapidity $Y \sim \ln(1/x)$ of the system, and the light-cone photon momentum amounts to the condition $q^+ > 0$. The gluon radiation from the parent dipole in the large N_c limit, can be interpreted as a collection of dipoles of different transverse sizes which interact with the proton. If the proton remains intact, the diffractive events with a large rapidity gap are formed. If this is the case, the diffractive system is created by the color dipoles and it is possible to model the pomeron by color singlet gluon exchange taking place between the dipoles and the proton.

In the simplest case, where only the parent $q\bar{q}$ dipoles form a diffractive system, the diffractive cross section at $t = 0$ reads [96]:

$$\frac{d\,\sigma^{diff}}{dt}_{|\,t=0} = \frac{1}{16\,\pi}\int d^2r\,dz\,|\Psi^{\gamma}(r,z,Q^2)|^2\,\hat{\sigma}^2(x,r), \tag{3.1}$$

where Ψ^{γ} is the well known light-cone wave function of the virtual photon, while r is the dipole transverse size and z is a fraction of the photon momentum q^+ carried by the quark. In this formula, the *dipole cross section* $\hat{\sigma}(x,r)$ describes the pomeron interaction, which in the QCD-approach is modelled by the exchange of gluons. The simplest two-gluon exchange does not depend on energy and has to be rejected. Since the DIS diffraction is a typical high energy (small x) phenomenon, it is tempting to apply the BFKL pomeron [39] with two reggeized, interacting gluons. Nevertheless, the resulting energy dependence is too strong in this case. Thus, more complicated gluon exchanges are necessary.

Particularly important are those [97] which do not lead to the violation of the Froissart's unitary bound for the total $\gamma^* p$ cross section: $\sigma^{tot} \leq c\ln^2 W^2$. Applying the $q\bar{q}$ dipole picture to σ^{tot}, the following relation holds in the small-x limit [96]

$$\sigma^{tot} = \int d^2r\,dz\,|\Psi^{\gamma}(r,z,Q^2)|^2\,\hat{\sigma}(x,r), \tag{3.2}$$

with the same dipole cross $\hat{\sigma}(x,r)$ as in (3.1). In order to fulfill the Froissart's bound, the following phenomenological form of the dipole cross section was proposed in [97, 98].

$$\hat{\sigma}(x,r) = \sigma_0\left\{1 - \exp(-r^2 Q_s^2(x))\right\}, \tag{3.3}$$

where $Q_s(x) = Q_0\,x^{-\lambda}$ is a saturation scale which parameters (together with σ_0) were found from a fit to all small-x data on $\sigma^{tot} \sim F_2/Q^2$. After fitting the dipole cross section parameters to the inclusive data on F_2, it can be used then to predict diffractive cross sections in DIS. This strategy was successfully applied in [24]. It is shown in Fig. 3.2.

Formula (3.3) captures essential features of parton saturation [25]. For $r \gg 1/Q_s(x)$ the dipole cross section saturates to a constant value σ_0, which may be regarded as a unitarity bound leading to

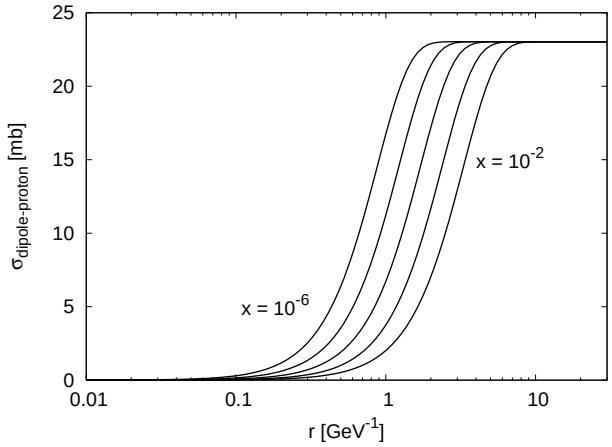

Figure 3.2: Dipole cross section in the GBW model (3.3) with $\sigma_0 = 23.03[mb]$, $\lambda = 0.288$ and $x_0 = 3.04.\,10^{-4}$. These parameters are from the original fit of Golec-Biernat and Wüsthoff [24].

the behavior respecting the Froissart bound. With decreasing x, the dipole cross section saturates for smaller dipoles, thus with increasing energy the proton blacken for the dipole probe of fixed transverse size. An important aspect of form (3.3), in which r and x are combined into one dimensionless variable $rQ_s(x)$, is geometric scaling. This a new scaling in inclusive DIS at small x [99]. Qualitatively, the behavior (3.3) can be found from an effective theory of dense parton systems with saturation – the Color Glass Condensate, see [98] and reference therein.

The DIS diffraction is an ideal process to study parton saturation since it is especially sensitive to the large dipole contribution, $r > 1/Q_s(x)$. Unlike inclusive DIS, the region below is suppressed by an additional power of $1/Q^2$. The dipole cross section with saturation (3.3) leads in a natural way to the constant ratio (up to logarithms) [25]

$$\frac{\sigma^{diff}}{\sigma^{tot}} \sim \frac{1}{\ln(Q^2/Q_s^2(x))}\,. \tag{3.4}$$

3.2 Diffraction in dipole models

3.2.1 Diffractive structure functions

In dipole models of ep diffractive deep inelastic scattering, the diffractive structure function F_2^D is a sum of components corresponding to different diffractive final states produced from two polarizations of the virtual photon: transverse (T) and longitudinal (L). In the lowest order the diffractive state consists of a quark-antiquark $(q\overline{q})$ pair. The higher order takes gluons and more quark-antiquark pairs into account.

In our approach we consider three components: $q\overline{q}$ pairs from transverse and longitudinal photons and a $q\overline{q}g$ component from transverse photons, see Fig. 3.3. Thus the structure function takes the form

$$F_2^D = F_T^{q\overline{q}} + F_L^{q\overline{q}} + F_T^{q\overline{q}g}\,. \tag{3.5}$$

Below we provide analytic formulas for the three components.

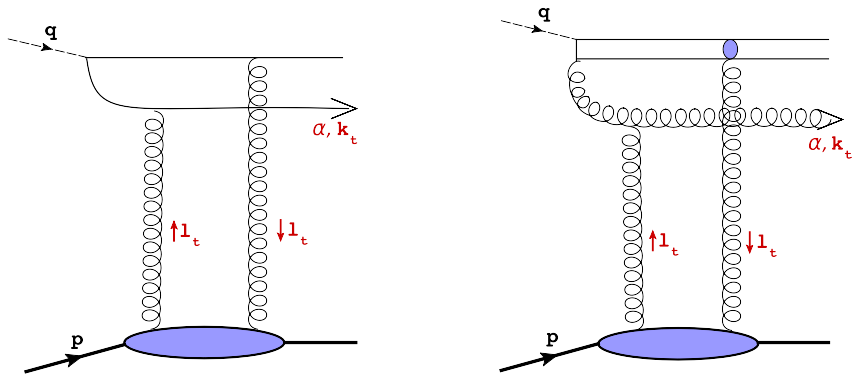

Figure 3.3: The $q\overline{q}$ and $q\overline{q}g$ components of the diffractive structure function.

3.3 The transverse and longitudinal $q\bar{q}$ components

The $q\overline{q}$ component from transverse photons is given by

$$x_{I\!P} F_T^{(q\overline{q})} = \frac{3Q^4}{64\pi^4 \beta B_d} \sum_f e_f^2 \int_{z_f}^{1/2} dz\, z(1-z) \left\{ [z^2 + (1-z)^2]\, \overline{Q}_f^2\, \phi_1^2 \,+\, m_f^2\, \phi_0^2 \right\} \tag{3.6}$$

$$x_{I\!P} F_L^{(q\overline{q})} = \frac{3Q^4}{16\pi^4 \beta B_d} \sum_f e_f^2 \int_{z_f}^{1/2} dz\, Q^2 z^3 (1-z)^3\, \phi_0^2 \tag{3.7}$$

where we sum over quark flavors f. The variable

$$z_f = \tfrac{1}{2}\left(1 - \sqrt{1 - 4m_f^2/M^2}\right) \tag{3.8}$$

and

$$\overline{Q}_f^2 = z(1-z)Q^2 + m_f^2\,. \tag{3.9}$$

B_d is the so called diffractive slope and the functions ϕ_i take the following form for $i = 0, 1$

$$\phi_i = \phi_i(x_{I\!P}, z, k_f, Q^2) = \int_0^\infty dr r K_i(\overline{Q}_f r)\, J_i(k_f r)\, \hat{\sigma}(x_{I\!P}, r)\,, \tag{3.10}$$

where k_f is transverse momentum of quark f

$$k_f^2 = z(1-z)M^2 - m_f^2 \tag{3.11}$$

and K_i and J_i are Bessel functions.

The lower integration limits in Eqs. (3.6) and (3.7) correspond to the minimal value of z at which the diffractive final state with mass M can be produced. From (3.11) we see that such a z correspond to the quark transverse momentum $k_f = 0$. For massless quarks, $m_f = 0$, the lower limit $z_f = 0$. When the threshold for the diffractive $q\overline{q}$ state production is approached, $M^2 \to 4m_f^2$, we have $z_f \to 1/2$ and the components $F_{T,L}^{(q\overline{q})} \to 0$.

3.3.1 Dipole cross section

The quantity $\hat{\sigma}(x_{I\!P}, r)$ in Eq. (3.10) is a dipole cross section describing the diffractive interaction of the $q\overline{q}$ pair (dipole) with a proton. It is related to the corresponding dipole scattering amplitude $N(x_{I\!P}, r, b)$ through the formula

$$\hat{\sigma}(x_{I\!P}, r) = 2 \int d^2b \, N(x_{I\!P}, r, b) \, . \tag{3.12}$$

We are going to compare the presented dipole description of the diffractive structure functions with the newest HERA data. For this purpose, we consider two parametrizations of the dipole cross section which are based on the idea of parton saturation in dense gluon systems. The first one is the GBW parametrization with heavy quarks, [25], which has played an inspirational role in studies of parton saturation in the recent ten years. In this parametrization we added quark c and $f = u, d, s, c$. The second one is the CGC parametrization [76, 85] which somehow summarizes the studies within the Color Glass Condensate [50] approach to parton saturation. Quite surprisingly, these two parametrizations give very similar results for the diffractive structure functions. The main reason is the same normalization of the dipole cross section, σ_0 see Fig. 3.4. The origin of the same numerical value, however, is different. For the GBW parametrization σ_0 is fitted to the data for F_2 while for the CGC parametrization it is computed from a diffractive slope B_D, see Eq. (3.18).

The two considered parametrizations, specified below, describe very well the inclusive DIS data on the structure function F_2. Their use for the DDIS description is a very important test of the universality of the dipole approach to DIS diffraction.

- The GBW parametrization with heavy quarks has the following form of the $q\overline{q}$ dipole cross section [25]

  $$\hat{\sigma}(x_{I\!P}, r) = \sigma_0 \left(1 - \exp(-r^2 Q_s^2/4)\right), \tag{3.13}$$

  where $\sigma_0 = 29$ mb, and the saturation scale is given by

  $$Q_s^2 = (x_{I\!P}/x_0)^{-\lambda} \ \mathrm{G}eV^2, \tag{3.14}$$

  with $x_0 = 4 \cdot 10^{-5}$ and $\lambda = 0.288$. The dipole scattering amplitude in such a case reads

  $$\hat{N}(x_{I\!P}, \mathbf{r}, \mathbf{b}) = \theta(b_0 - b) \left(1 - \exp(-r^2 Q_s^2/4\right) , \tag{3.15}$$

  where $2\pi b_0^2 = \sigma_0$. This form corresponds to a model of the proton with a sharp edge.

- The CGC parametrization with heavy quarks of the quark dipole scattering amplitude is given by [75, 76, 85]

  $$\hat{N}(x_{I\!P}, \mathbf{r}, \mathbf{b}) = S(\mathbf{b}) \, N(x_{I\!P}, \mathbf{r}) \, , \tag{3.16}$$

  where the form factor $S(\mathbf{b}) = \exp(-b^2/(2B_d))$ with the diffractive slope from HERA, $B_d = 6 \ \mathrm{G}eV^{-2}$. Thus, the dipole cross section (3.12) is given by the formula

  $$\hat{\sigma}(x_{I\!P}, \mathbf{r}) = 4\pi B_d \, N(x_{I\!P}, \mathbf{r}) \, . \tag{3.17}$$

  We see that the asymptotic value of $\hat{\sigma}$ for $r \to \infty$ is the same as for the GBW parametrization, if the diffractive slope measured at HERA is substituted,

  $$\sigma_0 = 4\pi B_d = 29 \ \mathrm{m}b \tag{3.18}$$

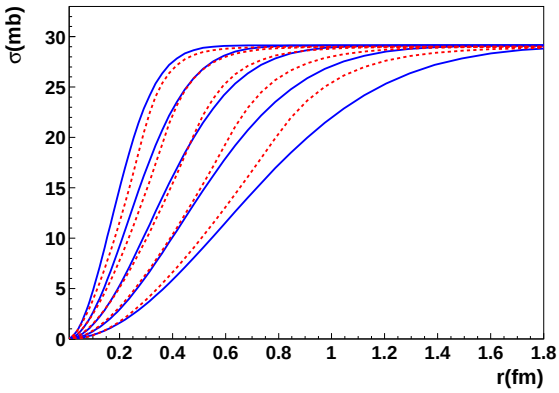

Figure 3.4: The dipole cross section as a function of r for $x = 10^{-2} \ldots 10^{-6}$ (from right to left) and for the GBW (continuous lines) and CGC (dashed lines) parametrization.

In addition,

$$N(\mathbf{r},x) = \begin{cases} N_0 \left(\frac{rQ_s}{2}\right)^{2\gamma_s} \mathrm{e}^{\frac{2\ln^2(rQ_s/2)}{\kappa\lambda\ln(x)}} & \text{for} \quad rQ_s \leq 2 \\ 1 - \mathrm{e}^{-4\alpha\ln^2(\beta rQ_s)} & \text{for} \quad rQ_s > 2, \end{cases} \tag{3.19}$$

where the saturation scale Q_s has now the following parameters: $\lambda = 0.22$ and $x_0 = 1.63 \cdot 10^{-5}$. The parameters $\alpha = 0.615$ and $\beta = 1.006$ are chosen such that N and its first derivative are continues at the point r where $N(r) = N_0 = 0.7$. The remaining parameters are given by $\kappa = 9.9$ and $\gamma_c = 0.7376$.

Both parametrizations provide the energy dependence of the diffractive structure function through the variable $x_{I\!P}$. This dependence is determined from fits of the dipole model formula for F_2 into the data from HERA for the Bjorken variable $x \leq 0.01$. In the case of DDIS, x is substituted by $x_{I\!P}$.

3.4 The transverse $q\bar{q}g$ component

The $q\overline{q}g$ diffractive component from transverse photons, computed for massless quarks, $m_f = 0$, is given by the formula

$$x_{I\!P} F_T^{(q\bar{q}g)} = \frac{81\beta\alpha_s}{512\pi^5 B_d} \sum_f e_f^2 \int_\beta^1 \frac{dz}{(1-z)^3} \left[\left(1 - \frac{\beta}{z}\right)^2 + \left(\frac{\beta}{z}\right)^2 \right]$$
$$\times \int_0^{(1-z)Q^2} dk^2 \log\left(\frac{(1-z)Q^2}{k^2}\right) \phi_2^2(x_{I\!P}, z, k) \ , \tag{3.20}$$

where the function ϕ_2 takes to form

$$\phi_2(x_{I\!P}, z, k) = k^2 \int_0^\infty dr\, r\, K_2\left(\sqrt{\frac{z}{1-z}} kr\right) J_2(kr)\, \hat{\sigma}(x_{I\!P}, r) \ . \tag{3.21}$$

with K_2 and J_2 being the Bessel functions. Notice that the energy dependence of F_2^D in the dipole models comes through the $x_{I\!P}$ dependence of the dipole cross section $\hat{\sigma}(x_{I\!P}, r)$.

Formula (3.20) was computed with two gluons exchanged between the diffractive system and the proton. This brings into the normalization of the scattering amplitude the relative color factor C_A/C_F with respect to the $q\overline{q}-$proton scattering amplitude. Then the two gluon exchange is substituted by the dipole cross section for the $q\overline{q}$ dipole interaction with the proton. For example, for the GBW parametrization

$$\hat{\sigma} \equiv \hat{\sigma}_{q\overline{q}} = \sigma_0 \left(1 - \mathrm{e}^{-r^2 Q_s^2/4}\right) . \tag{3.22}$$

There exists another approach in which the two gluon exchange formula is eikonalized with the color factor absorbed into the exponent. For the GBW parametrization this leads to the following gluon dipole cross section in Eq. (3.21)

$$\hat{\sigma} \equiv \hat{\sigma}_{gg} = \sigma_0 \left(1 - \mathrm{e}^{-(C_A/C_F) r^2 Q_s^2/4}\right) . \tag{3.23}$$

In such a case, the color factor $C_A/C_F = 9/4$ (for $N_c = 3$) disappears from the normalization of the scattering amplitude and we have to rescale the structure function in the following way

$$F_T^{(q\overline{q}g)} \;\rightarrow\; \frac{1}{(C_A/C_F)^2}\, F_T^{(q\overline{q}g)} . \tag{3.24}$$

By the comparison with HERA data, we will show in the next section that the latter possibility is more appropriate for the data description.

We summarize our considerations referring to Fig. 1.16, from Section 1.6 which shows the three diffractive components of F_2^D: $q\overline{q}T$, $q\overline{q}L$ i $q\overline{q}gT$, as a function of β. We emphasize once again that each component has its own dominance region:

- $F_T^{(q\overline{q})}$ component dominates for $\beta \sim 1/2$ when $M^2 \sim Q^2$
- $F_L^{(q\overline{q})}$ component dominates for $\beta \rightarrow 1$ when $M^2 \ll Q^2$
- $F_T^{(q\overline{q}g)}$ component dominates for $\beta \rightarrow 0$ when $M^2 \gg Q^2$.

3.5 Comparison with HERA data

In Figs. 3.5, 3.6 and 3.7 we show a comparison of the dipole model predictions with the ZEUS Collaboration data [94] and the H1 Collaboration data [7] on the reduced cross section

$$\sigma_r^D = F_2^D - \frac{y^2}{1 + (1-y)^2} F_L^D . \tag{3.25}$$

We included the charm contribution in the above structure functions. The solid lines correspond to the GBW parametrization of the dipole cross section with the color factor modifications (3.23) and (3.24) of the $q\overline{q}g$ component, while the dotted (red) lines are obtained from the CGC parametrization. We see that the two sets of curves are barely distinguishable. This somewhat surprising results could be attributed to the same normalization of the dipole cross section in both models, $\sigma_0 = 29\ \mathrm{mb}$. Let us emphasize again that this numerical value was obtained in two different ways (see Sec. 3.3.1 for more details). The dashed (red) lines on these Figs. show the contribution without charm.

The color factor modification of the $q\overline{q}g$ component in the GBW parametrization is necessary since the curves without such a modification significantly overshoot the data (by a factor of two or so) in the

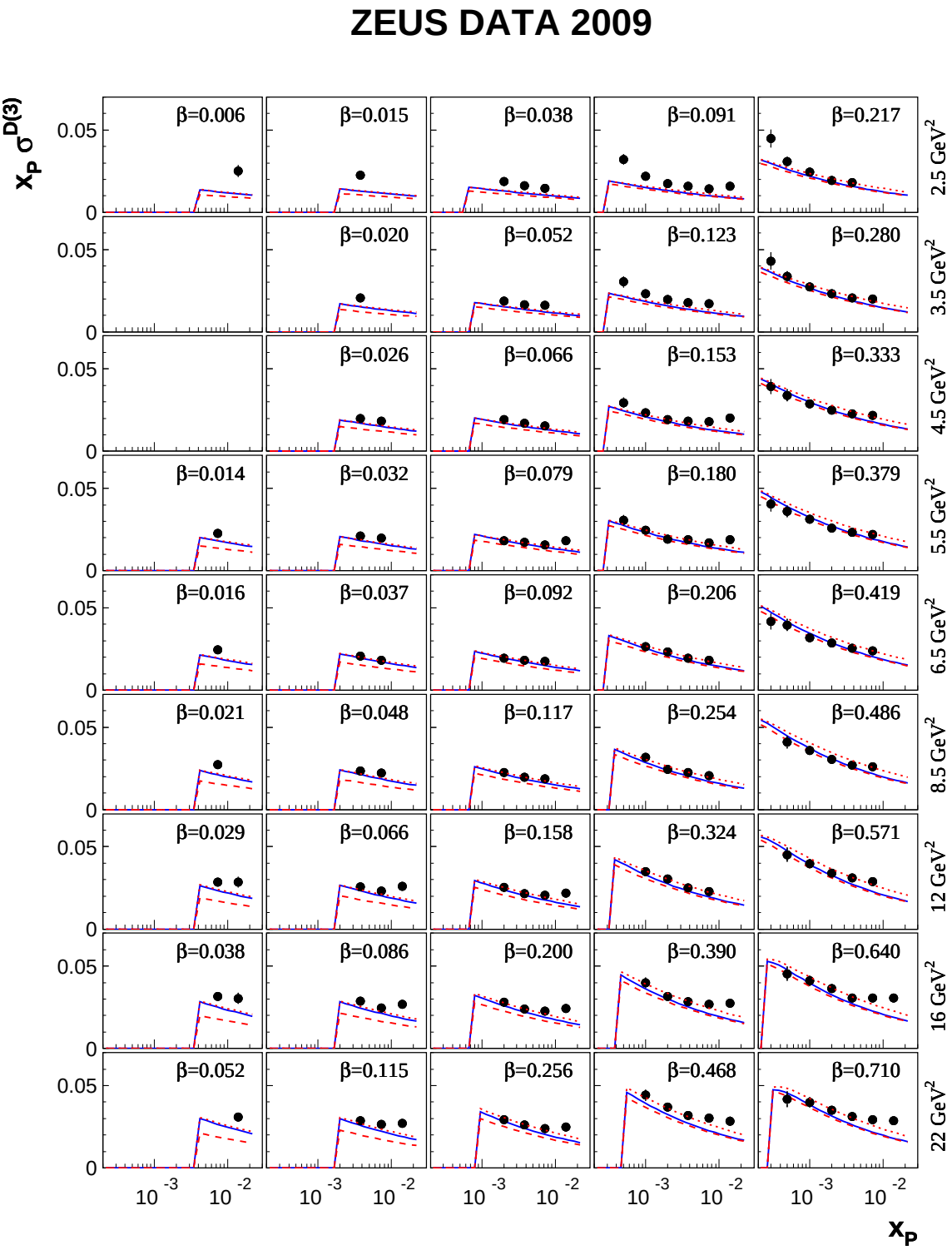

Figure 3.5: A comparison of σ_r^D from the two considered dipole models with the newest ZEUS Collaboration data [94]. The solid lines correspond to the GBW parametrization of the dipole cross section with the color factor modifications (3.23) and (3.24), while the dotted lines correspond to the CGC parametrization. The dashed lines show the results without the charm contribution.

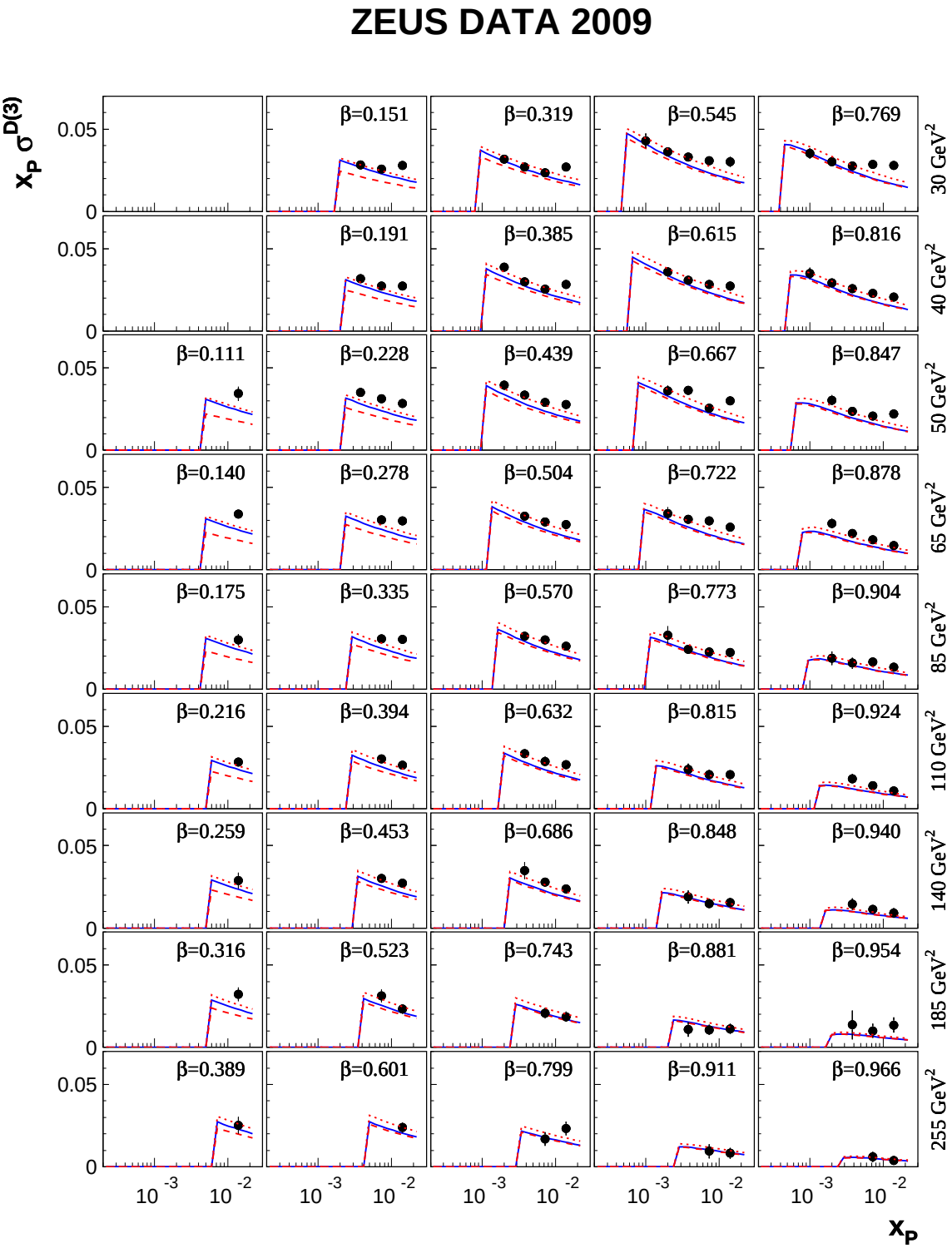

Figure 3.6: The same as in Fig. 3.5 but for higher values of Q^2.

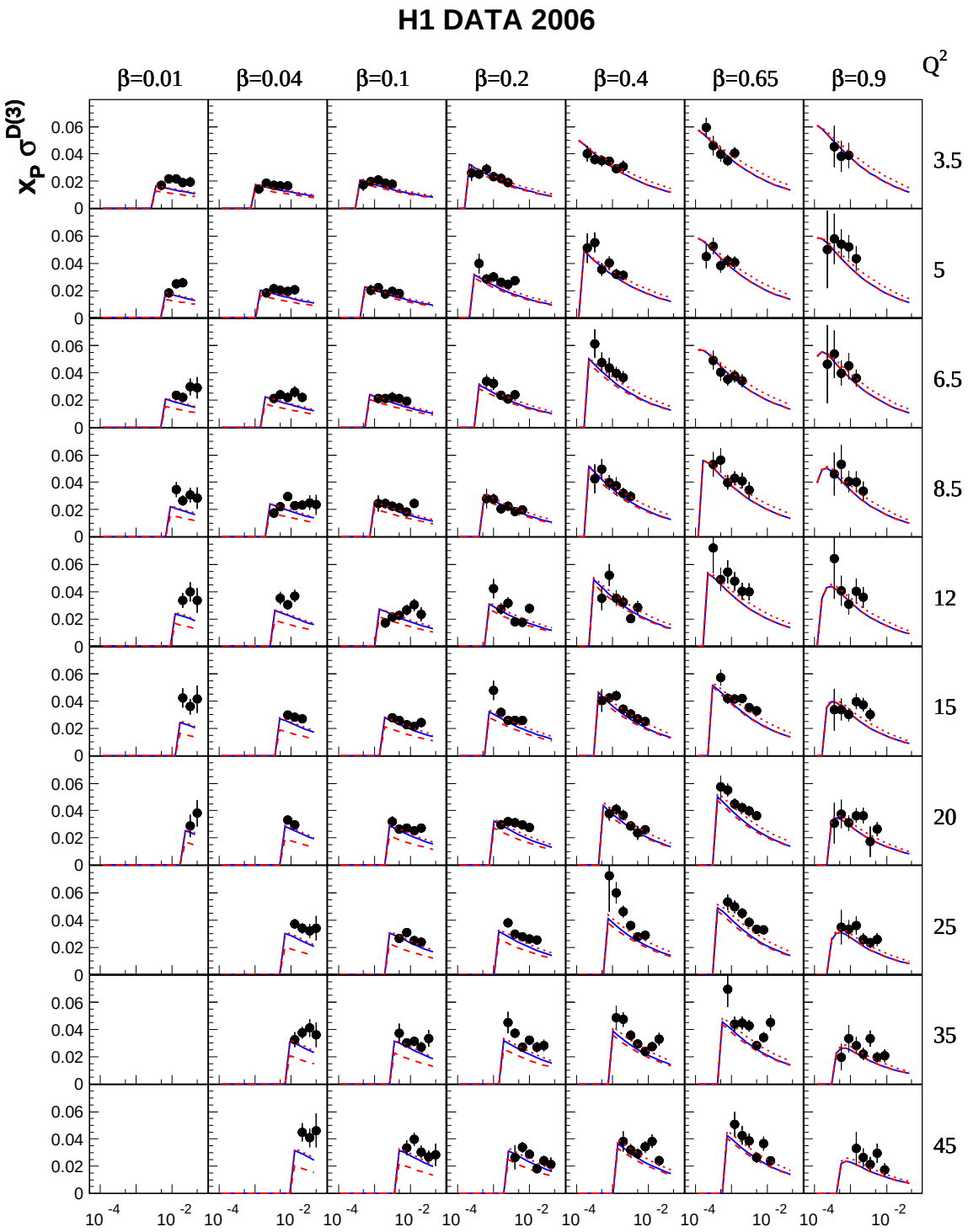

Figure 3.7: The same as in Figs. 3.5 and 3.6 but for the H1 Collaboration data on the reduced cross section σ_r^D [7]. The dashed lines show the contribution without charm.

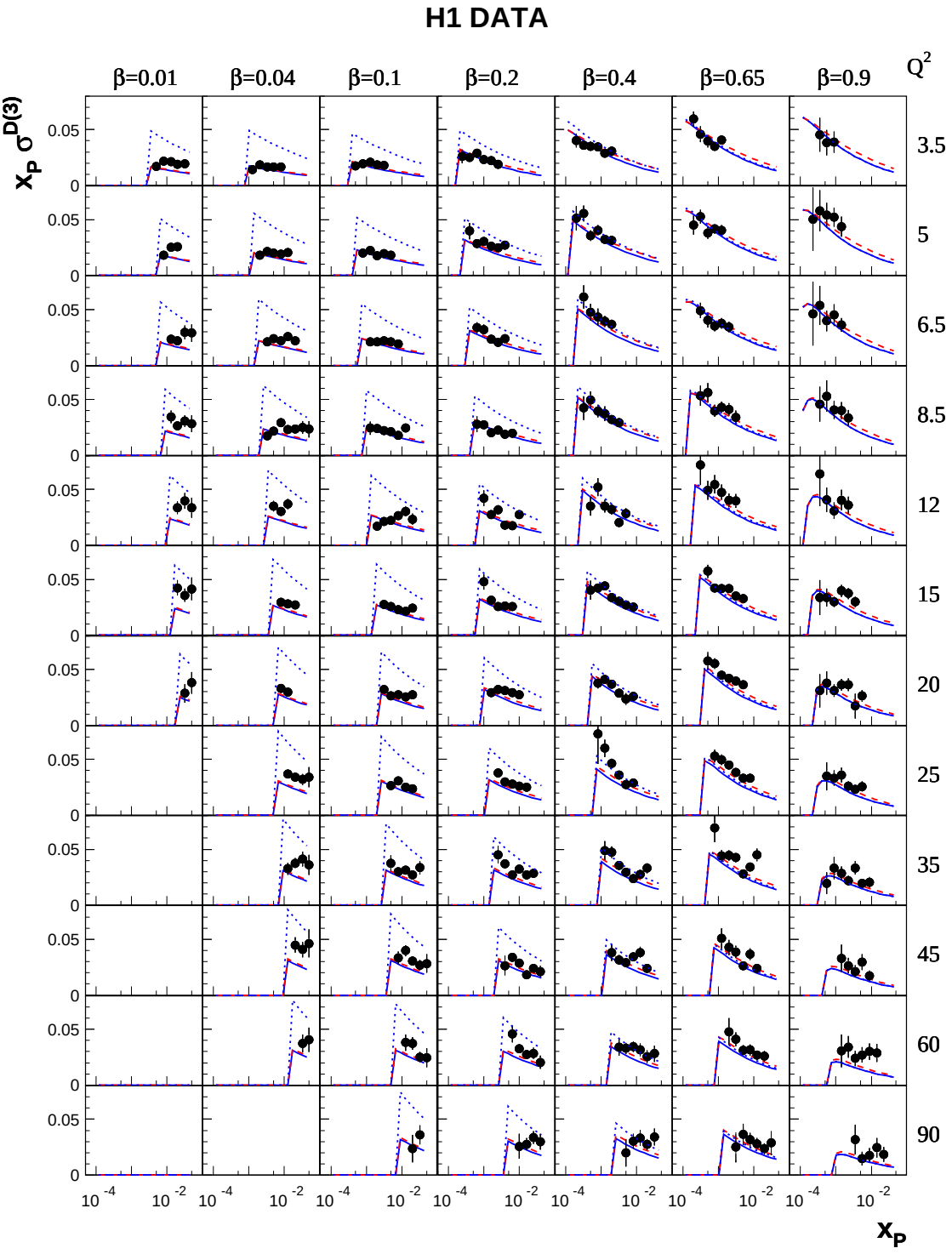

Figure 3.8: The comparison of σ_r^D from dipole models with HERA data from the H1 collaboration. The solid lines correspond to the GBW parametrization with the color factor modification of $F_T^{q\bar{q}g}$ while the dashed lines correspond to the CGC parametrization. The dotted lines show the GBW parametrization without the color factor modification.

region of small β where the $q\overline{q}g$ component dominates. It is shown in Fig. 3.8 for H1 Collaboration data [7]. We checked that this is also true for ZEUS Collaboration data analyzed here.

The comparison of the predictions with the data also reveals a very important aspect of the three component dipole model Eq. (3.5). In the small β region, the curves are systematically below the data points, which effect may be attributed to the lack of higher order components in the diffractive state, i.e. with more than one gluon or $q\overline{q}$ pair. They may be added in the DGLAP based approach to inclusive diffraction which sums additional partonic emissions in the diffractive state in the transverse momentum ordering approximation. A comprehensive discussion of the DGLAP based fits to the diffractive HERA data is presented in Chapter 2. We recall that in this approach the diffractive structure functions are twist-2 quantities with the logarithmic dependence on Q^2 for fixed $x_{I\!P}$ and β. They are related to the diffractive parton distributions by the standard collinear factorization formula, ***e.g.*** in the leading $\log Q^2$ approximation we have for F_2^D:

$$F_2^{D(3)} = \sum_f e_f^2 \, \beta \, \left\{ q_f^D(x_{I\!P}, \beta, Q^2) + \overline{q}_f^D(x_{I\!P}, \beta, Q^2) \right\} = \frac{1}{N_f} \sum_f e_f^2 \, \beta \, \Sigma^D(x_{I\!P}, \beta, Q^2) \, , \qquad (3.26)$$

where we assume flavor democracy for all quark distributions to account for vacuum quantum number exchange responsible for diffraction, this Σ^D is the singlet quark distribution and N_f is the number of active flavors. See also Eqs. 2.23 and 2.27 from previous Chapter. This distribution is evolved in Q^2 by the DGLAP evolution equations together with the diffractive gluon distribution $g_D(x_{I\!P}, \beta, Q^2)$. In contrast to the dipole model case, the $x_{I\!P}$ dependence of the parton distributions is fitted to data together with their form in β at some initial scale Q_0^2.

In [61] we raised the question of higher twist corrections to the leading twist structure functions. In the inclusive case such corrections to the structure function F_2 seem to be small, at least for not too small values of Q^2 and x (replaced by β in DDIS). However, from Fig. 1.16 we see that for large β the higher twist $F_L^{q\overline{q}}$ contribution dominates the leading twist components. Since this contribution describes well the existing data for $\beta \to 1$, we include it into the DGLAP fits of diffractive parton distributions. The $q\overline{q}L$ contribution has the main impact on the longitudinal structure function F_L^D, what we proved in Section 2.8.

Regarding our predictions using dipole models, it is also important that the charm contribution, described in Chapter 4, is added into the analysis, presented in Figs. 3.5, 3.6 and 3.7. Without this contribution the comparison would be much worse than that shown here.

3.6 Dipole approach vs DGLAP approach

The relation between the dipole approach with three diffractive components and the DGLAP approach with diffractive parton distributions was analyzed at length in [60]. Summarizing this relation, the twist–2 part of the dipole approach leads to diffractive quark and gluon distributions which we present in Sections 4.1 and 4.2. The quark distribution $\Sigma^D(x_{I\!P}, \beta, Q^2)$ is independent of Q^2, thus it may only serve as an initial conditions for the DGLAP evolution equations. The value of the initial scale, however, cannot be determined in the dipole approach. The twist-2 part of $q\overline{q}g$ component forms a first step of the DGLAP evolution in logarithms of Q^2 and leads to the diffractive gluon distribution $g^D(x_{I\!P}, \beta, Q^2)$ with a mild Q^2 dependence.

From this perspective, the DGLAP approach offers a description of more complicated diffractive states with any number of partons with ordered transverse momenta. However, the perturbative QCD calculations tell us that the twist–2 DGLAP analysis of diffractive data should be combined with the twist–4 contribution which cannot be neglected at large β. This is the strategy which we have follow in our analysis in the previous Chapter. We also borrow from the dipole approach a general form in

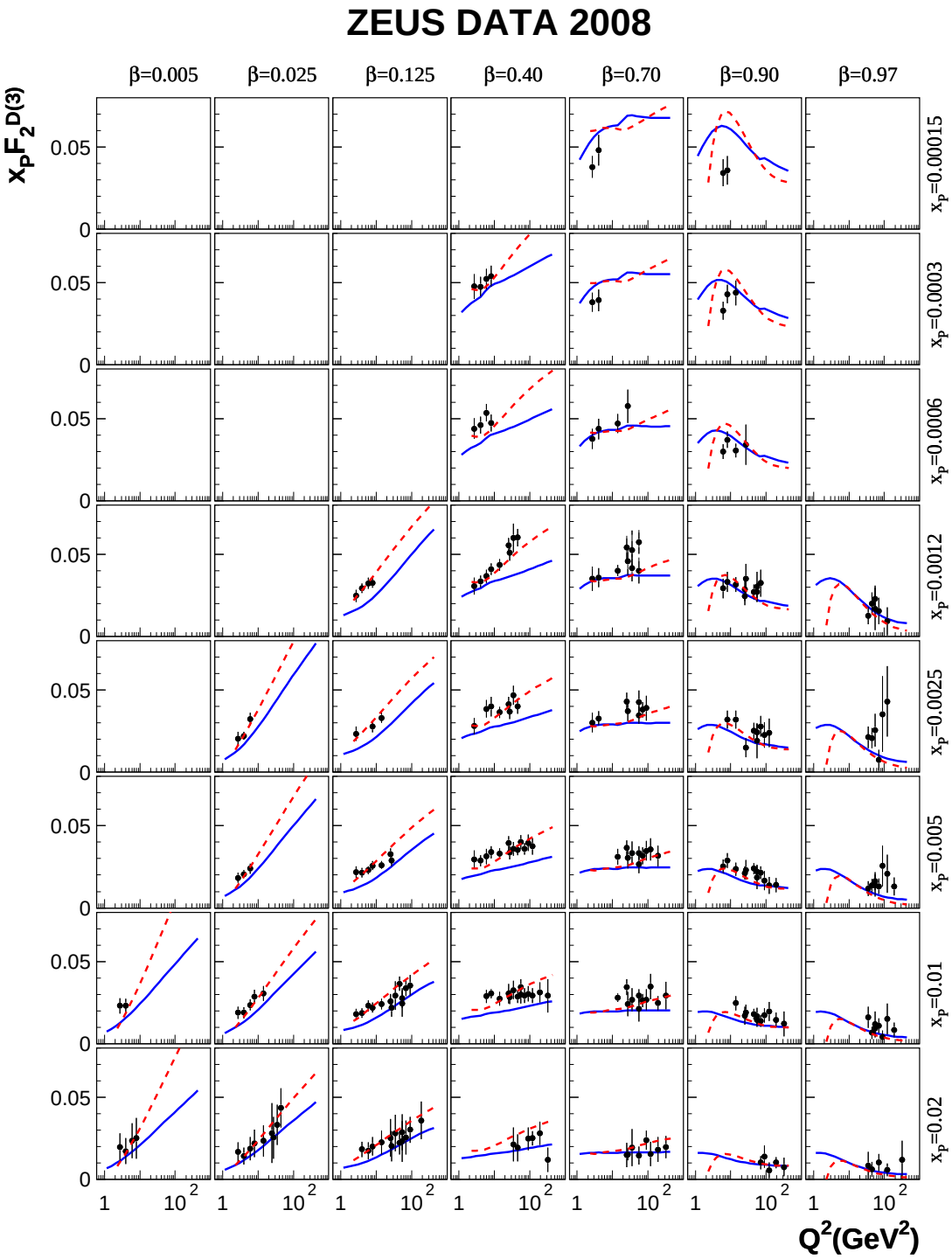

Figure 3.9: The comparison of the GBW dipole model prediction with the color factor modification (solid lines) and the results from the DGLAP fit to the ZEUS data (dashed lines).

β of the initial singlet quark distribution which vanishes at the endpoints $\beta = 0, 1$, see Eq. (2.44) in which the coefficients A_q and C_q appears to be positive from fits.

A very important aspect of Regge factorization of the diffractive parton distributions (DPD) from Eq. (2.25) can also be motivated by the dipole approach. As shown in [60], Regge factorization is a consequence of geometric scaling of the dipole cross section from Eq. (2.34) [99]. The assumption that $\hat{\sigma}$ is a function of the dimensionless ratio $rQ_s(x)$ has a remarkable consequence for the $x_{I\!P}$ dependent of the diffractive parton distributions found in the dipole approach, namely

$$x_{I\!P}\Sigma^D(\beta, x_{I\!P}) = Q_s^2(x_{I\!P})\,\Sigma^{I\!P}(\beta) \tag{3.27}$$

$$x_{I\!P}g^D(\beta, x_{I\!P}) = Q_s^2(x_{I\!P})\,g^{I\!P}(\beta). \tag{3.28}$$

This type of factorization is similar to Regge factorization but in fact has no connection with Regge theory. Since the evolution does not affect the $x_{I\!P}$-dependence of the DPD, the factorized form will be valid for any scale Q^2.

Now, we can write for the leading twist part of the diffractive structure function:

$$x_{I\!P}F_2^{D(3)(LT)} = Q_s^2(x_{I\!P})\,\frac{1}{2N_f}\sum_f e_f^2\,\Sigma^{I\!P}(\beta) \tag{3.29}$$

in which the dependence on $x_{I\!P}$ is factored out. The dependence on Q^2 of the distributions $q_f^{I\!P}$ is introduced by the evolution equations. In the saturation model [25] the parameter $\lambda = 0.29$ in the relation $Q_s^2(x) \sim x^{-\lambda}$ was determined from a fit to inclusive DIS data only.

The same value holds for diffractive interactions, thus we find a definite prediction for the $x_{I\!P}$ dependence of the leading twist diffractive structure function

$$F_2^{D(3)(LT)} \sim x_{I\!P}^{-1-\lambda}\,. \tag{3.30}$$

At present, the bulk of diffractive data in DIS support the factorized form (3.30). They are usually interpreted in terms of the t-averaged pomeron intercept $\overline{\alpha}_{I\!P}$, *i.e.* $F_2^{D(3)} \sim x_{I\!P}^{1-2\overline{\alpha}_{I\!P}}$. Thus, for the value $\lambda = 0.29$, we find

$$\overline{\alpha}_{I\!P} = \lambda/2 + 1 \approx 1.15, \tag{3.31}$$

which is in remarkable agreement with the values found at HERA, $\overline{\alpha}_{I\!P} = 1.17$ by H1 [7] and $\overline{\alpha}_{I\!P} = 1.13$ by ZEUS [66].

Summarizing, the leading twist description extracted from the saturation model of DIS diffraction leads to the factorization of the $x_{I\!P}$ dependent part of the cross section similar to Regge factorization. It correctly predicts the value of the effective pomeron intercept. The Q^2 dependence of the diffractive structure function does not affect the $x_{I\!P}$ factorization.

This means that the saturation model gives effectively the result which coincides with the Regge approach, although the physics behind is completely different. The relative hardness of the intrinsic scale $Q_s(x_{I\!P}) \sim 1$ GeV in the saturation models suggests that the DDIS at HERA is a semihard process rather than a soft process as Regge theory would require.

In Fig. 3.9 we show the comparison of the results from the two discussed above approaches with the recent ZEUS data [66]. In the most interesting small β region, the DGLAP fit curves (dashed lines) are closer to the data then the ones with the $q\overline{q}g$ component (solid lines) from GBW dipole model. In particular, the logarithmic slope in Q^2 of F_2^D is steeper in the DGLAP approach. This illustrates the importance of more complicated diffractive states then the $q\overline{q}g$ state.

3.7 Conclusions

To sum up, we presented a comparison of the dipole model results on the diffractive structure functions with the newest HERA data. We considered two most popular parametrization of the interaction between the diffractive system and the proton (the GBW and CGC parametrizations) which are based on the idea of parton saturation. The three component model with the $q\overline{q}$ and $q\overline{q}g$ diffractive states describe reasonable well the recent data. However, the region of small values of β needs some refinement by considering components with more gluons and $q\overline{q}$ pairs in the diffractive state. This can be achieved in the DGLAP based approach which sums partonic emissions in the diffractive state in the transverse momentum ordering approximation.

Chapter 4

Diffractive heavy quark production

In this chapter we calculated diffractive charm production using dipole model approach and collinear factorization approach with DGLAP fits. We compared our results with the recent data from HERA, relevant to charm diffractive structure function [100]. According to the collinear factorization approach, it is expected that diffractive open charm production at HERA proceeds mainly via boson gluon fusion (BGF) as it is presented in Fig. 4.1. In the BGF process a charm quark anti-quark pair $(c\overline{c})$ is produced of which one quark couples to the photon with virtuality Q^2 and the other to a gluon emerging from the diffractive exchange. This process is expected to be dominant for diffractive open charm production in DIS. It is important, that BGF process is sensitive in a direct manner to the gluon content of the diffractive exchange, which is only determined indirectly and for low momentum fractions $z_{I\!P}$ of the gluon in inclusive diffractive scattering via scaling violations [7].

We start from introducing the diffractive quark and gluon distributions, respectively, in Sections 4.1 and 4.2. These distributions can be defined in the dipole models by extracting the leading twist component of F_2^D. It is interesting to compare them with those found in the DGLAP fits. In particular, knowing the gluon distribution in these two distinct approaches, we will find predictions for the diffractive charm production, measured recently at HERA. Predictions for the diffractive charm production are presented in Section 4.3.

The results presented in Section 4.3 are based on the original publication [95].

4.1 Diffractive quark distributions

In the leading logarithmic collinear approximation the diffractive structure function F_2^D is related to the diffractive quark distributions q^D and $\overline{q}_f^D$ by the formula

$$F_2^D(x_{I\!P},\beta,Q^2) = \sum_f e_f^2\,\beta\,(q_f^D + \overline{q}_f^D) = \frac{1}{N_f}\sum_f e_f^2 \beta\,\Sigma^D\,, \tag{4.1}$$

where

$$\Sigma^D(x_{I\!P},\beta,Q^2) = \sum_f (q_f^D(x_{I\!P},\beta,Q^2) + \overline{q}_f^D(x_{I\!P},\beta,Q^2)) \tag{4.2}$$

is the singlet quark distribution and N_f is the number of active quark flavors.

In order to find the quark distribution resulting from dipole models, we only consider the transverse photon contribution $F_T^{(q\overline{q})}$, given by Eq. (3.6), since the longitudinal component, $F_L^{(q\overline{q})}$, is proportional to $1/Q^2$ for large Q^2. Thus, formally it is higher twist which does not contribute to parton distributions

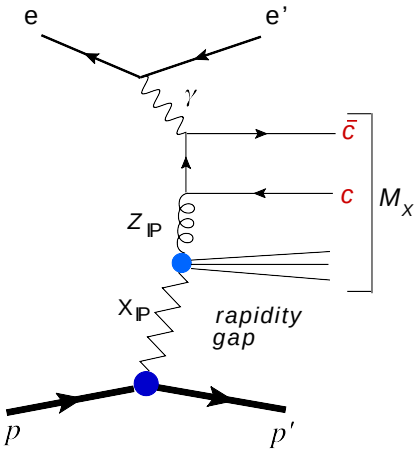

Figure 4.1: Direct process of diffractive charm production, where the photon enters the hard scatter itself.

in the collinear approach. For massless quarks, $m_f = 0$, we have

$$x_{I\!P} F_T^{(q\bar{q})} = \frac{3Q^6}{64\pi^4 \beta B_d} \sum_f e_f^2 \int_0^{1/2} dz\, z^2(1-z)^2 \left[z^2 + (1-z)^2\right] \phi_1^2(x_{I\!P}, z, k), \tag{4.3}$$

where $k^2 = z(1-z)M^2$ and

$$\phi_1(x_{I\!P}, z, k) = \int_0^\infty dr r\, K_1\Big(\sqrt{z(1-z)}Qr\Big)\, J_1(kr)\, \hat{\sigma}(x_{I\!P}, r)\,. \tag{4.4}$$

Let us change the integration variable, $z \to k^2$, in Eq. (4.3). We find

$$\int_0^{1/2} dz\, z^2(1-z)^2 \left[z^2 + (1-z)^2\right] = \int_0^{M^2/4} dk^2\, \frac{k^4}{M^6}\, \frac{1 - 2k^2/M^2}{\sqrt{1 - 4k^2/M^2}}. \tag{4.5}$$

We want to obtain the formula with β and Q^2 as independent variables, thus we have to use the formula:

$$M^2 = \frac{1-\beta}{\beta} Q^2\,. \tag{4.6}$$

Finally, Eq. (4.3) takes the following form

$$x_{I\!P} F_T^{(q\bar{q})} = \frac{3}{64\pi^4 B_d} \sum_f e_f^2\, \frac{\beta^2}{(1-\beta)^3} \int_0^{\frac{Q^2(1-\beta)}{4\beta}} dk^2\, \frac{1 - \frac{2\beta}{1-\beta}\frac{k^2}{Q^2}}{\sqrt{1 - \frac{4\beta}{1-\beta}\frac{k^2}{Q^2}}}\, \phi_1^2(x_{I\!P}, \beta, k), \tag{4.7}$$

where

$$\phi_1(x_{I\!P}, \beta, k) = k^2 \int_0^\infty dr\, r\, K_1\left(\sqrt{\frac{\beta}{1-\beta}} kr\right) J_1(kr)\, \hat{\sigma}(x_{I\!P}, r)\,. \tag{4.8}$$

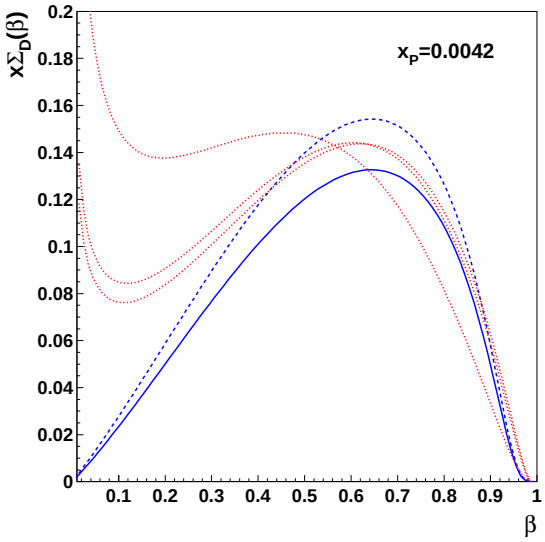

Figure 4.2: Diffractive singlet quark distribution $x\Sigma_D(x_{I\!P}, \beta)$ as a function of β for $x_{I\!P} = 0.0042$ and two parametrizations of the dipole scattering amplitude: GBW (solid line) i CGC (dashed line). Here $x = x_{I\!P}\beta$. The (dotted lines) show the parton distributions from our DGLAP fit to the H1 data.

The leading behavior in Q^2 of $F_T^{(q\overline{q})}$ for fixed values of β and $x_{I\!P}$ is found after changing the integration limit over k^2 to infinity and neglecting in the integrand the expressions proportional to

$$\frac{\beta}{1-\beta}\frac{k^2}{Q^2} = z(1-z) \ll 1\,. \tag{4.9}$$

Such a limit means that we consider the so called *aligned jet configuration* when the fraction z or $(1-z)$ is very small. Then

$$x_{I\!P}F_T^{(tw2)} = \frac{3}{64\pi^4 B_d}\sum_f e_f^2\,\frac{\beta^2}{(1-\beta)^3}\int_0^\infty dk^2\phi_1^2(x_{I\!P},\beta,k)\,. \tag{4.10}$$

Comparing the resulting formula with Eq. (4.1) we find the *diffractive singlet quark distribution*

$$\Sigma^D(x_{I\!P},\beta) = \frac{3N_f}{64\pi^4 B_d x_{I\!P}}\,\frac{\beta}{(1-\beta)^3}\int_0^\infty dk^2\,\phi_1^2(x_{I\!P},\beta,k)\,. \tag{4.11}$$

This distribution is independent of Q^2 and can be interpreted as the initial distribution for the DGLAP evolution, see Fig. 4.2. The value of the initial scale, however, is not determined in the presented approach.

4.2 Diffractive gluon distribution

As a starting point for the extraction of the diffractive gluon distribution will now serve Eq. (3.20), after reducing it to the collinear factorization form.

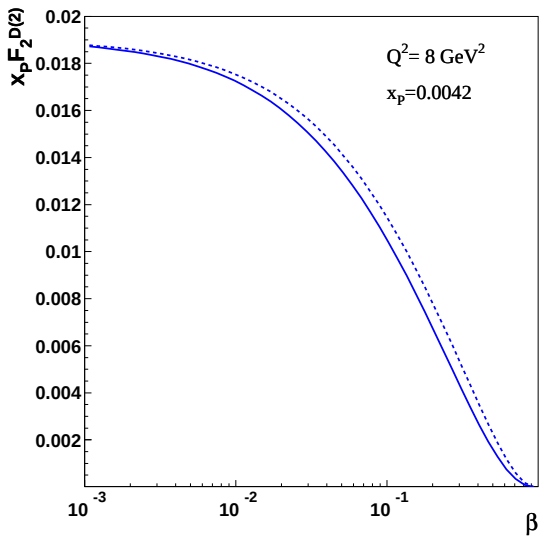

Figure 4.3: The contribution $F_T^{q\overline{q}g}$ as a function of β for two formulas (3.20) (solid line) and (4.13) (dashed line). The effect of the change $(1-z)Q^2 \to Q^2$ in Eq. (3.20) is not significant.

For this purpose, let us compute first the logarithmic derivative of the structure function Eq. (4.1). Using the DGLAP equation for the singlet quark distribution, we have

$$\frac{\partial \Sigma^D(x_{I\!P},\beta,Q^2)}{\partial \ln Q^2} = \frac{\alpha_s(Q^2)}{2\pi}\int_\beta^1 \frac{dz}{z} N_f \left\{\left(1-\frac{\beta}{z}\right)^2 + \left(\frac{\beta}{z}\right)^2\right\} g^D(x_{I\!P},z,Q^2)$$

$$+ \frac{\alpha_s(Q^2)}{2\pi}\int_\beta^1 \frac{dz}{z}\frac{4}{3}\left(\frac{1+(\beta/z)^2}{1-\beta/z}\right)\Sigma^D(x_{I\!P},z,Q^2)\,.$$

For small values of β, when the $q\overline{q}g$ component dominates, the second term in the above Eq., is much smaller than the first one and we find

$$\frac{\partial F_2^D(x_{I\!P},\beta,Q^2)}{\partial \ln Q^2} = \frac{\beta\alpha_s}{2\pi}\sum_f e_f^2 \int_\beta^1 \frac{dz}{z}\left\{\left(1-\frac{\beta}{z}\right)^2 + \left(\frac{\beta}{z}\right)^2\right\} g^D(x_{I\!P},z,Q^2). \tag{4.12}$$

This is the relation between the diffractive gluon distribution and the structure function in the collinear limit for $\beta \to 0$.

Coming back to Eq. (3.20), let us substitute $(1-z)Q^2 \to Q^2$ there to find

$$F_T^{(q\overline{q}g)} = \frac{81\beta\alpha_s}{512\pi^5 B_d x_{I\!P}}\sum_f e_f^2 \int_0^{Q^2} dk^2 \log\left(\frac{Q^2}{k^2}\right)$$

$$\times \int_\beta^1 \frac{dz}{z}\left[\left(1-\frac{\beta}{z}\right)^2 + \left(\frac{\beta}{z}\right)^2\right]\frac{z}{(1-z)^3}\,\phi_2^2(x_{I\!P},z,k)\,. \tag{4.13}$$

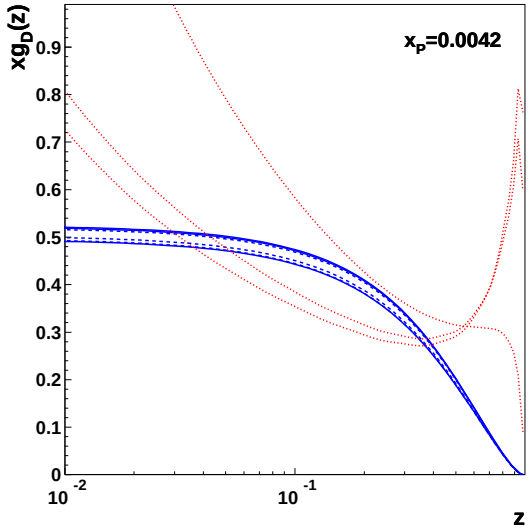

Figure 4.4: Diffractive gluon distribution $xg_D(x_{I\!P}, z, Q^2)$ as a function of z, for $Q^2 = 1.0,\ 4m_c^2,\ 10^2,\ 10^3$ GeV^2 (from bottom to top) and $x_{I\!P} = 0.0042$ for two parametrizations of the dipole scattering amplitude: GBW (solid lines) and CGC (dashed lines). Here $x = x_{I\!P} z$. The (dotted lines) show the parton distributions from our DGLAP fit to the H1 data.

In Figure 4.3 we see that such a change leaves the diffractive structure function practically unchanged. After taking the logarithmic derivative, we find

$$\frac{\partial F_T^{(q\bar{q}g)}}{\partial \ln Q^2} = \frac{81\beta\alpha_s}{512\pi^5 B_d x_{I\!P}} \sum_f e_f^2 \int_\beta^1 \frac{dz}{z} \left[\left(1 - \frac{\beta}{z}\right)^2 + \left(\frac{\beta}{z}\right)^2 \right] \times \frac{z}{(1-z)^3} \int_0^{Q^2} dk^2\, \phi_2^2(x_{I\!P}, z, k)\,. \tag{4.14}$$

For small β we have $F_T^{(q\bar{q}g)} \approx F_2^D$, thus comparing with (4.12) we find the following diffractive gluon distribution

$$g^D(x_{I\!P}, z, Q^2) = \frac{81}{256\pi^4 B_d\, x_{I\!P}} \frac{z}{(1-z)^3} \int_0^{Q^2} dk^2\, \phi_2^2(x_{I\!P}, z, k), \tag{4.15}$$

where

$$\phi_2(x_{I\!P}, z, k) = k^2 \int_0^\infty dr\, r\, K_2\left(\sqrt{\frac{z}{1-z}} kr\right)\, J_2(kr)\, \hat{\sigma}(x_{I\!P}, r)\,. \tag{4.16}$$

The dependence of the gluon distribution Eq. (4.15) on Q^2 has nothing in common with the DGLAP evolution, it can be treated, however, as an initial scale for the evolution. In Fig. 4.4 we show gluon distributions computed for the GBW and CGC parametrization of the dipole scattering amplitude, together with the gluon from DGLAP fit. We see that g^D tends to a bounded asymptotic shapes for dipole approach.

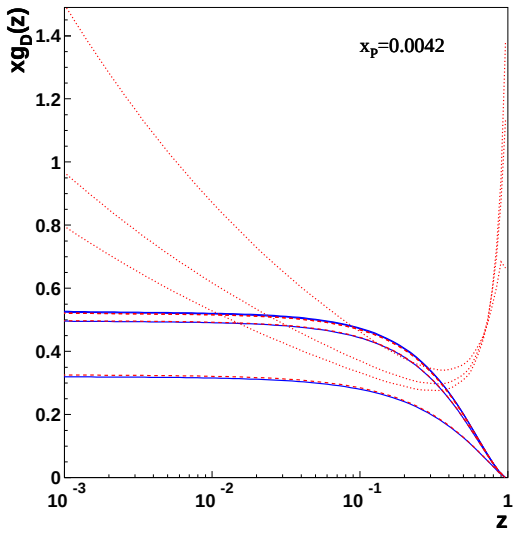

Figure 4.5: The same as in Figure 4.4 but with the color factors absorbed into the GBW dipole cross section as in the CGC approach.

The two gluon distributions from dipole approach in Fig. 4.4 are considerable different. This difference disappears when we consider the approach suggested by the comparison with the HERA data in which the two gluon exchange color factor is absorbed into the dipole cross section in the GBW form, see Eq. (3.23). In the CGC parametrization this is already taken into account. Thus, for the GBW parametrization we rescale Eq. (4.15):

$$g^D \;\to\; \frac{1}{(C_A/C_F)^2}\; g^D, \tag{4.17}$$

and use formula Eq. (3.23) for the dipole cross section. For $N_c = 3$ colors we have $C_A/C_F = 9/4$. The result shown in Fig. 4.5. Now both the GBW and CGC parametrizations give the same diffractive gluon distribution, the lines: solid for GBW and dashed for CGC incrust in Fig. 4.5. Notice that the described above ambiguity in the treatment of the color factors does not concern the interaction of the $q\overline{q}$ diffractive state.

4.3 Heavy flavor production in dipole models

In the dipole models of the diffractive scattering heavy quarks are produced as $c\overline{c}$ and $b\overline{b}$ pairs. From now on we consider only charm production since bottom production is negligible. Such pairs can be produced provided that the mass of the diffractive system is above the quark pair production threshold

$$M^2 = Q^2\,(1/\beta - 1) > 4m_{c,b}^2 \tag{4.18}$$

In the lowest order the diffractive state consist only the $c\overline{c}$ or $b\overline{b}$ pair. The corresponding contributions to F_2^D are given by Eqs. (3.6) and (3.7) with only one flavor component. For example, for the charm pair production from transverse photons, we have

$$x_{I\!P} F_T^{(c\overline{c})} = \frac{3Q^4 e_c^2}{64\pi^4 \beta B_d} \int_{z_c}^{1/2} dz\, z(1-z) \left\{ [z^2 + (1-z)^2]\, Q_c^2\, \phi_1^2 \;+\; m_c^2\, \phi_0^2 \right\} \tag{4.19}$$

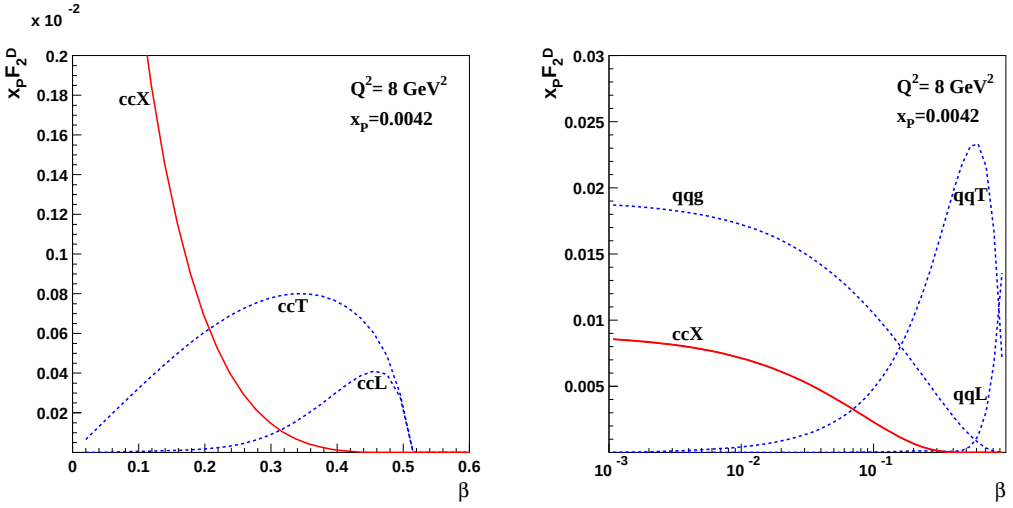

Figure 4.6: On the left: the $c\bar{c}T$ and $c\bar{c}L$ components of F_2^D at $Q^2 = 8$ GeV^2 from the dipole model with the GBW parametrization together with the $c\bar{c}X$ contribution from the collinear approximation Eq. (4.22) with the diffractive gluon distribution Eq. (4.15). On the right: we show the $c\bar{c}X$ component in a different scale against the massless $q\bar{q}T, q\bar{q}L, q\bar{q}g$ components.

where m_c and e_c are the charm quark mass and electric charge, respectively, and

$$z_c = (1 - \sqrt{1 - 4m_c^2/M^2})/2\,, \qquad Q_c^2 = z(1-z)Q^2 + m_c^2\,. \tag{4.20}$$

The minimal value of the diffractive mass $M^2 = 4m_c^2$, thus the maximal value of β is given by

$$\beta_{max} = \frac{Q^2}{(Q^2 + 4m_c^2)}\,. \tag{4.21}$$

In such a case, $z_c = 1/2$ in Eq. (4.19) and $F_{T,L}^{(c\bar{c})} = 0$ for $\beta > \beta_{max}$. This is shown in Fig. 4.6 (left) for the $c\bar{c}$ diffractive states from transverse $(c\bar{c}T)$ and longitudinal $(c\bar{c}L)$ photons. By the comparison with the corresponding curves for three massless quarks $(q\bar{q}T, q\bar{q}L)$, shown in Fig. 4.6 (right), we see that the exclusive $c\bar{c}$ diffractive production contributes only $1/30$ to the total structure function F_2^D and can practically be neglected.

The next component of the heavy quark production is the $c\bar{c}g$ diffractive state. Unfortunately, formula (3.20) for the $q\bar{q}g$ production is only known for massless quarks and cannot be used for heavy quarks. Thus, we have to resort to the collinear factorization formula Eq. (4.22), in which the heavy quark pair is produced via the photon-gluon fusion: $\gamma^* g \to c\bar{c}$ [101]. If such an approach is applied to diffractive scattering, gluon is a *constituent of a pomeron*. Thus in addition to the heavy quark pair, the diffractive state (or system) also consists of additional particles X called (*pomeron remnant*) which are well separated in rapidity from the scattered initial proton. The diffractive case with pomeron remnant was discussed in detail in Section 1.3 and is shown in Fig. 1.6.

In the collinear factorization approach, the leading order formula for the diffractive structure function $F_2^{D(c\bar{c})}$ with the $c\bar{c}X$ diffractive state is the same as in the inclusive case but with the diffractive gluon distribution g^D instead of the inclusive one [73]:

$$F_{2,L}^{D(c\bar{c})}(x_{I\!P}, \beta, Q^2) \;=\; 2\beta\, e_c^2\, \frac{\alpha_s(\mu_c^2)}{2\pi} \int_{a\beta}^{1} \frac{dz}{z}\; C_{2,L}\left(\frac{\beta}{z}, \frac{m_c^2}{Q^2}\right) g^D(x_{I\!P}, z, \mu_c^2) \tag{4.22}$$

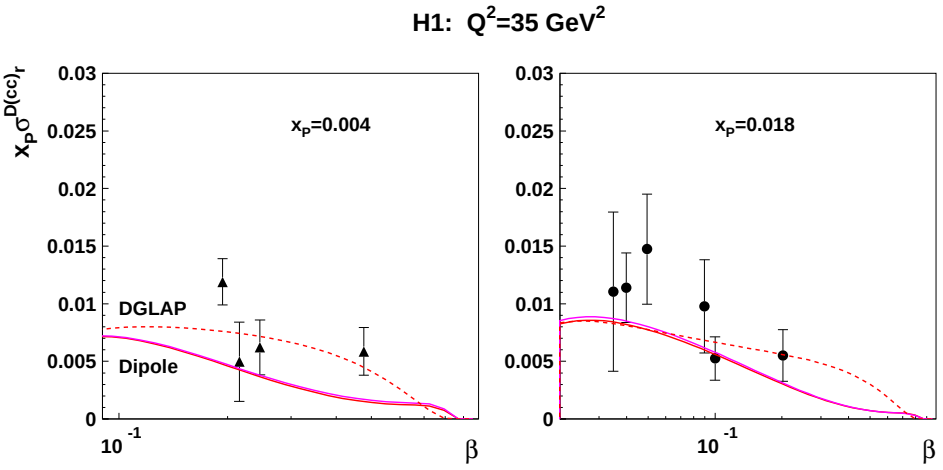

Figure 4.7: The comparison of the collinear factorization predictions with the GBW and CGC gluon distributions (solid lines) with the HERA data on the open diffractive charm production. The dashed lines are computed with the gluon distribution obtained in the DGLAP fit [61] to the H1 data on the diffractive structure functions.

where $a = 1+4m_c^2/Q^2$, and the factorization scale $\mu_c^2 = 4m_c^2$ with charm quark mass $m_c = 1.4\,\mathrm{G}eV$. The leading order coefficient functions $C_{2,L}$ are given by

$$\begin{aligned} C_2(z,r) &= \tfrac{1}{2}\left\{z^2+(1-z)^2+4z(1-3z)r-8z^2r^2\right\}\ln\tfrac{1+\alpha}{1-\alpha} \\ &+ \tfrac{1}{2}\alpha\left\{-1+8z(1-z)-4z(1-z)r\right\} \end{aligned} \tag{4.23}$$

$$C_L(z,r) = -4z^2 r\ln 1+\alpha 1-\alpha+2\alpha z(1-z) \tag{4.24}$$

where $r = m_c^2/Q^2$ and $\alpha = \sqrt{1-4rz/(1-z)}$. The lower integration limit in Eq. (4.22) results from the condition for the heavy quark production in the fusion: $\gamma^* g \to c\bar{c}$,

$$(z x_{I\!P}\, p+q)^2 \geq 4m_c^2 \tag{4.25}$$

where we assume that gluon carries a fraction z of the pomeron momentum $x_{I\!P}p$.

The $c\bar{c}X$ contribution given by Eq. 4.22 and showed in Fig. 4.6 as solid lines becomes significant for $\beta < 0.1$. By a comparison with the massless quark contributions (the right Figure) in Fig. 4.6, we see that diffractive charm production contributes up to 30% to the diffractive structure function F_2^D for small values of β. The presented results were obtained assuming the diffractive gluon distribution which results from the dipole model, given by the Eq. 4.15, with the GBW parametrization of the dipole cross section with the color factor modification. The CGC parametrization gives a similar results.

In Fig. 4.7 we show the collinear factorization predictions for the diffractive charm production confronted with the HERA data [100] on the charm component of the reduced cross section:

$$\sigma_r^{D(c\bar{c})} = F_2^{D(c\bar{c})} - \frac{y^2}{1+(1-y)^2}F_L^{D(c\bar{c})}\,. \tag{4.26}$$

The solid curves, which are barely distinguishable correspond to the result with the GBW and CGC parametrizations of the diffractive gluon distributions. The dashed lines are computed for the gluon

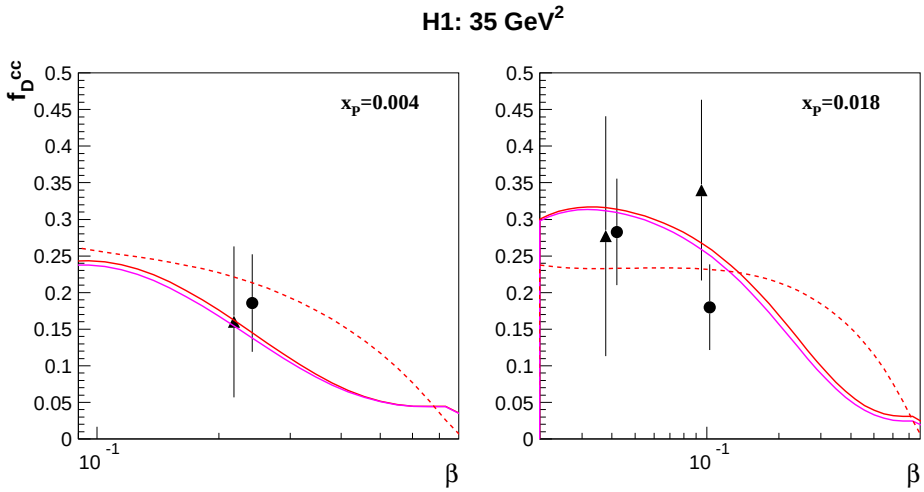

Figure 4.8: The contribution of charm quarks to the total diffractive cross section, $f_D^{c\bar{c}}$, shown as a function of β. The solid lines are the collinear factorization predictions for the $c\bar{c}$ production with the GBW and CGC diffrcative gluon distributions while the dashed lines are computed with the gluon distribution obtained in the DGLAP fit ([61]) to the H1 data.

distribution from the DGLAP fit to the H1 data [61]. The present accuracy of the charm data does not allow one to discriminate between these two approaches although the data seem to prefere the gluon distribution from the DGLAP fit which is much more concentrated in the large z-region as compared to the dipole model gluon distributions, see Fig. 4.4.

In Fig. 4.8 the measurements [100] are presented in the form of fractional contribution of charm to the total diffractive ep cross section, $f_D^{c\bar{c}} = \sigma_r^{D(c\bar{c})}/\sigma_r^D$. For small values of $x = \beta x_{I\!P}$ the charm contribution equals on average approximately $20\% - 30\%$, which is comparable to the charm fraction in the inclusive cross section for similar values of Q^2 [102]. The collinear factorization predictions with the GBW and CGC parametrizations of the diffractive gluon distributions (solid lines) are found to describe the data reasonable. The predictions with the gluon distribution from the DGLAP fit to the H1 data (dashed lines) show also reasonable description of the charm ratio $f_D^{c\bar{c}}$.

In summary, the gluon distributions from the two approaches were used to make predictions for the diffractive charm production. We found that this contribution is significant in both approaches, especially for small values of β. Finally, we found good agreement with the HERA data on the diffractive open charm production both for the gluon distributions from the considered dipole models and the DGLAP fits from [61].

Chapter 5

Diffractive dijet production at the Tevatron

Hard diffractive processes in hadron-hadron collisions, such as the diffractive production of dijets or massive electroweak bosons, are especially interesting since they allow to study the interplay of small and large distance QCD dynamics. The existence of a hard scale (E_T of jets of electroweak boson mass) justifies the use of perturbative QCD. On the other hand, the mechanism of the rapidity gap formation is nonperturbative since no hard scale is involved on the intact hadron side. As it was shown in the previous chapters, the description of this aspect of hard diffractive processes in deep inelastic scattering (DDIS) with the help of the diffractive parton distributions turned out very successful. It is, therefore, tempting to apply them to the hard diffractive processes in hadronic collisions invoking the QCD factorization theorem which allows to separate soft and hard aspects in a process independent way.

However, in diffractive hadron-hadron scattering, QCD factorization is violated due to soft interactions between colliding hadrons and therefore, the diffractive parton distributions extracted from DDIS cannot be used to predict cross sections of hard diffractive processes in $p\overline{p}$ or pp collisions. A large discrepancy is observed in a shape and normalization between H1 and ZEUS predictions and CDF data on dijet production, by which factorization breaking is clearly shown. A quantity which describes the scale of the QCD factorization breaking in hard diffraction at hadron colliders is called the gap survival probability which is a probability that there is no additional soft interactions which destroy the gap, i.e. that hard scattering events remain diffractive.

The main goal in this chapter is to reanalyze the QCD factorization breaking in diffractive dijet production at the Tevatron with our parton distributions found in Chapter 2. We will also pay an attention to the role of the secondary reggeon contribution the scale of the factorization breaking. We will show that this aspect, usually omitted in the discussions up till now, is an important factor for the Tevatron data analysis.

5.1 Diffraction at the Tevatron

After the gluon and quark densities in the pomeron have been find, it is easy to formulate predictions for the Tevatron (or the LHC) on the condition that the same mechanism is assumed for the origin of diffraction in each case. It is thought that the same structures of the pomeron exist at HERA and the Tevatron. An example is the jet production in single diffraction or double pomeron exchange using the parton densities in the pomeron measured at HERA. Here we present jet production in single diffraction at the Tevatron [103]. The interesting point is to see if the factorization property between HERA and Tevatron, using the same parton distributions functions, holds or not [104–106].

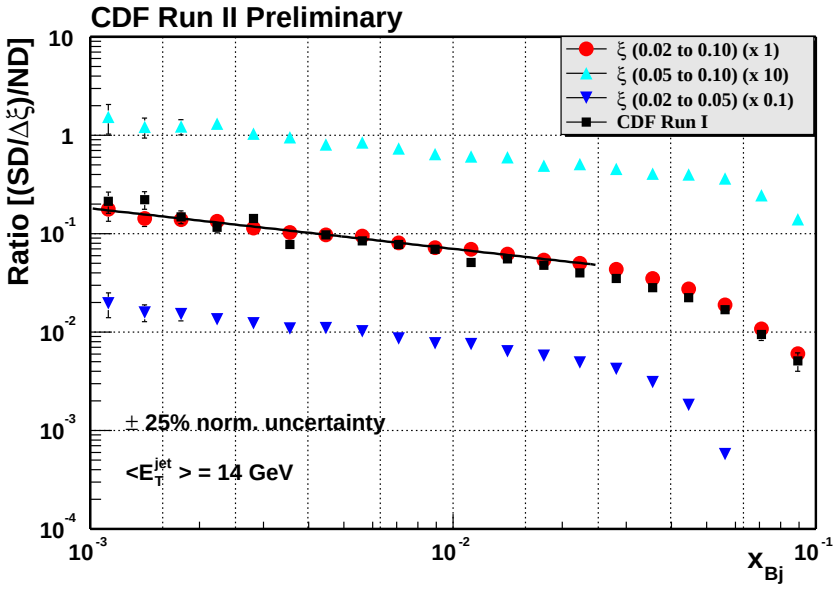

Figure 5.1: Test of QCD factorization within CDF diffractive data alone. The percentage of diffractive events with dijets is presented as a function of x for different ξ bins. The same x-dependence is observed within systematic and statistical uncertainties in all ξ bins, supporting the fact that CDF data are consistent with factorization [104].

The diffractive processes at the Tevatron are presented and briefly discussed in Chapter 1. According to the theory, QCD factorization is not expected to hold between the Tevatron and HERA [107] due to additional soft interactions between colliding hadrons. For instance, soft gluon exchanges between protons are possible at a time scale longer than for hard interactions. The rapidity gap is destroyed by such exchanges and the proton does not remain intact after the interaction. The factorization break-up is confirmed first by comparing the percentage of diffractive events at HERA and the Tevatron (10% at HERA and about 1% of single diffractive events at the Tevatron) showing already that factorization does not take place [6]. So it is necessary to introduced the concept of gap survival probability, the probability that there is no soft additional interaction or that the event remains diffractive, which we briefly discuss in Section 1.9.

The first experimental test of QCD factorization is applied to CDF data on dijet production only. In Fig. 5.1, the percentage of diffractive events as a function of x for different $\xi(= x_{I\!P})$ bins is shown, as well as the same x-dependence within systematic and statistical uncertainties in all ξ bins, supporting the fact that CDF data are consistent with factorization [104]. The x-dependence for different mean $\langle E_T \rangle$ bins, which leads to the same conclusions, was also studied by the CDF Collaboration.

As a second step, it is checked, whether factorization between Tevatron and HERA data takes place. It is possible to measure the diffractive structure function directly at the Tevatron. What is measured, is the ratio of dijet events in single diffractive and non-diffractive events, which is directly proportional to the ratio of the diffractive to the proton structure functions F_2,

$$R(x) = \frac{\mathrm{Rate}_{jj}^{SD}(x)}{\mathrm{Rate}_{jj}^{ND}(x)} \sim \frac{F_{jj}^{SD}(x)}{F_{jj}^{ND}(x)} \,. \tag{5.1}$$

F_2 is known from the DIS experiments on fixed targets and from HERA, thus single diffractive dijet structure function $F_{jj}^{SD}(x)$ is directly determined by measuring the ratio $R(x)$.

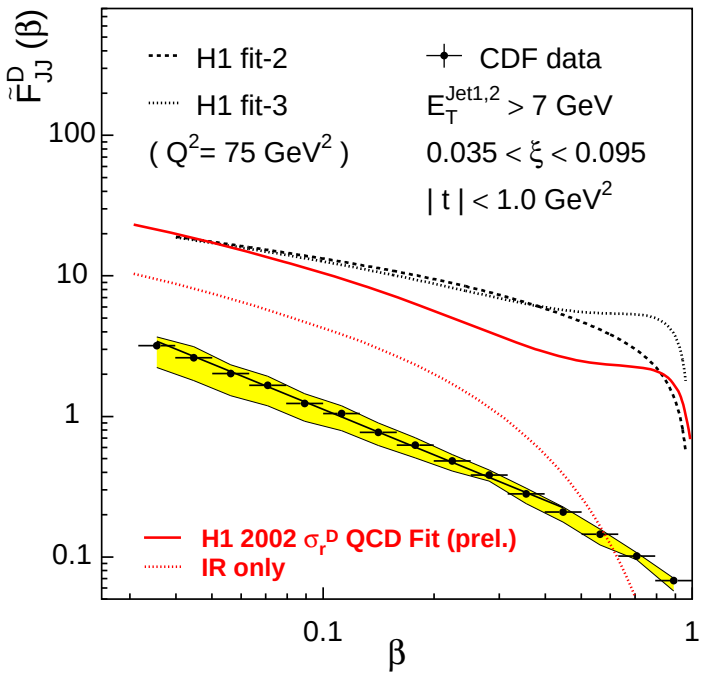

Figure 5.2: Comparison between the CDF measurement of diffractive structure function (black points) with the expectation of the H1 QCD fits (red full line) from [106].

As it is seen in Figure 5.2, the predictions which use diffractive parton distributions from the H1 Collaboration fits to DDIS data from HERA significantly (a factor 8 to 10) overshoot the experimental points from the CDF measurement. Therefore, the QCD factorization is clearly violated which can be attributed to soft interactions between the colliding hadrons. At least two interesting questions are in order at this point. First, it is the role of the secondary reggeon exchanges. As we see in Figure 5.2, they contribute up to 50% to the violation of the QCD factorization. Secondly, looking at the shape in β, it is interesting to ask about the β-dependence of the gap survival probability which brings the predictions into the agreement with the CDF data.

5.1.1 Basic formula for diffractive dijet structure function at Tevatron

Before discussing the QCD factorization breaking in the CDF dijet data we will present basic formula for the measured quantity. If we ignore rescattering corrections, then the cross section for diffractive dijet production, shown in Figure 5.3 (a), may be written as

$$\frac{d\sigma}{dE_T d\beta} = \sum_{i,k} \int f_{I\!P}(\xi,t)\, f_i^{I\!P}(\beta,E_T^2)\, f_k^p(x_1,E_T^2)\, \hat{\sigma}_{ik}\, dx_1\, d\xi\, dt \tag{5.2}$$

where $\hat{\sigma}_{i,k}$ is the hard cross section to produce dijets from partons i,k which carry longitudinal momentum fractions of the proton and pomeron, x_1 and β, respectively. Information on the diffractive structure functions $f_i^P(\beta,E_T^2)$ are obtained from the measurements of the diffractive processes at HERA, shown in Fig. 5.3 (b). The pomeron flux factor $f_{I\!P}(\xi,t)$ is given by Eq. (2.8) and $f_k^p(x_1,E_T^2)$ are the standard parton distribution functions in the proton.

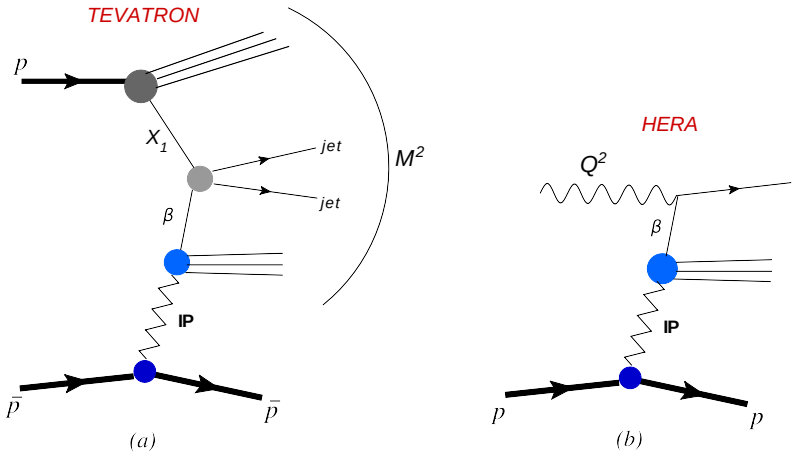

Figure 5.3: Schematic diagrams for diffractive dijet production at the Tevatron (a) and the diffractive deep inelastic scattering at HERA (b).

The CDF Collaboration present measurements of the ratio of the dijet production with a rapidity gap to that without a gap as a function of $x = \beta\xi$ (the fractional longitudinal momentum of the antiproton carried by the parton) for $E_T(\mathrm{jet1}, \mathrm{jet2}) > 7$ GeV in the range $0.035 < \xi < 0.095$ and $|t| < 1$ GeV^2. In the ratio, the terms $f_k^p(x_1, E_T^2)\,\hat{\sigma}_{ik}$ cancel. Hence the data determine the diffractive structure function of the antiproton (integrated over t), introduced already in Chapter 1 by Eq. (1.52),

$$F_{jj}^D(\beta) = \frac{1}{x_{I\!P max} - x_{I\!P min}} \int_{x_{I\!P min}}^{x_{I\!P max}} dx_{I\!P}\, f_{I\!P}(x_{I\!P})\, \beta \left\{ g^{I\!P}(\beta, E_T^2) + \frac{4}{9}\, \Sigma^{I\!P}(\beta, E_T^2) \right\}$$

$$+ \quad \text{secondary Reggeon contributions} \tag{5.3}$$

where $x_{I\!P} = \xi$. The secondary reggeon contribution is described by an analogous formula with the reggeon flux given e.g. by Eq. (2.13). The reggeon structure function can be given by Eq. (2.17) or, as in the H1 Collaboration analysis, by the pion parton distribution functions. The reggeon contribution was added to the formula to F_{jj}^D because the CDF measurement was performed in the region of ξ where this contribution might be important.

5.2 Discussion of the QCD factorization breaking at Tevatron

From a fundamental point of view, it is natural that diffractive hard scattering factorization does not apply to hadron-hadron collisions. Attempts to establish corresponding factorization theorems fail because of additional interactions between spectator partons of the colliding hadrons. The contribution of these interactions to the cross section does not decrease with the hard scale and they are generally soft. Thus, we need to rely on phenomenological models to quantify their effects. The yield of diffractive events in hadron-hadron collisions is then lowered because of these soft interactions between spectator partons (often referred to as reinteractions or multiple scatterings). What can be produced are additional final state particles with which the would be rapidity gap is filled. When such additional particles are produced, a very fast proton can no longer appear in the final state because of energy conservation. Diffractive factorization breaking is thus intimately related to multiple scattering in hadron-hadron collisions. It is not a surprise that such scatterings occur since both the colliding hadronic particles are composite objects with large transverse size.

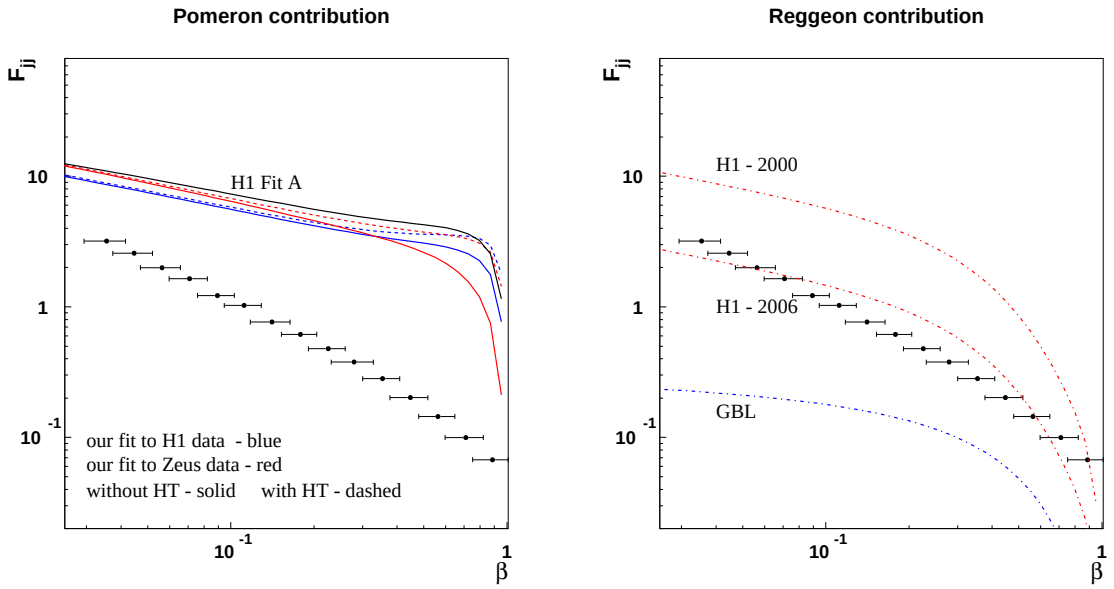

Figure 5.4: Left: a comparison of the measured CDF dijet diffractive distribution as a function of β at $Q^2 = \langle E_T^2 \rangle = 75\ \mathrm{GeV}^2$ with different predictions for the pomeron part of Eq. (5.3). Right: different models of the reggeon contribution, described in the text, shown against the same data.

In Fig. 5.4 (left) we compare the results from our fits with Chapter 2 to the recent CDF single diffractive dijet cross section measurement. In addition, we also show the result from the H1 Collaboration fits (Fit A) [7]. In general, the predictions are already in a reasonable agreement (including the H1 fit without the higher twist contribution) at the evolution scale $Q^2 = 75\ \mathrm{GeV}^2$. As expected, the high beta region shows the biggest differences between the curves. Surprisingly, the H1 fit curve is close to our results with the higher twist contribution. All in all, we note a large discrepancy both in shape and in the normalization between HERA predictions (with and without higher twist) and CDF data, clearly showing factorization breaking.

Precise determination of the scale of the factorization breaking needs to consider the role of the secondary reggeon exchanges which might be important in the region in which CDF measures dijets, $\xi > 0.035$. The answer to this question, however, is far from being clear. The original CDF analysis [103] quotes the parameters from the H1 analysis of the HERA diffractive data from 2000 which lead to the curve denoted by H1-2000 in Figure 5.4 (right). Thus, the reggeon contribution seems to be as important as the pomeron one and the sum of the two contributions gives the red solid curve in Figure 5.2. The new H1 analysis of the HERA data from 2006 [7] leads to new parameters of the reggeon contribution, shown by the curve in the middle denoted as H1-2006, which is three times smaller than the previous one. To make matters worse, our analysis from Chapter 2 gives even smaller contribution (denoted by GBL) which is significantly smaller than the two previous ones. Thus, in our case it can be practically neglected for the dijet production in the kinematic region measured by CDF. Taking into account these results we produce the final plot showing the spread of predictions for the pomeron plus reggeon contribution, see Fig. 5.5. For the H1 Fit A curve, the reggeon contribution was taken from the year 2000 analysis.

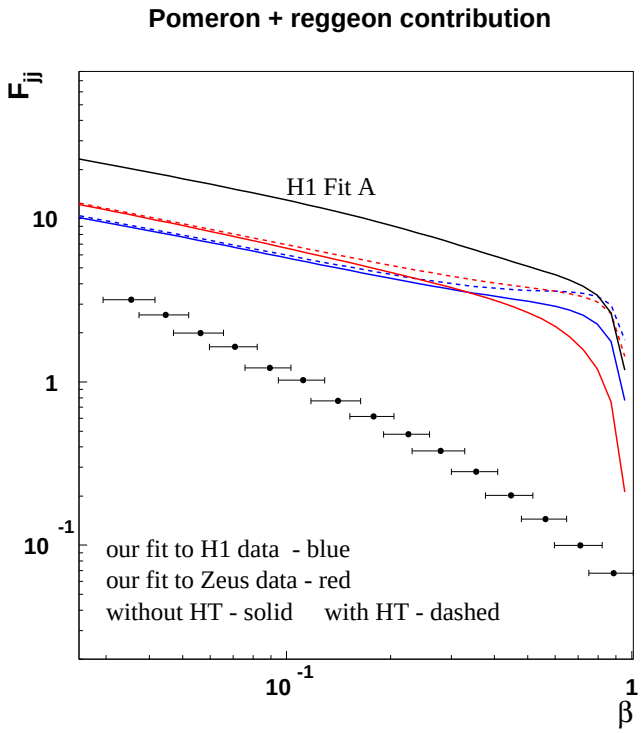

Figure 5.5: The same as in Fig. 5.4 but for the pomeron+reggeon contribution.

5.2.1 Restoring factorization at the Tevatron

The other interesting measurement which was also performed at the Tevatron is the test of factorization between single diffraction and double pomeron exchange. Whereas factorization was not true for the ratio of single diffraction to non diffractive events, factorization takes place for the ratio of double pomeron exchange to single diffraction. In other words, the price to pay for one gap is the same as the price to pay for two gaps [108]. The survival probability, i.e. the probability not to emit an additional soft gluon after the hard interaction needs to be applied only once to require the existence of a diffractive event, but should not be applied again for double pomeron exchange.

To summarize, factorization does not occur between HERA and Tevatron because of the long term additional soft exchanges between spectators in the colling hadrons. Nevertheless, experimentally, factorization happens in case of CDF data themselves and also between single diffraction and double pomeron exchange which means that the soft exchanges do not depend on hard scattering.

5.2.2 Gap survival probability

Let us come back to the term *gap survival probability* (GSP) introduced in Subsection 1.9 and mentioned at the beginning of this Chapter. It is perhaps more accurate to use the term *suppression factor* of a hard process accompanied by a rapidity gap, rather than survival probability. It depends not only on the probability of the initial state to survive, but is sensitive to the spatial distribution of partons inside the incoming hadrons, and thus on the dynamics of the whole diffractive part of the scattering matrix.

In Fig. 5.6 we show the gap survival probability in the diffractive dijet production, calculated in

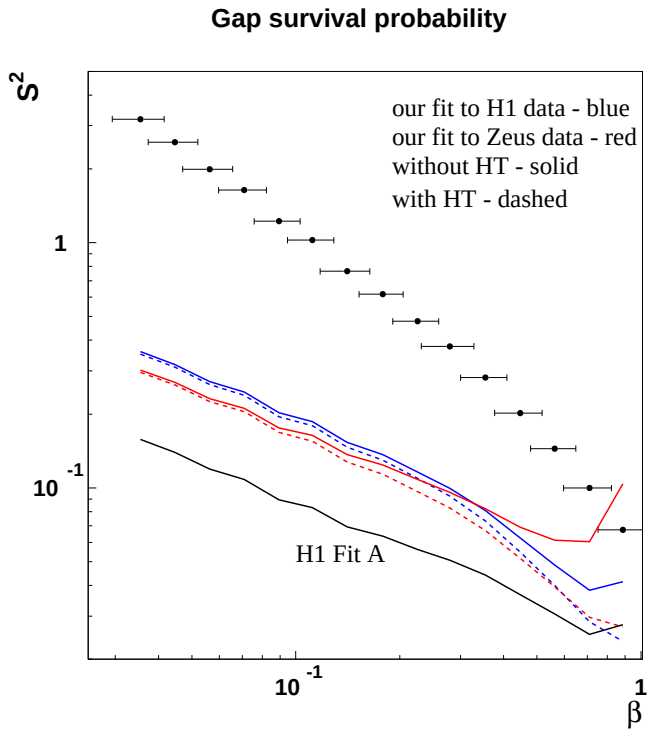

Figure 5.6: The gap survival probability as a function of β for the predictions from Fig. 5.4 (left) with reggeon contribution included.

the following way

$$S^2 = \frac{F_{jj}^{(Exp)}}{F_{jj}^{(Theory)}} \tag{5.4}$$

We compute S^2 as a function of β for all curves in Fig. 5.5 with the reggeon contribution included. The results are shown in Fig. 5.6 (together with experimental points for F_{jj} for better orientation). The GSP is in the range $[0.03, 0.4]$ with strong uncertainty coming from both theoretical and experimental analyzes. As expected, the region of large values of β is most poorly constrained.

5.3 Factorization breaking in dijet photoproduction at HERA

The virtual photon in $\gamma^* p$ collisions has small transverse size, which disfavors multiple interactions and enables diffractive factorization to hold. It may be expect that for decreasing virtuality Q^2, the photon behaves more and more like a hadron, and diffractive factorization may again be broken [108]. That is why, it is appropriate to address the factorization breaking problem in diffractive dijet photoproduction at HERA. The relevant diagrams for this process are shown on Fig. 5.7.

H1 Collaboration [109] has measured diffractive photoproduction of dijets in the kinematic region $Q^2 < 0.01$ GeV^2 with transverse energy cuts of the two jets: $E_T^{jet1} > 5$ GeV and $E_T^{jet2} > 4$ GeV. A fit to the photoproduction data yields suppression factors of 0.53 ± 0.14, independent of the observed x_γ, which is a fraction of the photon momentum transferred into the dijet system. So, the predicted dijet cross section has to be multiplied by a factor of approximately 0.5 for both direct and resolved photon interactions to describe the measurements. The ratio of measured dijet cross section to NLO

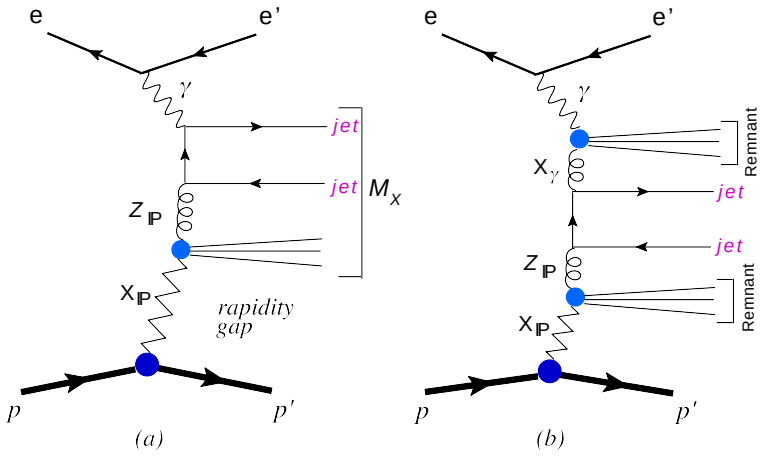

Figure 5.7: Diffractive dijet production at HERA: a) the direct process where the photon enters the hard scatter itself, b) the resolved photon process where only a reduced fraction x_γ of the photon momentum takes part in the hard scatter.

prediction in photoproduction is a factor 0.5 ± 0.1 smaller than the same ratio in DIS. This suppression is the first clear observation of QCD hard scattering factorization breaking at HERA.

For ZEUS Collaboration [110], the measurements of diffractive photoproduction of dijets were performed in the kinematic region $Q^2 < 1$ GeV^2 with higher cuts on jets transverse energy, $E_T^{jet1} > 7.5$ GeV and $E_T^{jet2} > 6.5$ GeV. The comparisons with NLO QCD predictions based on available parametrizations of diffractive PDFs, were made for the full data sample as well as for the subsamples enriched with resolved photon ($x_\gamma^{obs} < 0.75$) and direct photon ($x_\gamma^{obs} \geqslant 0.75$) processes. The NLO calculations tend to overestimate the measured cross sections of both the resolved-enriched and the direct-enriched data sample. However, within large uncertainties of the NLO calculations the data are compatible with QCD factorization.

The theoretical understanding of this discrepancy has not been know yet. Lately, it was addressed in [111] where the gap survival probability was estimated to be:

- for the direct photon contribution $S^2 = 1$,
- for the hadron-like component (resolved photon) $S^2 \simeq 0.34$,
- for the point-like component of the resolved photon generated by the inhomogeneous term in the DGALP equations S^2 has a power-correction form

$$S^2 \simeq \frac{1-a}{\mu^2} + ..., \tag{5.5}$$

  which will only be non-negligible at the beginning of the evolution at low scales μ^2.

Considering these three contributions and other effects, like x_γ migration in the hadronization process, the authors of [111] conclude that for small x_γ the hadron-like component of the resolved photon (with $S^2 \simeq 0.34$) only starts to be important. The perturbatively calculable point-like component of the resolved photon is the dominant one for $x_\gamma > 0.1$, and its suppression is small. For this component, the spectator partons have relatively large transverse momenta and can be seen as a third jet. According to [111], after including the direct component as well, the predictions are consistent with the observed data. It remains to be seen if these conclusions will hold after a careful, independent examination.

Chapter 6

Production of electroweak bosons

The electroweak W and Z boson production in hadronic collision is a particularly valuable process to constrain parton distribution functions (PDFs) in a nucleon. By measuring leptonic products of the weak boson decays, the electroweak parameters like $\sin^2\theta_W$, where θ_W is the effective weak mixing angle, or the W/Z boson masses and decay widths can also be determined. At the Born level, the W/Z bosons are produced from the annihilation of two quarks in the colliding nucleons. In the collinear approximation, the elementary cross sections for these processes have to be convoluted with the nucleons' PDFs. A direct access to these distributions is provided by the measurement of $W^{\pm}$ production asymmetry in rapidity. This quantity reflects the fact that at given rapidity the two charged vector bosons are produced by quarks which are associated with different parton distribution functions. The measured $W^{\pm}$ asymmetry can be used in the global fit analysis to constrain PDFs, in particular the ratio of the u and d PDFs. Such measurements were done at the Fermilab Tevatron. The electron charge asymmetry in W boson decays is presented in [112, 113], a direct measurement of the $W^{\pm}$ boson asymmetry is reported in [114], the forward-backward asymmetry of the electron from Z boson decays is discussed in [115,116], while a short summary on the W/Z boson production at the Tevatron can be found in [117].

In this chapter we analyze inclusive and diffractive weak boson production in pp and $p\bar{p}$ collisions. We begin by discussing the production cross section for $W^{\pm}$ and Z bosons. In the following sections, we present basic formulas for $W^{\pm}$ boson production asymmetry in rapidity for inclusive $p\bar{p}$ and pp collisions. Then, we describe diffractive hadroproduction of W/Z bosons and give predictions for the single diffractive boson production cross sections at the LHC. We discuss in detail the $W^{\pm}$ asymmetry in $p\mathbb{P}$ collisions showing that this quantity is a good observable to test the concept of the flavor symmetric pomeron parton distributions.

The results presented in Section 6.2 are based on the original publication [118].

6.1 Production cross sections

The discovery in 1983 the W and Z gauge bosons at CERN $p\overline{p}$ collider [119, 120] provided dramatic confirmation of Standard Electroweak Model. In the naive parton model, the cross section σ_{AB} for producting such a pair in the collision of beam A and target B is obtained by simply weighting the subprocess cross section $\hat{\sigma}$ for $q\overline{q}' \to W/Z$ with the parton distribution functions $f_q(x)$ and $f_{\bar{q}'}(x)$ extracted from deep inelastic scattering, and summing over all quark-antiquark combinations in the beam and target:

$$\sigma_{AB} = \sum_{q,\bar{q}'} \int dx_1 dx_2 \, f_q(x_1) \, f_{\bar{q}'}(x_2) \, \hat{\sigma}_{q\overline{q}' \to W/Z} \, . \tag{6.1}$$

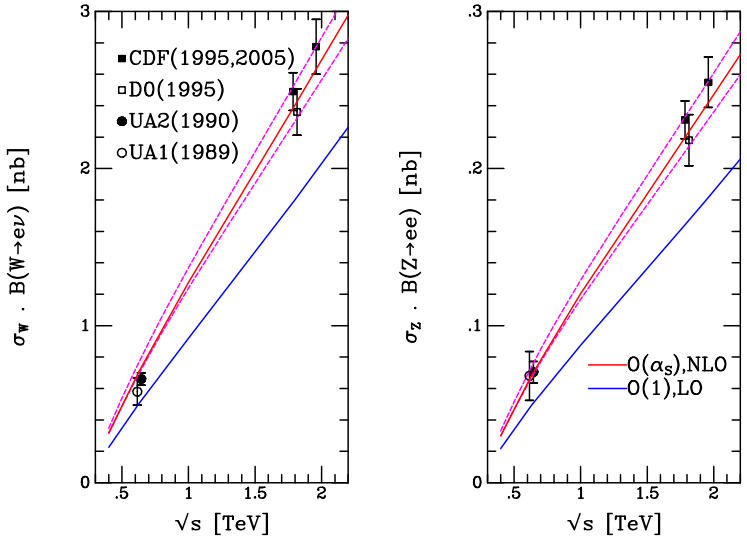

Figure 6.1: Comparison of W and Z cross section measurements in $p\overline{p}$ collisions with theoretical predictions [121].

The leading order cross sections for the subprocess $q\overline{q}' \to W, Z$, with *collinear quarks*, are given by [121]:

$$\sigma^{q\overline{q}'\to W} = \frac{2\pi G_F}{3\sqrt{2}} M_W^2 |V_{ff'}|^2 \delta(\hat{s} - M_W^2) \tag{6.2}$$

$$\sigma^{q\overline{q}\to Z} = \frac{2\pi G_F}{3\sqrt{2}} M_Z^2 (V_f^2 + A_f^2) \delta(\hat{s} - M_Z^2)\,, \tag{6.3}$$

where G_F is the Fermi constant and $V_{ff'}$ is the appropriate CKM matrix element. In addition, $V_f = T_f^3 - 2Q_f \sin^2\theta_W$ and $A_f = T_f^3$ are the vector and axial couplings of the fermion f to the Z boson, respectively, where $T_f^3 = \pm\frac{1}{2}$ with $(+)$ for the up type quarks and $(-)$ for the down type quarks and Q_f is given in units of the positron electric charge $e = g_w \sin\theta_W$.

The W and Z decay widths are small ($\Gamma_W = 2.08$ GeV and $\Gamma_Z = 2.50$ GeV in the Standard Model) compared to their masses, and so it is sufficient to consider the production of effectively stable particles, multiplying cross section by the appropriate final-state branching ratios. Fig. 6.1 shows the $O(\alpha_s)$ theoretical predictions for the W and Z cross sections (multiplied by the Standard Model leptonic branching ratios $BR(W \to l\nu) = 0.1084$ and $BR(Z \to l^+l^-) = 0.0336$) compared with measurements from the $p\overline{p}$ collider experiments [122–125].[2] The parton distributions are the MRS(A') set [126], with the factorization and renormalization scales $\mu_F = \mu_R = M_{W,Z}$. A $\pm 5\%$ theoretical error band on the predictions is included to allow for the uncertainties arising from the parton distributions, electroweak parameters, scale variation and unknown higher-order corrections.

In the calculation of the branching ratio for $W \to l\nu$ used in the theoretical predictions shown in Fig.6.1, the Standard Model prediction for the total W decay width is used. However the comparison between theory and data in Fig. 6.1 can also be used to obtain a measurement of Γ_W. Indeed before the top quark was discovered, this method was used to set limits on a possible $\Gamma(W \to tb)$ contribution to Γ_W, and hence on m_t [127, 128]. It is advantageous to consider the ratio R of the cross sections times branching ratios shown in 6.1. Several uncertainties, for example the uncertainty in the collider

[2] The dominant $W, Z \to q\overline{q}$ decay channels are suppressed by the large QCD two-jet background [121].

luminosity, cancel in the ratio. Thus,

$$R = \frac{N(W \to l\nu_l)}{N(Z \to l^+l^-)} = \frac{\sigma_W}{\sigma_Z} \cdot \frac{N(W \to l\nu)}{N(Z \to l^+l^-)} = R_\sigma \cdot R_{BR} \tag{6.4}$$

$$R_{BR} = \frac{N(W \to l\nu_l)}{N(Z \to l^+l^-)} = \frac{\Gamma(W \to l\nu)}{\Gamma_W} \frac{\Gamma_Z}{\Gamma(Z \to l^+l^-)} \tag{6.5}$$

The cross section ratio R_σ is calculable theoretically. The dependence on parton distributions and on the renormalization and factorization scales is somewhat smaller than for the individual cross sections. The Z leptonic and total widths are measures accurately at LEP and SLC. The partial width, $\Gamma(W \to l\nu_l)$, can be calculated precisely in the Standard Model. Hence, using Eq. 6.5, a measurement of R gives information on Γ_W.

The measured valuse of R from the Tevatron $p\overline{p}$ collider are [125, 129]:

$$R = 10.90 \pm 0.49(stat. \oplus sys.)(D0), \tag{6.6}$$

$$R = 10.9 \pm 0.32(stat.) \pm 0.29(sys.)(CDF), \tag{6.7}$$

which correspond to

$$\Gamma_W = 2.044 \pm 0.092 GeV(D0), \tag{6.8}$$

$$\Gamma_W = 2.064 \pm 0.085 GeV(CDF) \tag{6.9}$$

The theoretical prediction assuming no 'anomalous' decay channels and no $W \to tb$ contribution is a function of the W mass. For $M_W = 80.33 \pm 0.15$ GeV, the prediction is

$$\Gamma_W = 2.085 \pm 0.012 GeV, \tag{6.10}$$

in good agreement with the measured values.

6.2 W bosons production asymmetry in rapidity

The differential cross section for the $W^\pm$ boson production distribution in rapidity y is given by the convolution of the elementary cross section (6.2) with the parton distributions in the colliding nucleons. Thus, in the leading order in α_s we have

$$\frac{d\sigma_{W^\pm}}{dy} = \sigma_0^W \sum_{qq'} |V_{qq'}|^2 \left\{ q(x_1,\mu)\,\overline{q}'(x_2,\mu) \;+\; \overline{q}(x_1,\mu)\,q'(x_2,\mu) \right\}, \tag{6.11}$$

where the factorization scale $\mu = M_W$, $q, \overline{q}$ denote quark/antiquark distributions and

$$\sigma_0^W = \frac{2\pi G_F}{3\sqrt{2}} \frac{M_W^2}{s} \tag{6.12}$$

In addition

$$x_1 = \frac{M_W}{\sqrt{s}} \mathrm{e}^y\,, \qquad\qquad x_2 = \frac{M_W}{\sqrt{s}} \mathrm{e}^{-y} \tag{6.13}$$

are parton longitudinal momentum fractions and y is the W *boson rapidity*. Obviously, $y = \frac{1}{2}\ln(x_1/x_2)$, and from the condition $0 < x_{1,2} < 1$, the following constraint results

$$-y_{max} < y < y_{max} \tag{6.14}$$

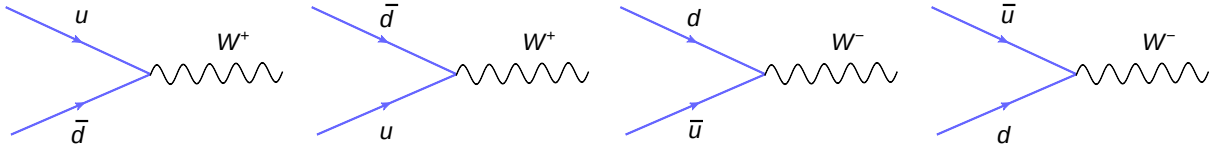

Figure 6.2: The leading order diagrams for the $W^{\pm}$ boson production.

with $y_{max} = \ln(\sqrt{s}/M_W)$. The cross section for the Z boson is obtained from Eq. (6.11), by replacing

$$|V_{qq'}|^2 \;\; \rightarrow \;\; \delta_{qq'}(V_q^2 + A_q^2) \equiv \delta_{qq'} C_q \,. \tag{6.15}$$

In the forthcoming analysis we neglect the Cabbibo suppressed s quark part of the W production cross sections and consider only two flavors: u and d. Thus for the partonic processes shown in Fig. 6.2, we find

$$\frac{d\sigma_{W^+}}{dy} = \sigma_0^W \, |V_{ud}|^2 \left\{ u(x_1)\,\overline{d}(x_2) \, + \, \overline{d}(x_1)\,u(x_2) \right\} \tag{6.16}$$

$$\frac{d\sigma_{W^-}}{dy} = \sigma_0^W \, |V_{ud}|^2 \left\{ d(x_1)\,\overline{u}(x_2) \, + \, \overline{u}(x_1)\,d(x_2) \right\} \tag{6.17}$$

$$\frac{d\sigma_{Z}}{dy} = \sigma_0^Z \, \left\{ C_u \, u(x_1)\,\overline{u}(x_2) \, + \, C_d \, d(x_1)\,\overline{d}(x_2) \, + \, (x_1 \leftrightarrow x_2) \right\} , \tag{6.18}$$

where the parton distributions are taken at the scale $\mu = M_{W,Z}$. The $W^{\pm}$ boson production asymmetry in rapidity is defined as follows

$$A(y) = \frac{d\sigma_{W^+}(y) - d\sigma_{W^-}(y)}{d\sigma_{W^+}(y) + d\sigma_{W^-}(y)} \,. \tag{6.19}$$

6.2.1 $p\bar{p}$ collisions

The predicted distributions for $W^{\pm}$, Z production in $p\overline{p}$ collisions at Tevatron are shown in Fig. 6.3. Here we have defined $y > 0$ to be the direction of the incoming proton. In fact, the W boson rapidity asymmetry provides a very sensitive measure of the relative slope of u and d quark distributions [130]. This fact was our motivation to study electroweak vector bosons asymmetry in diffractive processes, using our diffractive parton distributions from Chapter 2. Assuming that the fraction x_1 refers to the proton and the fraction x_2 refers to the antiproton in the $p\bar{p}$ scattering, the W production cross sections are related to the nucleon parton distributions as follows, see Fig. 6.2

$$\begin{aligned} \frac{d\sigma_{W^+}}{dy} &\sim u_p(x_1)\,\overline{d}_{\overline{p}}(x_2) \, + \, \overline{d}_p(x_1)\,u_{\overline{p}}(x_2) \\ \frac{d\sigma_{W^-}}{dy} &\sim d_p(x_1)\,\overline{u}_{\overline{p}}(x_2) \, + \, \overline{u}_p(x_1)\,d_{\overline{p}}(x_2) \,. \end{aligned} \tag{6.20}$$

Since from charge conjugation symmetry we have

$$d_{\overline{p}}(x) = \overline{d}_p(x) \,, \quad u_{\overline{p}}(x) = \overline{u}_p(x) \quad \text{and} \quad \overline{d}_{\overline{p}}(x) = d_p(x) \,, \quad \overline{u}_{\overline{p}}(x) = u_p(x) \,, \tag{6.21}$$

hence, we find

$$\begin{aligned} \frac{d\sigma_{W^+}}{dy} &\sim u_p(x_1)\,d_p(x_2) \, + \, \overline{d}_p(x_1)\,\overline{u}_p(x_2) \\ \frac{d\sigma_{W^-}}{dy} &\sim d_p(x_1)\,u_p(x_2) \, + \, \overline{u}_p(x_1)\,\overline{d}_p(x_2) \,. \end{aligned} \tag{6.22}$$

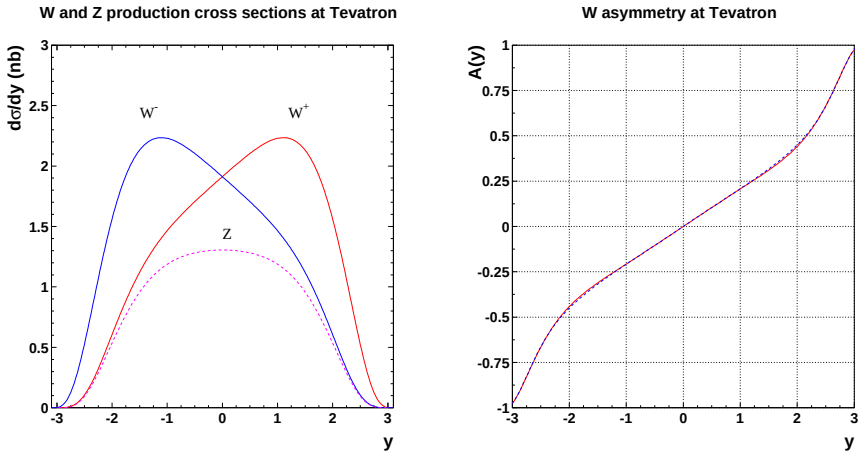

Figure 6.3: Left: the W and Z boson production cross sections at Tevatron as functions of the boson rapidity y for the MSTW08 parton distributions. Right: the W boson asymmetry (solid line) together with the approximate relation (6.28) (dashed line).

Notice that interchanging $x_1 \leftrightarrow x_2$ $(y \to -y)$ we have: $d\sigma_{W^+}/dy \leftrightarrow d\sigma_{W^-}/dy$, and

$$\frac{d\sigma_{W^+}(y)}{dy} = \frac{d\sigma_{W^-}(-y)}{dy}\,. \tag{6.23}$$

This is clearly seen in Fig. 6.3 (left) where the weak boson production cross sections are shown for the proton-antiproton collisions at the Tevatron energy $\sqrt{s} = 1.8$ TeV (in which case $y_{max} \approx 3.1$). We use the LO MSTW08 parametrization [131] of the parton distribution functions. Form relation (6.23), the W boson production asymmetry $A(y)$ is odd function of the W rapidity, see Fig. 6.3.

In the $p\overline{p}$ collisions, the W-charge asymmetry in rapidity is also defined

$$A_{W^+}(y) = \frac{d\sigma_{W^+}(y) - d\sigma_{W^+}(-y)}{d\sigma_{W^+}(y) + d\sigma_{W^+}(-y)}\,. \tag{6.24}$$

Form the above mentioned symmetry, we have the following chain of equalities

$$A_{W^+}(y) = A_{W^-}(-y) = A(y)\,. \tag{6.25}$$

These asymmetries are useful for the determination of the parton distributions since assuming the local isospin symmetry for the sea quarks in the proton

$$\overline{d}_p(x) = \overline{u}_p(x)\,, \tag{6.26}$$

we obtain from relations (6.22)

$$A(y) = \frac{u_p(x_1)\,d_p(x_2) - d_p(x_1)\,u_p(x_2)}{u_p(x_1)\,d_p(x_2) + d_p(x_1)\,u_p(x_2) + 2\,\overline{u}_p(x_1)\,\overline{u}_p(x_2)}\,. \tag{6.27}$$

For most of the parton distribution parametrizations, the term $2\,\overline{u}_p(x_1)\,\overline{u}_p(x_2)$ in the denominator can be neglected and we find

$$A(y) \simeq \frac{u_p(x_1)\,d_p(x_2) - d_p(x_1)\,u_p(x_2)}{u_p(x_1)\,d_p(x_2) + d_p(x_1)\,u_p(x_2)}\,. \tag{6.28}$$

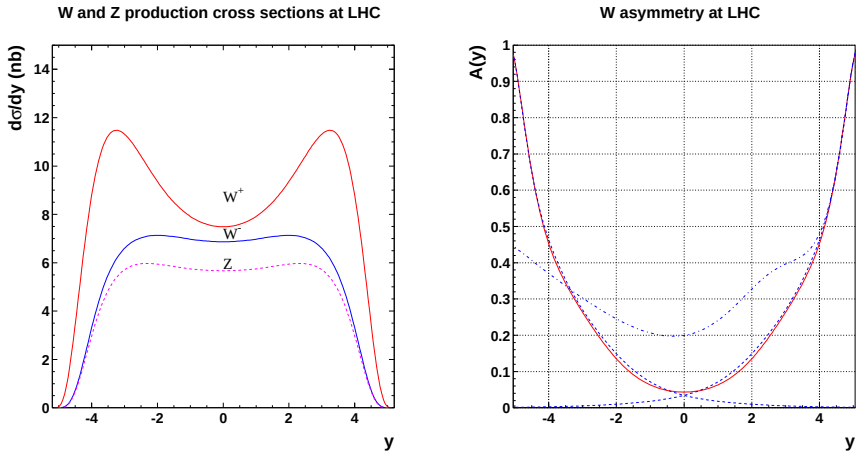

Figure 6.4: Left: the W and Z boson production cross sections at the LHC as functions of the boson rapidity y for the LO MSTW08 parton distributions. Right: the W boson asymmetry (solid curve) together with relation (6.32) computed at $x = x_1$ and $x = x_2$ (two dashed lines) and for the valence quark distributions at $x = x_1$ (dash-dotted line).

The quality of this relation is shown in Fig. 6.3 (right) where the solid curve shows Eq. (6.27) while the dashed curve corresponds to relation (6.28), computed for the LO MSTW08 parametrization.

Relation (6.28) is the basis of the current analysis of the Tevatron data on the W production asymmetry for the determination of the ratio $d_p(x)/u_p(x)$, since from Eq. (6.28) we find

$$\frac{d_p(x_1)/u_p(x_1)}{d_p(x_2)/u_p(x_2)} \simeq \frac{1 - A(y)}{1 + A(y)}\,, \tag{6.29}$$

where the quark distributions are taken at the scale $\mu = M_W$.

6.2.2 pp collisions

For pp collisions, the W production cross sections look as follows

$$\begin{aligned} \frac{d\sigma_{W^+}}{dy} &\sim u_p(x_1)\,\overline{d}_p(x_2) + \overline{d}_p(x_1)\,u_p(x_2) \\ \frac{d\sigma_{W^-}}{dy} &\sim d_p(x_1)\,\overline{u}_p(x_2) + \overline{u}_p(x_1)\,d_p(x_2)\,. \end{aligned} \tag{6.30}$$

Due to symmetric proton beams, the transformation $x_1 \leftrightarrow x_2$ leaves $d\sigma_{W^\pm}$ unchanged, which is reflected in the symmetry of these cross sections under the rapidity reflection $y \to -y$. This is clearly seen in Fig. 6.4 (left) where the cross sections for the LHC energy $\sqrt{s} = 14$ TeV (in which case $y_{max} \approx 5.1$) are shown for the LO MSTW08 parton distributions.

Assuming for simplicity the local isospin symmetry for the sea quark distributions, $\overline{u}_p(x) = \overline{d}_p(x)$, we find

$$A(y) = \frac{(u_p(x_1) - d_p(x_1))\,\overline{u}_p(x_2) + \overline{u}_p(x_1)\,(u_p(x_2) - d_p(x_2))}{(u_p(x_1) + d_p(x_1))\,\overline{u}_p(x_2) + \overline{u}_p(x_1)\,(u_p(x_2) + d_p(x_2))}\,, \tag{6.31}$$

which is evidently even function of rapidity, see Fig. 6.4 (right). In the limit $x_1 \sim 1$ and $x_2 \ll 1$ or $x_1 \sim x_2 \ll 1$, the sea quark distribution $\overline{u}(x_1)$ is small and the second terms in the numerator and

denominator of Eq. (6.31) can be neglected. Thus, we obtain

$$A(y) \simeq \frac{u_p(x_1) - d_p(x_1)}{u_p(x_1) + d_p(x_1)} \,. \tag{6.32}$$

From the $x_1 \leftrightarrow x_2$ symmetry, the same relation holds true when the argument of the parton distributions in Eq. (6.32) is changed to x_2. These approximate relations are shown by the two dashed curves in Fig. 6.4 (right). Thus, from the measurement of the W asymmetry in the pp collisions, the $d_p(x)/u_p(x)$ ratio at the scale $\mu = M_W$ can be extracted,

$$\frac{d_p(x)}{u_p(x)} \simeq \frac{1 - A(y)}{1 + A(y)} \,, \tag{6.33}$$

down to $x_1 \simeq M_W/\sqrt{s} \approx 0.006$ for the LHC energy. Relation (6.32) can also be written in terms of the valence (val) and sea (sea) quark distributions

$$\begin{aligned} u_p(x) &= u_{val}(x) + u_{sea}(x) \,, \qquad & \overline{u}_p(x) &= u_{sea}(x) \\ d_p(x) &= d_{val}(x) + d_{sea}(x) \,, \qquad & \overline{d}_p(x) &= d_{sea}(x) \,, \end{aligned} \tag{6.34}$$

taking the following form (assuming isospin symmetry)

$$A(y) \simeq \frac{u_{val}(x_1) - d_{val}(x_1)}{u_{val}(x_1) + d_{val}(x_1) + (u_{sea}(x_1) + d_{sea}(x_1))} \,. \tag{6.35}$$

For $x_1 \to 1$ the sea quark distributions in the denominator can be neglected and relation (6.33) gives

$$\frac{d_{val}(x)}{u_{val}(x)} \simeq \frac{1 - A(y)}{1 + A(y)} \,. \tag{6.36}$$

The quality of this relation for the LO MRTW09 parametrization is shown in Fig. 6.4 by the dash-dotted line computed from eq. (6.32) with the valence quark distributions at $x = x_1$ (a symmetric curve can be found for $x = x_2$). We see that for $y > 4$ ($x > 0.3$) relation (6.36) can be used for the determination of the d_{val}/u_{val} ratio at the scale $\mu = M_W$.

6.3 Diffractive production of W/Z bosons

Diffractive hadroproduction of electroweak bosons was observed experimentally at the Tevatron [132] and analyzed theoretically in a series of papers [133–136]. Here we concentrate on a single diffractive dissociation case, in which one of the colliding hadrons remains intact while the other which dissociates into the diffractive state is separated in rapidity from the intact hadron, see also Section 1.7 in which we described different types of diffractive processes.

In the diffractive case, the electroweak bosons are produced in a restricted region of rapidity, with a rapidity gap without particles between the proton, which stayed intact and the diffractive system. In this process, the boson mass is a hard scale allowing for perturbative QCD interpretation as in the nondiffractive case. However, the nature of the vacuum quantum number exchange, which leads to the rapidity gap, is nonperturbative. It is usually modelled using the Regge theory notion - a pomeron. In the model of Ingelman and Schlein [21], introduced in Section 2.2, the pomeron is endowed with a partonic structure described by the pomeron parton distributions $q_{I\!P}$, which replace the standard inclusive parton distributions on the dissociated proton side. Since the pomeron carries vacuum quantum numbers, these distributions have to be flavor symmetric

$$u_{I\!P}(x) = \bar{u}_{I\!P}(x) = d_{I\!P}(x) = \bar{d}_{I\!P}(x) = s_{I\!P}(x) = \bar{s}_{I\!P}(x) = \ldots \equiv q_{I\!P}(x) \,, \tag{6.37}$$

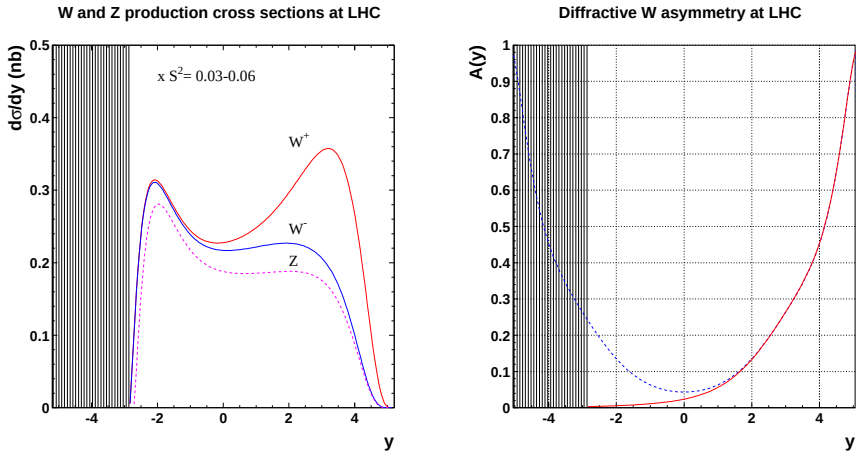

Figure 6.5: Left: the single diffractive W/Z boson production cross sections at the LHC as functions of boson rapidity. The results have to be multiplied by the gap survival factor $S^2 = 0.09$. Right: the W asymmetry in $p\mathbb{P}$ collisions (solid line), given by Eq. (6.42), together with the asymmetry (6.31) in pp collisions (dashed line). The shaded areas indicate the rapidity gap $\Delta = 2.3$ for $x_{\mathbb{P}} = 0.1$.

where $x = x_2/x_{\mathbb{P}}$ and $x_{\mathbb{P}} = M_D^2/s$ is a fraction of the proton's momentum transferred into the diffractive system of mass M_D. With such a definition, x is a fraction of the pomeron momentum carried by the parton taking part in the W boson production. From the condition $0 < x, x_{\mathbb{P}} < 1$, one finds that the W boson rapidity is in the range

$$-y_{max} + \ln(1/x_{\mathbb{P}}) < y < y_{max}\,, \tag{6.38}$$

and the rapidity gap has the length $\Delta = \ln(1/x_{\mathbb{P}})$.

Thus, in the single diffractive case, the W production cross sections are related to quark distributions in the following way

$$\frac{d\sigma_{W^+}}{dy dx_{\mathbb{P}}} \sim (u_p(x_1) + \overline{d}_p(x_1))\, q_{\mathbb{P}}(x_2/x_{\mathbb{P}}) \tag{6.39}$$

$$\frac{d\sigma_{W^-}}{dy dx_{\mathbb{P}}} \sim (d_p(x_1) + \overline{u}_p(x_1))\, q_{\mathbb{P}}(x_2/x_{\mathbb{P}})\,. \tag{6.40}$$

In more general approach, the pomeron parton distribution should be replaced by diffractive parton distributions [54, 55, 62, 64, 69]. As it was described in Chapter 2, in Section 2.2 diffractive parton distributions in the pomeron model interpretation have the Regge factorized form

$$q_D(x_2, x_{\mathbb{P}}) = f(x_{\mathbb{P}})\, q_{\mathbb{P}}(x_2/x_{\mathbb{P}})\,, \tag{6.41}$$

where $f(x_{\mathbb{P}})$ is pomeron flux. Independent of this interpretation, however, the diffractive quark distributions should also be flavor symmetric.

In Fig. 6.5 (left) we show the W and Z production cross sections with the LO MSTW08 proton parton distributions and the pomeron parton distributions from our last analysis [61], presented in Chapter 2. The effect of the pomeron in the left hemisphere is clearly visible - the rapididty gap is formed and the $W^{\pm}$ asymmetry strongly decreases. These cross sections should be multiplied by a gap survival factor, $S^2 = 0.09$ [37], which takes into account soft interactions destroying the rapidity gap.

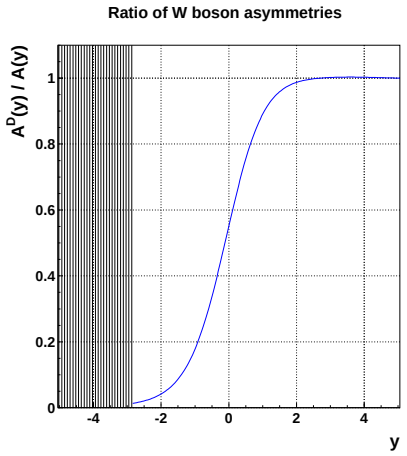

Figure 6.6: The ratio of the W boson production asymmetries in the diffractive and nondiffractive pp scattering.

The W boson production asymmetry (6.19) is a particularly good observable since it is insensitive to the gap survival probability [34] which multiplies both the cross sections $d\sigma_{W^\pm}/dydx_{I\!P}$. The flavor symmetric pomeron parton distributions also cancel, and we obtain for the W asymmetry in the diffractive case,

$$A^D(y) = \frac{u_p(x_1) - d_p(x_1) \, + \, \overline{d}_p(x_1) - \overline{u}_p(x_1)}{u_p(x_1) + d_p(x_1) \, + \, \overline{d}_p(x_1) + \overline{u}_p(x_1)} \,, \tag{6.42}$$

where the parton distributions are taken at the scale $\mu = M_W$. Notice that $A^D(y)$ is independent of $x_{I\!P}$, i.e. the length of the rapidity gap. Substituting decomposition (6.34), we find

$$A^D(y) = \frac{u_{val}(x_1) - d_{val}(x_1)}{u_{val}(x_1) + d_{val}(x_1) \, + \, 2\,(u_{sea}(x_1) + d_{sea}(x_1))} \,. \tag{6.43}$$

This is an exact result obtained only under the assumption (6.37). In Fig. 6.5 (right) we show the asymmetry (6.43) (solid line) together with the W boson asymmetry (6.31) in the inclusive case (dashed line).

In order to understand our result, it is interesting to compare Eq. (6.43) with the approximate asymmetry (6.35), valid in the right hemisphere for $y > 0$. For large rapidities, when the sea quark distributions can be neglected, these two asymmetries are equal while for $y \approx 0$, when the valence quark distributions in the denominator are negligible, $A^D(y) \approx A(y)/2$. This is clearly seen in Fig. 6.6 where the ratio $A^D(y)/A(y)$, with $A(y)$ given by Eq. (6.31), is shown. Approaching the rapidity gap, the asymmetry $A^D(y)$ decreases while $A(y)$ rises. Thus, the ratio shown in Fig. 6.6 is close to zero at the edge of the rapidity gap.

The pattern shown in Fig. 6.6 is quite general and depends only on the assumption on flavor symmetry of the pomeron parton distributions, Eq. (6.37). Therefore, it would be interesting to test experimentally the concept of the flavor symmetric pomeron parton distributions by measuring the ratio of the two W asymmetries in the diffractive and nondiffractive pp scattering. Systematic errors will cancel in such a ratio which should allow for quite precise determination of this quantity. We are looking forward to the experimental verification of the presented results at the LHC.

In summary, the measurement of the $W^\pm$ boson production asymmetry in the diffractive pp collisions is a valuable method to test the concept of the flavor symmetric pomeron parton distributions. If it is true, the W asymmetry in the single diffractive case provides an additional constraint for the parton distribution functions in the proton.

Let us finish by noting that the W rapidity is difficult to measure because of undetected neutrino in the final state from the decay: $W^{\pm} \to l^{\pm}\nu$. It is easier to measure the closely related charge lepton asymmetry, which in general is smaller then that of the W itself. The work in this direction in the diffractive case is underway.

Chapter 7

Summary

In this Thesis we presented theoretical studies of diffractive processes, which have been experimentally investigated in the ep collisions at HERA, $p\overline{p}$ collisions at the Tevatron and will be explored soon in the pp collisions at the LHC. We concentrated on hard diffraction when a large scale is present, allowing for the use of perturbative QCD.

The determination of diffractive parton distributions, documented in Chapter 2, was performed in the framework of the QCD fits to the diffractive data from HERA. In this analysis, we included a higher twist-4 contribution, taken form the dipole models, which dominates for small diffractive masses, $M^2 \ll Q^2$. We proved that this contribution is important for the determination of the diffractive gluon distribution. It also has a big impact on the diffractive longitudinal structure function, F_L^D, for large values of the variable β (small diffractive masses) [137]. The latter result can be compared with measurements when the results from the low energy runs at HERA will be available [80].

In Chapter 3, we analyzed the newest diffractive data from HERA using the dipole model approach with three components of the diffractive state: $q\overline{q}$ and $q\overline{q}g$ from transverse and longitudinal polarized photons. This goes beyond the collinear factorization analysis from Chapter 2 since the energy ($x_{I\!P}$) dependence of the diffractive structure functions can be predicted in the dipole models. On the other hand, the final state diffractive system is better described in the collinear factorization approach since it involves DGLAP resummed parton configurations in the k_T-ordering approximation. In the dipole model approach, we used two most characteristic phenomenological parametrizations of the dipole cross sections (the GBW and CGC parametrizations) which are based on the parton saturation ideas. We discussed the following important elements which have not been analyzed in such detail so far. Firstly, we show that the charm contribution, both in the dipole scattering amplitude and in the diffractive state, is essential for a better description of the data on the diffractive structure function F_2^D measured at HERA (in contrast e.g. to the results of Marquet [75]). Secondly, we proved that a simple model with only quark-antiquark-gluon diffractive state is inadequate to precisely describe the large diffractive mass region and we need DGLAP resummation. Thirdly, we show that the treatment of the color factors in the original GBW approach for quark-antiquark-gluon diffractive component (based on the two gluon exchange approach) fails and should be replaced by that based on eikonal scattering of multiple gluons. To summarize this chapter, we presented an updated and comprehensive analysis which clearly summarizes the significance of the dipole models with parton saturation for the precise description of the recent HERA data. This might be a reference analysis of DDIS for a hopefully new collider LHeC at CERN.

In Chapter 4, we compared two sets of diffractive parton distributions, from the DGLAP fits and from the dipole model approach analyzes. We found significant difference between them, especially for the diffractive gluon distributions. Based on these results, we made predictions for the diffractive charm production using the boson-gluon fusion process, $\gamma^* g \to c\overline{c}$, with the diffractive gluon distribution taken from the two discussed analyzes. We found reasonable agreement with the first HERA data.

We also confirmed the known result that the pure $c\bar{c}$ diffractive production is strongly suppressed due to kinematic limits.

The diffractive parton distributions are not universal and cannot be applied to both lepton-hadron and hadron-hadron diffractive processes. According to [59], additional soft interactions between colliding hadrons prevent the collinear factorization universality of the DPDF. This is seen in diffractive production of dijets at the Tevatron, which we discussed in Chapter 5. We used the DPDF from Chapter 2 to show the scale of the factorization breaking and discuss the role of the secondary reggeon contribution in the description of this effect. We also discussed the gap survival probability for the dijet production. We finished with a brief description of the theoretical status of the factorization breaking in diffractive dijet photoproduction at HERA.

In Chapter 6 we analyzed diffractive hadroproduction of electroweak vector bosons at the LHC. We compared asymmetry in rapidity of the $W^{\pm}$ boson production in inclusive proton-(anti)proton collisions with the same asymmetry expected in the events with single proton diffractive dissociation. Since diffractive dissociation is described by the vacuum quantum number exchange, the pomeron, the expected asymmetry vanishes in the pomeron fragmentation region near the edge of the rapidity gap. This method may be used to test the flavor symmetry of parton distributions in the pomeron and to obtain an additional constraint for the quark distribution functions in the proton.

Acknowledgments

First and foremost, I would like to express my gratitude to my supervisor, Professor Krzysztof Golec-Biernat, who has been supporting my efforts through all the years, starting from forming the concept of this analysis till the preparation of the final version of the presented Thesis. I would like to thank him for invaluable help, guidance and patience.

I am very grateful to my family and my friends for their support during the period of my PhD studies. I thank you all.

I also wish to thank the members of the Department of Structure of Matter for providing nice and comfortable environment for work and study.

This research has been supported by the grants from the Polish Ministry of Science and Higher Education, nos. N N202 246635 and N N202 249235, the grant HEPTOOLS, MRTN-CT-2006-035505 and the European Union Scholarship for Phd students (2009).

Bibliography

[1] UA8, R. Bonino *et al.,* Phys. Lett. **B211**, 239 (1988).

[2] CDF, F. Abe *et al.,* Phys. Rev. Lett. **74**, 855 (1995).

[3] D0, S. Abachi *et al.,* Phys. Rev. Lett. **76**, 734 (1996), [hep-ex/9509013].

[4] ZEUS, M. Derrick *et al.,* Phys. Lett. **B315**, 481 (1993).

[5] H1, T. Ahmed *et al.,* Nucl. Phys. **B429**, 477 (1994).

[6] C. Royon, L. Schoeffel, R. Peschanski and E. Sauvan, Nucl. Phys. **B746**, 15 (2006), [hep-ph/0602228].

[7] H1, A. Aktas *et al.,* Eur. Phys. J. **C48**, 715 (2006), [hep-ex/0606004].

[8] ZEUS, S. Chekanov *et al.,* Nucl. Phys. **B713**, 3 (2005), [hep-ex/0501060].

[9] L. Landau and I. Pomeranchuk, Zh. Eksp. Teor. Fiz. **24**, 505 (1953).

[10] E. Feinberg and I. Pomeranchuk, Nuovo. Cim. Suppl. Fiz. **3**, 652 (1956).

[11] A. Akhiezer and I. Pomeranchuk, Usp. Fiz. Nauk. **65**, 593 (1958).

[12] A. Akhiezer and I. Pomeranchuk, Usp. Fiz. Nauk. **67**, 377 (1959).

[13] V. Barone and E. Predazzi, *High-Energy Particle Diffraction* (Cambridge University Press, 1996).

[14] Born and Wolf, Pergamon Press London. , 397 (1959).

[15] K. Goulianos, Phys. Rept. **101**, 169 (1983).

[16] M. Arneodo and M. Diehl, hep-ph/0511047.

[17] K. Golec-Biernat, Habilitation Thesis, Report No 1877/PH (2001).

[18] M. Wusthoff and A. D. Martin, J. Phys. **G25**, R309 (1999), [hep-ph/9909362].

[19] I. Y. Pomeranchuk, Sov.Phys. **JETP7**, 499 (1958).

[20] A. Donnachie and P. V. Landshoff, Nucl. Phys. **B231**, 189 (1984).

[21] G. Ingelman and P. E. Schlein, Phys. Lett. **B152**, 256 (1985).

[22] G. Altarelli and G. Parisi, Nucl. Phys. **B126**, 298 (1977).

[23] Y. L. Dokshitzer, Sov. Phys. JETP **46**, 641 (1977).

[24] K. J. Golec-Biernat and M. Wusthoff, Phys. Rev. **D60**, 114023 (1999), [hep-ph/9903358].

[25] K. J. Golec-Biernat and M. Wusthoff, Phys. Rev. **D59**, 014017 (1999), [hep-ph/9807513].

[26] J. Bartels and M. G. Ryskin, Z. Phys. **C76**, 241 (1997), [hep-ph/9612226].

[27] M. Wusthoff, Phys. Rev. **D56**, 4311 (1997), [hep-ph/9702201].

[28] K. Goulianos, Phys. Lett. **B358**, 379 (1995), [hep-ph/9502356].

[29] K. Goulianos, hep-ph/9505310.

[30] CDF, A. A. Affolder *et al.*, Phys. Rev. Lett. **87**, 141802 (2001), [hep-ex/0107070].

[31] UA8, A. Brandt *et al.*, Nucl. Phys. **B514**, 3 (1998), [hep-ex/9710004].

[32] D0, S. Abachi *et al.*, Phys. Rev. Lett. **72**, 2332 (1994).

[33] Y. L. Dokshitzer, V. A. Khoze and S. I. Troian, LENINGRAD-86-1218.

[34] J. D. Bjorken, Phys. Rev. **D47**, 101 (1993).

[35] CDF, A. A. Affolder *et al.*, Phys. Rev. Lett. **85**, 4215 (2000).

[36] E. Gotsman, E. M. Levin and U. Maor, Phys. Lett. **B309**, 199 (1993), [hep-ph/9302248].

[37] V. A. Khoze, A. D. Martin and M. G. Ryskin, Eur. Phys. J. **C18**, 167 (2000), [hep-ph/0007359].

[38] V. S. Fadin, E. A. Kuraev and L. N. Lipatov, Phys. Lett. **B60**, 50 (1975).

[39] L. N. Lipatov, Sov. J. Nucl. Phys. **23**, 338 (1976).

[40] E. A. Kuraev, L. N. Lipatov and V. S. Fadin, Sov. Phys. JETP **45**, 199 (1977).

[41] I. I. Balitsky and L. N. Lipatov, Sov. J. Nucl. Phys. **28**, 822 (1978).

[42] J. Bartels, Nucl. Phys. **B151**, 293 (1979).

[43] J. Bartels, Nucl. Phys. **B175**, 365 (1980).

[44] J. Bartels, Phys. Lett. **B298**, 204 (1993).

[45] J. Bartels, Z. Phys. **C60**, 471 (1993).

[46] J. Bartels and M. Wusthoff, Z. Phys. **C66**, 157 (1995).

[47] J. Bartels and C. Ewerz, JHEP **09**, 026 (1999), [hep-ph/9908454].

[48] L. D. McLerran and R. Venugopalan, Phys. Rev. **D49**, 2233 (1994), [hep-ph/9309289].

[49] L. D. McLerran and R. Venugopalan, Phys. Rev. **D49**, 3352 (1994), [hep-ph/9311205].

[50] E. Iancu and R. Venugopalan, hep-ph/0303204.

[51] E. Iancu, hep-ph/0608086.

[52] L. V. Gribov, E. M. Levin and M. G. Ryskin, Phys. Rept. **100**, 1 (1983).

[53] V. N. Gribov and L. N. Lipatov, Sov. J. Nucl. Phys. **15**, 438 (1972).

[54] A. Berera and D. E. Soper, Phys. Rev. **D53**, 6162 (1996), [hep-ph/9509239].

[55] J. C. Collins, Phys. Rev. **D57**, 3051 (1998), [hep-ph/9709499].

[56] F. Hautmann, Z. Kunszt and D. E. Soper, Phys. Rev. Lett. **81**, 3333 (1998), [hep-ph/9806298].

[57] F. Hautmann, Z. Kunszt and D. E. Soper, Nucl. Phys. **B563**, 153 (1999), [hep-ph/9906284].

[58] J. Blumlein, B. Geyer and D. Robaschik, Nucl. Phys. **B755**, 112 (2006), [hep-ph/0605310].

[59] J. C. Collins, L. Frankfurt and M. Strikman, Phys. Lett. **B307**, 161 (1993), [hep-ph/9212212].

[60] K. Golec-Biernat and M. Wusthoff, Eur. Phys. J. **C20**, 313 (2001), [hep-ph/0102093].

[61] K. J. Golec-Biernat and A. Luszczak, Phys. Rev. **D76**, 114014 (2007), [0704.1608].

[62] A. Berera and D. E. Soper, Phys. Rev. **D50**, 4328 (1994), [hep-ph/9403276].

[63] Z. Kunszt and W. J. Stirling, hep-ph/9609245.

[64] J. C. Collins, J. Huston, J. Pumplin, H. Weerts and J. J. Whitmore, Phys. Rev. **D51**, 3182 (1995), [hep-ph/9406255].

[65] A. Donnachie and P. V. Landshoff, Phys. Lett. **B296**, 227 (1992), [hep-ph/9209205].

[66] ZEUS, S. Chekanov *et al.*, Nucl. Phys. **B800**, 1 (2008), [0802.3017].

[67] K. J. Golec-Biernat and J. Kwiecinski, Phys. Rev. **D55**, 3209 (1997), [hep-ph/9607399].

[68] K. Golec-Biernat, J. Kwiecinski and A. Szczurek, Phys. Rev. **D56**, 3955 (1997), [hep-ph/9701254].

[69] L. Trentadue and G. Veneziano, Phys. Lett. **B323**, 201 (1994).

[70] W. Furmanski and R. Petronzio, Phys. Lett. **B97**, 437 (1980).

[71] W. Furmanski and R. Petronzio, Zeit. Phys. **C11**, 293 (1982).

[72] J. C. Collins, Phys. Rev. **D58**, 094002 (1998), [hep-ph/9806259].

[73] M. Gluck, E. Reya and A. Vogt, Z. Phys. **C67**, 433 (1995).

[74] J. Bartels, J. R. Ellis, H. Kowalski and M. Wusthoff, Eur. Phys. J. **C7**, 443 (1999), [hep-ph/9803497].

[75] C. Marquet, Phys. Rev. **D76**, 094017 (2007), [0706.2682].

[76] G. Soyez, Phys. Lett. **B655**, 32 (2007), [0705.3672].

[77] H1, A. Aktas *et al.*, Eur. Phys. J. **C48**, 749 (2006), [hep-ex/0606003].

[78] ZEUS, S. Chekanov *et al.*, Eur. Phys. J. **C38**, 43 (2004), [hep-ex/0408009].

[79] A. D. Martin, W. J. Stirling and R. S. Thorne, Phys. Lett. **B636**, 259 (2006), [hep-ph/0603143].

[80] D. Salek and H1, http://www.sciwipub.com/10.3360/dis.2009.151.

[81] V. A. Khoze, A. D. Martin and M. G. Ryskin, Phys. Lett. **B650**, 41 (2007), [hep-ph/0702213].

[82] A. Hebecker, Phys. Rept. **331**, 1 (2000), [hep-ph/9905226].

[83] J. R. Forshaw, G. Kerley and G. Shaw, Phys. Rev. **D60**, 074012 (1999), [hep-ph/9903341].

[84] H. Kowalski and D. Teaney, Phys. Rev. **D68**, 114005 (2003), [hep-ph/0304189].

[85] E. Iancu, K. Itakura and S. Munier, Phys. Lett. **B590**, 199 (2004), [hep-ph/0310338].

[86] J. R. Forshaw, G. R. Kerley and G. Shaw, Nucl. Phys. **A675**, 80c (2000), [hep-ph/9910251].

[87] J. R. Forshaw, R. Sandapen and G. Shaw, Phys. Lett. **B594**, 283 (2004), [hep-ph/0404192].

[88] J. R. Forshaw, R. Sandapen and G. Shaw, JHEP **11**, 025 (2006), [hep-ph/0608161].

[89] H. Kowalski, L. Motyka and G. Watt, Phys. Rev. **D74**, 074016 (2006), [hep-ph/0606272].

[90] I. Balitsky, Nucl. Phys. **B463**, 99 (1996), [hep-ph/9509348].

[91] Y. V. Kovchegov, Phys. Rev. **D60**, 034008 (1999), [hep-ph/9901281].

[92] Y. V. Kovchegov, Phys. Rev. **D61**, 074018 (2000), [hep-ph/9905214].

[93] Y. V. Kovchegov and E. Levin, Nucl. Phys. **B577**, 221 (2000), [hep-ph/9911523].

[94] ZEUS, S. Chekanov *et al.*, Nucl. Phys. **B816**, 1 (2009), [0812.2003].

[95] K. J. Golec-Biernat and A. Luszczak, Phys. Rev. **D79**, 114010 (2009), [0812.3090].

[96] N. N. Nikolaev and B. G. Zakharov, Z. Phys. **C49**, 607 (1991).

[97] L. v. Gribov, E. m. Levin and M. g. Ryskin, Phys. Lett. **B121**, 65 (1983).

[98] J.-P. Blaizot, E. Iancu and A. Rebhan, hep-ph/0303185.

[99] A. M. Stasto, K. Golec-Biernat and J. Kwiecinski, Phys. Rev. Lett. **86**, 596 (2001), [hep-ph/0007192].

[100] H1, A. Aktas *et al.*, Eur. Phys. J. **C50**, 1 (2007), [hep-ex/0610076].

[101] V. P. Goncalves and M. V. T. Machado, Phys. Lett. **B588**, 180 (2004), [hep-ph/0401104].

[102] H1, A. Aktas *et al.*, Eur. Phys. J. **C45**, 23 (2006), [hep-ex/0507081].

[103] CDF, A. A. Affolder *et al.*, Phys. Rev. Lett. **84**, 5043 (2000).

[104] CDF, A. A. Affolder *et al.*, Phys. Rev. Lett. **88**, 151802 (2002), [hep-ex/0109025].

[105] CDF, A. A. Affolder *et al.*, Phys. Rev. Lett. **87**, 141802 (2001), [hep-ex/0107070].

[106] C. Royon, Acta Phys. Polon. **B37**, 3571 (2006), [hep-ph/0612153].

[107] P. Collins, *Regge theory and high energy physics* (Cambrige University Press, 1977).

[108] L. Schoeffel, 0908.3287.

[109] H1, A. Aktas *et al.*, Eur. Phys. J. **C51**, 549 (2007), [hep-ex/0703022].

[110] The ZEUS, S. Chekanov *et al.*, Eur. Phys. J. **C55**, 177 (2008), [0710.1498].

[111] A. B. Kaidalov, V. A. Khoze, A. D. Martin and M. G. Ryskin, 0911.3716.

[112] CDF, F. Abe *et al.*, Phys. Rev. Lett. **74**, 850 (1995), [hep-ex/9501008].

[113] D0, V. M. Abazov *et al.*, Phys. Rev. Lett. **101**, 211801 (2008), [0807.3367].

[114] CDF, T. Aaltonen *et al.*, Phys. Rev. Lett. **102**, 181801 (2009), [0901.2169].

[115] CDF, F. Abe *et al.*, Phys. Rev. Lett. **77**, 2616 (1996).

[116] D0, V. M. Abazov *et al.*, Phys. Rev. Lett. **101**, 191801 (2008), [0804.3220].

[117] CDF, E. L. Nurse, 0808.0218.

[118] K. Golec-Biernat and A. Luszczak, Phys. Rev. **D81**, 014009 (2010), [0911.2789].

[119] UA1, G. Arnison *et al.*, Phys. Lett. **B122**, 103 (1983).

[120] UA2, M. Banner *et al.*, Phys. Lett. **B122**, 476 (1983).

[121] R. K. Ellis, W. J. Stirling and B. R. Webber, *QCD and Collider Physics* (Cambridge University Press, 2003).

[122] UA1, C. Albajar *et al.*, Z. Phys. **C44**, 15 (1989).

[123] UA2, J. Alitti *et al.*, Phys. Lett. **B276**, 365 (1992).

[124] CDF, F. Abe *et al.*, Phys. Rev. Lett. **76**, 3070 (1996), [hep-ex/9509010].

[125] D0, S. Abachi *et al.*, Phys. Rev. Lett. **75**, 1456 (1995), [hep-ex/9505013].

[126] A. D. Martin, W. J. Stirling and R. G. Roberts, Phys. Lett. **B354**, 155 (1995), [hep-ph/9502336].

[127] F. Halzen and K. Mursula, Phys. Rev. Lett. **51**, 857 (1983).

[128] K.-i. Hikasa, Phys. Rev. **D29**, 1939 (1984).

[129] CDF, F. Abe *et al.*, Phys. Rev. Lett. **73**, 220 (1994).

[130] E. L. Berger, F. Halzen, C. S. Kim and S. Willenbrock, Phys. Rev. **D40**, 83 (1989).

[131] A. D. Martin, W. J. Stirling, R. S. Thorne and G. Watt, 0901.0002.

[132] CDF, F. Abe *et al.*, Phys. Rev. Lett. **78**, 2698 (1997), [hep-ex/9703010].

[133] R. J. M. Covolan and M. S. Soares, Phys. Rev. **D60**, 054005 (1999), [hep-ph/9905352].

[134] R. J. M. Covolan and M. S. Soares, Phys. Rev. **D67**, 017503 (2003), [hep-ph/0212349].

[135] R. J. M. Covolan and M. S. Soares, Phys. Rev. **D67**, 077504 (2003), [hep-ph/0305186].

[136] M. B. Gay Ducati, M. M. Machado and M. V. T. Machado, Phys. Rev. **D75**, 114013 (2007), [hep-ph/0703315].

[137] A. Luszczak, Acta Phys. Polon. **B38**, 2331 (2007).